Title

Bio-Inspired Lithium Iron Phosphate for Li-Ion Cathodes

Author

Pumwongpitak, Parawee

Publication Date

2017

UNIVERSITY OF CALIFORNIA
RIVERSIDE

Bio-Inspired Lithium Iron Phosphate Li-Ion Cathodes

A Dissertation submitted in partial satisfaction
of the requirements for the degree of

Doctor of Philosophy

in

Materials Science and Engineering

by

Parawee Pumwongpitak

December 2017

Dissertation Committee:
  Dr. David Kisailus, Chairperson
  Dr. Jianlin Liu
  Dr. Bryan Wong

The Dissertation of Parawee Pumwongpitak is approved:

Committee Chairperson

University of California, Riverside

Acknowledgements

First, I would like to express my deepest appreciation to Professor David Kisailus for his guidance and time to support me towards my degree. I am also thankful to my committee members Professor Jianlin Liu and Professor Bryan Wong for their help and advice on my research and dissertation. I would like to give thanks to Professor Krassimir N. Bozhilov, Professor Juchen Guo, and Professor Haizhou Liu for their collaborative help with characterization techniques. I would also like to thank Professor Yurong Ma for her collaborative help with my research.

My special thanks are also extended to many past and current members in Professor Kisailus group, Dr. Ian Marcus, Mathias Rommelfanger, Thomas Dugger, Ramya Mohan, Lucy Li, Jiayan Shi, and Chengyin Fu who have supported me along the way. I also thanks to all my department friends for sharing the good time during these last four years.

A special gratitude goes out all down to Royal Thai Government and Thailand Institute of Scientific and Technology Research (TISTR) for helping and providing scholarship support for my study in the United State.

Finally, I would like to thank my family and friends in Thailand for their love and support.

ABSTRACT OF THE DISSERTATION

Bio-Inspired Lithium Iron Phosphate for Li-Ion Cathodes

by

Parawee Pumwongpitak

Doctor of Philosophy, Graduate Program in Materials Science and Engineering
University of California, Riverside, December 2017
Dr. David Kisailus, Chairperson

Lithium iron phosphate (LiFePO4) is a good candidate for Li-ion cathode applications because of its high theoretical specific capacity, good cycle stability, and environmentally friendly nature. However, its performance is limited due to its low electrical conductivity and ionic diffusivity. Therefore, novel synthesis methods need to be developed to improve its electrochemical performance. One effective approach is to learn from natural systems. Several damage-tolerant structures from biological organisms (e.g., the nacreous layer of the California red abalone) consist of hierarchically structured inorganic-organic composites. These structures are formed via bio-mineralization processes, where inorganic minerals are nucleated and grown in the presence of a acidic functionalized organic matrix that controls crystal morphology, phase, size, and orientation. Utilizing inspiration from these systems, this research focuses on the investigation of organically controlled (i.e., biologically-inspired) synthesis of LiFePO4 using a modified solvothermal method. Specifically, high temperature crystal growth kinetics of $LiFePO_4$ are interrogated in order to establish a platform for understanding crystallization behavior during annealing processes. Secondly, the growth of $LiFePO_4$ crystals are examined under solvothermal conditions, modified with a ligating polymer that controls the solution environment and subsequently, the nucleation of $LiFePO_4$ crystals. Finally, structural polymers are utilized to act as scaffolds to regulate porosity in order to fabricate nanoporous cathodes with enhanced Li-ion intercalation kinetics, and thus, achieve improvements on electrochemical performance. Crystallization is interrogated using powder X-ray diffraction, SEM and TEM, while BET porosimetry is used to measure surface area. TGA and FTIR analyses are performed to confirm the presence of organic in the samples. Cyclic voltammetry is used to measure electrochemical performance.

Table of Contents

List of Figures

List of Tables

Chapter 1

Introduction

Abstract

Non-renewable energy from natural resources such as fossil fuels is being increasingly replaced by renewable or “green” energies such as wind, solar, and hydroelectric power. However, these alternative energy sources are not always available and infrequent, creating a need for energy storage devices to supply adequate energy on demand and has necessitated intensive research and development of energy storage materials [1].

1.1 Batteries

Batteries are a promising class of energy storage devices, which store electricity in the form of chemical energy through electrochemical reactions. Lithium Ion Batteries (LIBs) have higher energy densities and longer cycle lifetimes when compared to other secondary batteries such as Lead-Acid, Nickel-Cadmium (Ni-Cd), Nickel-Metal Hydride (Ni-MH), and Lithium polymer batteries (as shown in Table 1.1). Currently, LIBs have a wide range of usage, from portable electronic devices—used in 57.4% of cell phones and 31.5% of laptop computers—to large scale applications including electric vehicles (EVs), hybrid electric vehicles (HEVs), and station batteries for renewable energy [2-4].

Table 1.1 Typical properties of secondary batteries [5]

Type of battery	Cell voltage (V)	Specific energy (Wh/kg)	Cycle life (up to 80% initial capacity)	Charge time (h)	Self-discharge per month (%)
Lead-Acid	2	30-50	200-350	8-16	5
Ni-Cd	1.25	45-80	1500	1	20
Ni-MH	1.25	60-120	300-500	2-4	30
Li Ion	3.6	110-180	500-1000	2-4	10
Li polymer	3.6	100-130	300-500	2-4	10

1.1.1 Lithium ion batteries

The first non–aqueous rechargeable lithium ion batteries were introduced in the 1990s. A typical Li-ion battery is composed of an anode (negative electrode) such as graphite, a cathode (positive electrode) made of lithium metal oxide, an electrolyte such as a solution of lithium salt in a mixed organic solvent ($LiPF_6$), and a microporous separator. Figure 1.1 shows a schematic of a typical lithium-ion battery. During charging (lithium ion insertion), lithium ions migrate from the cathode to anode through the electrolyte, and then intercalate into the anode host, transferring electrons to the cathode so the overall charge is balanced. This makes the chemical potential of lithium in the anode higher than that of the cathode, storing energy until it is discharged (lithium ion extraction), allowing lithium ions to flow from the anode to the cathode [1, 6-7].

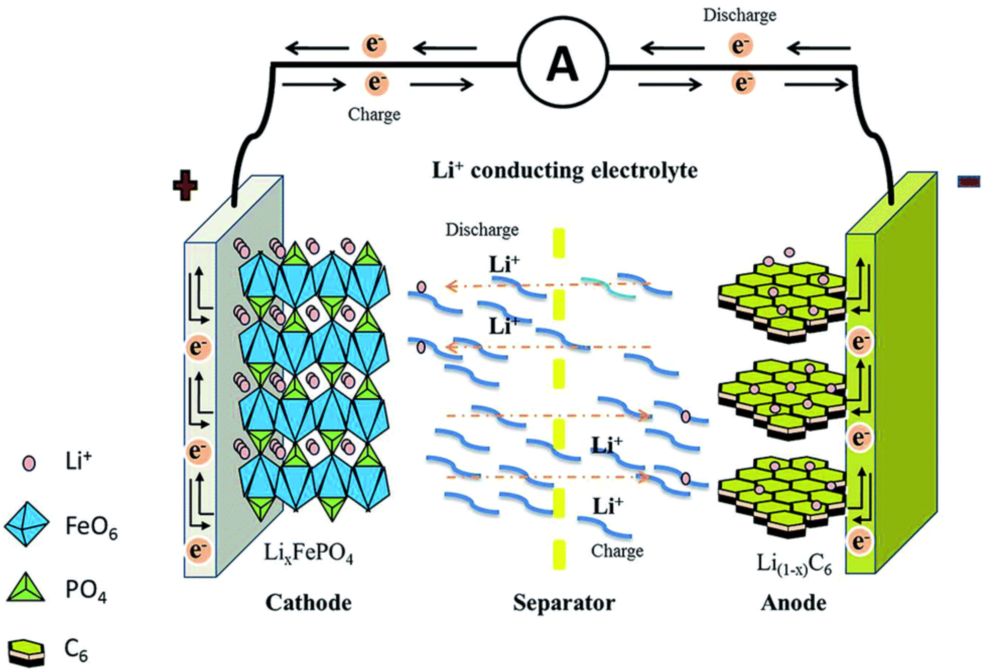

Figure 1.1 Schematic of a Lithium-ion battery [8].

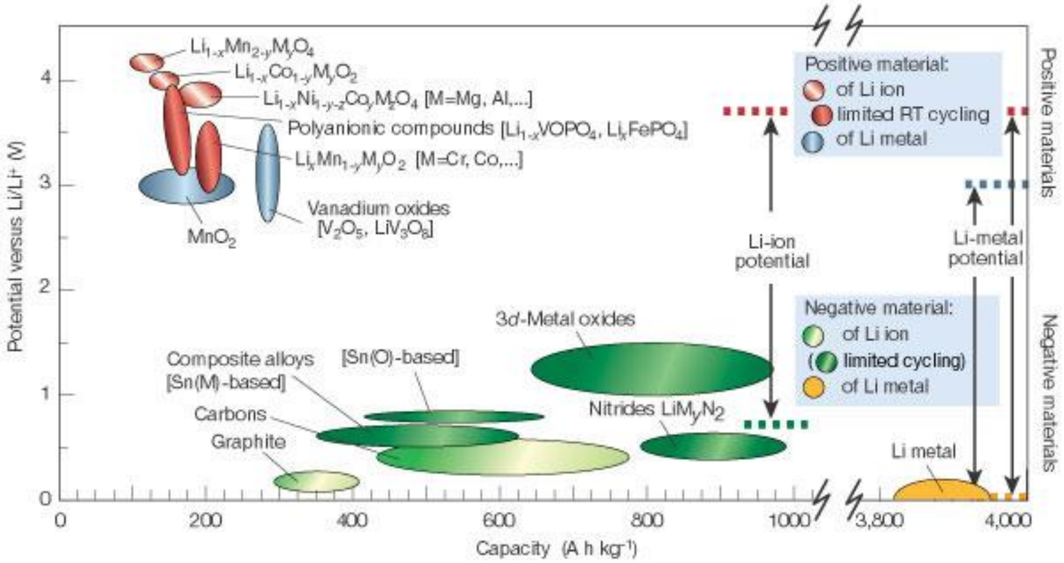

Figure 1.2 Voltage versus capacity for positive and negative electrodes [9].

To improve battery performance, extrinsic properties such as cell potential and capacity, and intrinsic properties of the cathode and anode materials (e.g., voltage, structural stability, and positive ion diffusivity) are considered. Figure 1.2. illustrates the voltage and capacity of several cathode and anode materials. Battery cycle life and lifetime are related to the interfaces between the electrolyte and electrodes, and battery safety depends on the stability of electrode materials and interfaces [9-10]. Therefore, each component must be considered when improving batteries to meet the increasing energy and power demand. In LIBs, the cell voltage and capacities are primarily determined by the cathode-limited lithium transportation rate. Thus, the development of cathode materials has been intensely explored in recent decades.

1.1.2 Cathode materials for lithium ion batteries

There are three classes for commercial positive electrode materials categorized by their structure: layered oxides (LMO_2; M = Mn, Co, and Ni), spinel oxides (LiM_2O_4), and olivine phosphates ($LiMPO_4$; here M is a 3d transition metal element such as Co, Mn, Fe) as shown in Table 1.2.

Table 1.2 The properties of positive cathode materials [11].

	$LiCoO_2$	**NCM**	**NCA**	**$LiMn_2O_4$**	**$LiFePO_4$**
Structure	Layered	Layered	Layered	Spinel	Olivine
Voltage (V)	3.7	3.6	3.6	3.8	3.4
Capacity (mAh g−1)	140– 200	160–190	180– 200	100–120	150–165
Life (cycles)	500– 1000	500– 3,000	500– 2,000	500– 3,000	1000– 20,000
Price	High	Medium	High	Low	Low
Safety	Medium	Good	Good	Good	Excellent
Application area	3C	3C, HEV, EV	3C, EV	HEV, EV, stationary	HEV, EV, stationary…

NMC = $LiNi_xCo_yMn_zO_2$ x + y + z = 1; NCA = $LiNi_{0.8}Co_{0.15}Al_{0.05}O$
HEV = Hybrid electrical vehicle
EV = Electrical vehicle

1.1.2.1 Layered $LiMO_2$

$LiCoO_2$, $LiMnO_2$, and $LiNiO_2$,

$LiCoO_2$ positive electrodes were investigated in the 1980s by John Goodenough [12]. The first commercial cathode material for LIBs was a 4-volt $LiCoO_2$ cell that was introduced by Sony Corporation in 1990 [13]. $LiCoO_2$ provides 2D-lithium ion diffusion channels through the interlayered CoO_6 as shown in Figure 1.3. Edge-shared CoO_6 octahedra are suitable for high discharge rate cathodes with theoretical capacities as high as 273 mAh/g [14]. This system is composed of a Li_xC_6 anode and a $Li_{1-x}CoO_2$ cathode, which demonstrates a reduced practical capacity amounting to just half of its achievable theoretical capacity (~140 mAh/g), due to the dissolution of cobalt in the electrolyte during delithiation processes over the composition range $1 \leq x \leq 0.5$ when below 4.2 V [15-17], and the resulting instability of the delithiated oxide layer [14]. Furthermore, cobalt processing is expensive, and toxic [18]. These limitations have spurred efforts to find alternative cathode materials with higher capacity, energy, and cycle life, requiring safer processing techniques.

$LiNiO_2$ is another cathode material with a hexagonal crystal system. It is more abundant and cheaper than Co, but is less stable and ordered when compared to $LiCoO_2$. During the exothermic oxidation of electrolyte, the layered structure collapses due to the smaller size difference between Ni^{2+} (0.83Å) and Li^{+} (0.9Å) [19]. $LiMnO_2$ has two-unit cell structures: orthorhombic and rhombohedral. The rhombohedral form can transition into a monoclinic structure due to the Jahn-Teller distortion of Mn^{3+}. This leads to a thermodynamically unstable crystal structure. Moreover, both orthorhombic and rhombohedral forms of $LiMnO_2$ can be transformed into a layered hexagonal structure during cycling, resulting in decreased electrochemical performance [20].

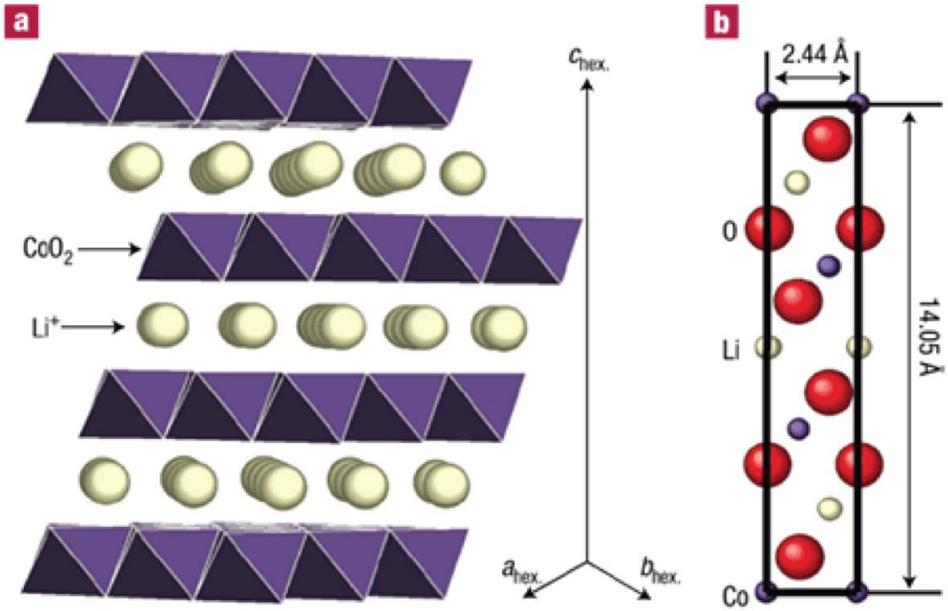

Figure 1.3 (a) Crystalline structure of 2-D layered $LiCoO_2$ (b) Along [110] Zone axis shows lithium, cobalt, and oxygen atoms [21].

1.1.2.2 <u>Spinel $LiMn_2O_4$</u>

$LiMnO_4$ crystals have a strong edge sharing MnO_6 octahedral framework, as shown in Figure 1.4., that exhibits a stable structure during the charge-discharge process, during which lithium occupies the tetrahedral sites [18, 22]. Although $LiMnO_4$ is safer than $LiCoO_2$, it has a lower capacity and undergoes phase changes during cycling [23]. Only 80% of lithium ions can be de-intercalated from the structure, while the other 20% remain in the lattice. This leads to a lowered efficiency of lithium utilization and potential safety concerns [24].

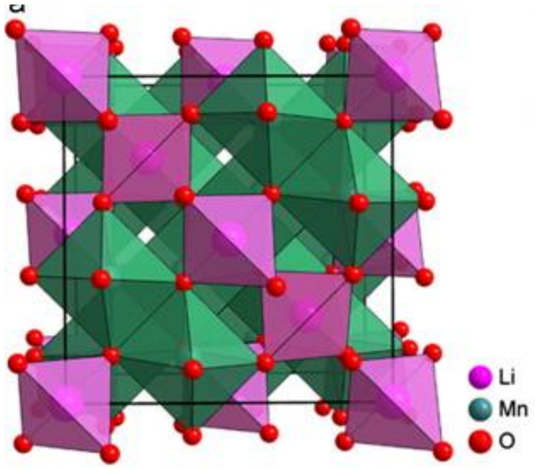

Figure 1.4 Representative crystal structure of spinel $LiMn_2O_4$ [25].

1.1.2.3 Olivine compounds $LiFePO_4$

Iron-based olivine phosphate compounds are attractive when compared to other cathode materials due to the abundance of iron in the earth, lower cost, reduced toxicity of extraction and purification processes (relative to Co, Ni, or Mn), high thermal stability, and a high theoretical specific capacity of 170 mAh/g. The strong covelent P-O bond in poly-anion materials is theorized to provide a structurally robust framework during lithium de-intercalation, eliminating any safety concerns[10].

Structure of $LiFePO_4$

$LiFePO_4$ (LFP) is a polyanionic compound with an orthorhombic olivine structure and belongs to space group Pnma [10, 26-27]. Its crystal structure consists of a slightly distorted hexagonal-close-packed array of oxygen atoms, as shown in Figure 1.5. The phosphorus atoms occupy one-eighth of the tetrahedral sites. Iron and lithium atoms occupy half of the octahedral sites. Each FeO_6 octahedron shares four common corners in the bc-plane, two edges with LiO_6 octahedra, and one edge with PO_4 tetrahedra. LiO_6 octahedra are edge-shared along the b-axis and share two edges with PO_4 tetrahedra [1, 28].

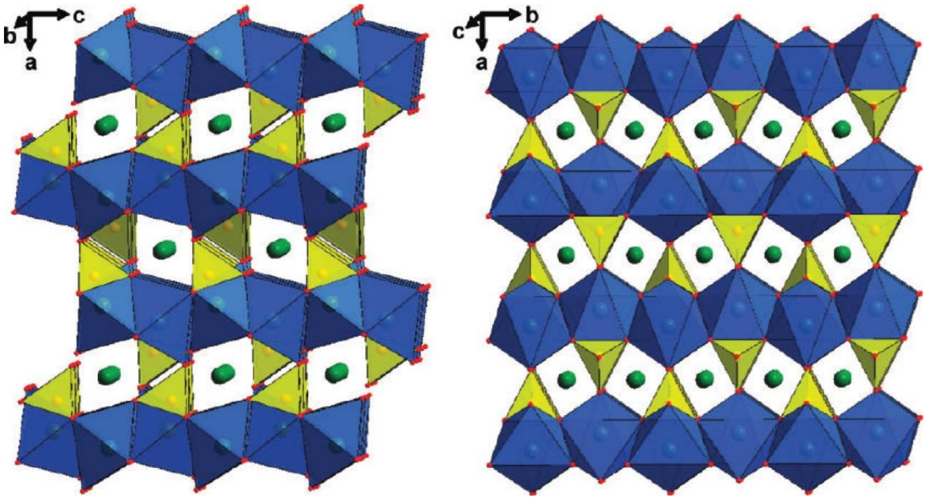

(a) (b)

Figure 1.5 Crystal structure of Olivine $LiFePO_4$ (a) along the b-axis and (b) along the c-axis [29]. Reprinted with permission from (Brian L. Ellis, Kyu Tae Lee, Linda F. Nazar, Positive Electrode Materials for Li-Ion and Li-Batteries, Chemistry of Materials, American Chemical Society, Feb 1, 2010). Copyright (2010) American Chemical Society.

Lithium ions are extracted from the structure during delithiation to yield $FePO_4$ without changing the crystal structure, just slightly altering the lattice parameters. Table 1.3. shows the unit cell parameters and the atomic co-ordinates of $LiFePO_4$ and $FePO_4$ obtained from the Rietveld refinement of X-ray powder diffraction data [28].

Table 1.3 Unit cell parameters obtained from two-phase Rietveld refinements of the powder X-ray diffraction data [30-31].

	$LiFePO_4$	**$FePO_4$**
a (Å)	10.3290	9.81
b (Å)	6.0065	5.79
c (Å)	4.6908	4.78
$V (A^3)$	291.2	271.5

Oxygen atoms in this crystal structure are strongly bound with iron and phosphorus atoms, resulting in a significantly stable structure at temperatures up to 400 °C, unlike $LiCoO_2$, which is only stable to 250°C [10]. In addition, the high lattice stability during lithiation/delithiation processes gives rise to improved cyclic performance and fewer safety issues [31].

Chen *et al.* [32] showed that the (010) surface, or *ac* plane, is a large facet of anisotropic plate-like $LiFePO_4$ crystals aligned along the *c*-axis. Islam *et al.* [33], through investigations of lithium ions transported in the olivine structure, confirmed that [010] is the lowest energy pathway for lithium ion diffusion, 0.55 eV, as shown in Figure 1.6 [33]. Thus, thin plate particles with large (010) surfaces would increase the active area and decrease the diffusion distance of lithium ions. Growth of the (010) facet is thermodynamically favored over other crystal facets [34].

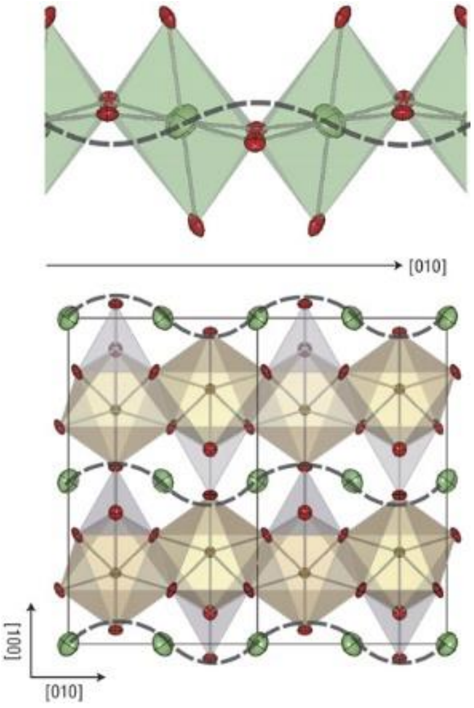

Figure 1.6 Non-linear one-dimensional lithium ion migration in the [010] direction of $LiFePO_4$ [35].

Electrical performance of $LiFePO_4$

$LiFePO_4$ (Triphylite) dissociates into $FePO_4$ (Heterosite) and Li ions at 3.45 V according to the following reaction:

$$LiFePO_4 \rightarrow FePO_4 + Li^+ + e^- \quad (1.1)$$

Rate Capability

Transport of electrons from within the particle to its surface and on to the current collector needs to be as fast as possible. Therefore, the electrical conductivity between

$LiFePO_4$ particles and current collector plays a critical role in battery performance. This can be achieved by applying a conductive carbon coating to the $LiFePO_4$ particles, rather than reducing particle size or cation doping, especially at high current rates [36].

Capacity density

The most important battery performance parameters for electric vehicles are specific energy (Wh/kg) and energy density (Wh/L). Increasing the specific energy significantly decreases the mass and cost of batteries. Specific energy is determined by cell design, electrode structure and potential, as well as capacity. Thus, capacity density (mAh/L) is one of the most important factors because the active cathode material accounts for 40 wt% of the high-energy cell. Even though the theoretical specific energy of $LiFePO_4$ is as high as 170 mAh/g, the energy density of batteries is related more to the capacity density than the specific capacity.

Energy density in batteries decreases with the tap density of $LiFePO_4$ powders because of the nanoparticle size and carbon coating. The nanopartciles provide better kinetic of lithium diffusion than large paticles [37]. Modifying LFP particles with carbon on their surface increases electronic conductivity due to the sp^3 character of carbon or sp^2 character on carbon atoms of polymer chains [38]. For example, nanoparticles of $LiFePO_4$ have a tap density from 1.0-1.3 g/cm^3, significantly lower than commercial $LiCoO_2$ materials (tap density 2.2-2.4 g/cm^3)[39]. Currently, the highest tap density of $LiFePO_4$ powders coated with 7 wt% carbon is 1.8 g/cm^3 [40]. Above that, too thick a carbon coating results to less tap density [41].

Cycle Lifetimes

Batteries for HEV and PHEV applications should last approximately 300,000 cycles over 15 years of active use [42]. The capacity degradation during both cycling and storage conditions is a major issue caused by solid electrolyte interphase (SEI) formation on graphite anodes. This results in the loss of lithium inventory because iron ions are precipitated on the surface of graphite anode and the separator. This influences the degradation of capacity that depends on the iron content. The iron ions can also dissolve in acidic electrolytes, which can be averted by replacing the slightly acidic $LiPF_6$ with less acidic lithium bis(oxalate)borate (LiBOB) or $LiAlO_4$ solutions [43]. The dissolution rate of iron ions also depends on the testing temperature, cut off voltage, the synthesis method, impurity content and $LiFePO_4$ particle size. For example, at high temperatures, formation of the impurity phase iron pyrophosphate ($Fe_4(P_2O_7)_3$) leads to a higher rate of iron dissolution and a faster capacity fade [31].

Temperature dependence

Lithium ion batteries have low performance at low temperatures especially below -20°C due to the loss of capacity, limited electrode kinetics, low electrolyte conductivity, low lithium diffusivity, and high charge transfer resistance at the electrode/electrolyte interface. The low temperature conductivity can be improved by optimizing the lithium salts or the electrolyte solutions such as using Lithium hexafluoro phosphate/ethylene carbonate, dimethyl, diethyl, and ethyl-methyl carbonates ($LiPF_6$/EC-DMC-DEC-EMC) instead of $LiPF_6$/EC-DMC. At high temperatures, the specific capacity of $LiFePO_4$ improves as the diffusion rate of the iron ions and electron transfer activity increases. But at higher temperatures, there is an increase in iron ion dissolution, leading to a capacity fade as a solid electrolyte interface (SEI) layer is formed on the graphite anode surface. The stability at high temperatures can be improved by using a LiBOB electrolyte or $Li_4Ti_5O_{12}$ anode material [31].

1.1.4. Approaches to improve the electrical performance of $LiFePO_4$

Particle size reduction

Particle size reduction can improve the rate capacity and cycling stability of $LiFePO_4$ by reducing the transport distance for electrons and lithium ions. The ionic diffusion constant in nanoparticles is a lot faster than in micro-particles [44]. Zhang [36] determined that the best particle size for high rate performance is about 30-50 nm. However, smaller particle sizes lead to a low tap density and energy density. The particles need more supporting materials such as conductive carbon or binder in the cells. This makes the cost of manufacturing significantly higher than that of the microparticles. Moreover, due to their high surface area and less coordinated surface atoms, nanoparticles are more likely to undergo surface reactions and dissolve into the electrolyte solution, which may reduce the cyclic lifetime of batteries. Nanoparticles are also more difficult to handle during processing and pose more inhalation risks and potential environmental hazards. Therefore, it is believed that the optimal particle size for high power applications is between 200-400 nm and even larger in PHEVs, where the energy density, battery mass, and energy cost are more important than the high rate capacity [31].

Conductive surface coating

Conductive polymers are widely used to coat the surface of $LiFePO_4$ particles to improve their specific capacity, rate performance and cycling life by enhancing their electric conductivity. Carbon coatings also inhibits the growth of $LiFePO_4$ particles during annealing and acts as a reducing agent to prevent oxidation of Fe^{2+} to Fe^{3+} [45]. Zhang et al. [36] reported that carbon coated $LiFePO_4$ with an average particle size of 300 nm showed good rate capability.

Liang et al. [46] synthesized $LiFePO_4$/C composites through a hydrothermal reaction in a glucose solution and determined that the *in-situ* carbon coating provides better electrochemical performance due to an even distribution of carbon on the $LiFePO_4$ surface. Furthermore, carbon coated $LiFePO_4$ particles prepared at higher temperatures such as 700°C have much higher electronic conductivity than the samples prepared at 600°C due to increased graphitization of these coatings.

Graphitic carbons with threefold coordination symmetry (sp^2 coordinated) are more conductive than disordered carbon with fourfold coordination symmetry (sp^3 coordinated) [47.] Carbon additives with aromatic groups such as polystyrene and sugars were used during synthesis as they increased the yield of graphitic carbon [47-48].

However, more carbon coating results in higher processing costs and reduced tap density, which means low battery energy density. This thick carbon also limits the penetration of lithium ions, especially the thickness is greater than 3-5 nm [49]. Dominko et al., demonstrated that 1-2 nm to 10 nm of carbon thickness from citrate anion as a carbon source was optimized to improve the electrochemical performance [50]. Zhu et al., reported less than 0.2 wt% of carbon content increased the electronic conductivity and then enhanced the electrochemical performance[51]. Other conductive coatings such as Cu, Ag, or Fe_2P are also effective to improve the electrochemical performance of $LiFePO_4$ particles [52-53].

Dopant substitution

Adding doping materials can increase the rate capacity and cyclic stability of $LiFePO_4$. Chung et al. [54] reported that the electric conductivity of $LiFePO_4$ increases eightfold by controlling cation non-stoichiometry combined with solid solution doping of supervalent cations such as Al, Ga, Mg, Nb, Zr, Ti. For example, vanadium-modified $LiFePO_4$ was introduced by Hong et al. [55] where vanadium was substituted in Fe sites. This results in an enhanced cycling rate performance by increasing the effective cross sectional area of the LiO_6 octahedral face, thus reducing the bottleneck for lithium transportation. A modeling study from Islam et al. [33] suggested that doping-$LiFePO_4$ on either Li (M1) or Fe (M2) sites is unfavorable and does not result in significantly increased electrochemical performance. Anion doping with F and Cl atoms was investigated to possibly enhance electrochemical performance, due to the high ionicity of F that could lead to increased lithium ion diffusivity. However, the doped particles without carbon coatings did not significantly increase the electrochemical performance of $LiFePO_4$, when compared to small particle sizes and carbon coating techniques. So far, carbon coatings have proven to be the most effective method to improve the electrochemical performance of $LiFePO_4$.

1.1.5 Challenges with using $LiFePO_4$

$LiFePO_4$ has poor intrinsic ionic and electronic conductivity due to the lack of electronically conducting species. Thus, the conductivity is as low as 10^{-11}s/cm. This is not enough to satisfy the electrochemical performance requirements, especially the high rate expectations with EVs. Therefore, increasing the lithium ion diffusion rate by shortening the diffusion distance with size reduction can improve ionic conductivity. In addition, optimizing the continuous conductive carbon coating of $LiFePO_4$ without reducing the effective packing density will directly increase electronic conductivity of this material [56].

1.2. Biological control of mineral crystallinity

Biomineralization is the process that organisms use to convert ions in solutions into solid inorganic materials and have been extensively studied [57]. Calcium (Ca) is the most common cation in biominerals, with Iron (Fe) as the second most common. Phosphates, oxides, and carbonates are the most common anions. The study of biominerals shows roughly 80% are crystalline and 20% are amorphous [57-58]. Crystal deposition initiates from the supersaturation of a fluid, followed by mineral nucleation and crystal growth [57]. The final products may form by interactions between ions and functional and structural organic molecules, which serve as nucleation templates and structural supports, respectively [59]. The resulting structures are hierarchically arranged organic/inorganic composites with desired mechanical function provided by a combination of stiff mineral and tough organic. Biomineralized composites, including shells and bones, are examples of these biological composites, and provide interesting insights to controlled crystal growth. Further descriptions of the formation mechanisms of these structures are provided below.

1.2.1 Nacre

Molluscan nacre from the red abalone shell is an organic/aragonite ($CaCO_3$) composite with high strength and toughness 20-30 times that of monoclinic aragonite. The microstructure of nacre is described as “brick and mortar” arrangement, as shown in Figure 1.7. The “bricks” are flat polygonal crystals of aragonite platelets forming 450-500 nm thick layers. The “mortar” refers to 1-5 wt% of an organic adhesive layer (thickness ~ 21-31 nm) that is composed of polysaccharide (β-chitin) and protein fibers. The aragonite bricks are composed of nano-grains glued together by biopolymer macromolecules [60-62]. Stacks of aragonite platelets maintain their orientation continuity through mineral bridge connections, which are formed and mediated through porous organic membranes as shown in Figure 1.8. The nearly perfect c-axis alignment normal to the plane of the platelets can be observed. Lamellar micro-architectures of the soft organic layers between the hard composite tablets provide toughness and impact resistance through crack deflection and resist slip.

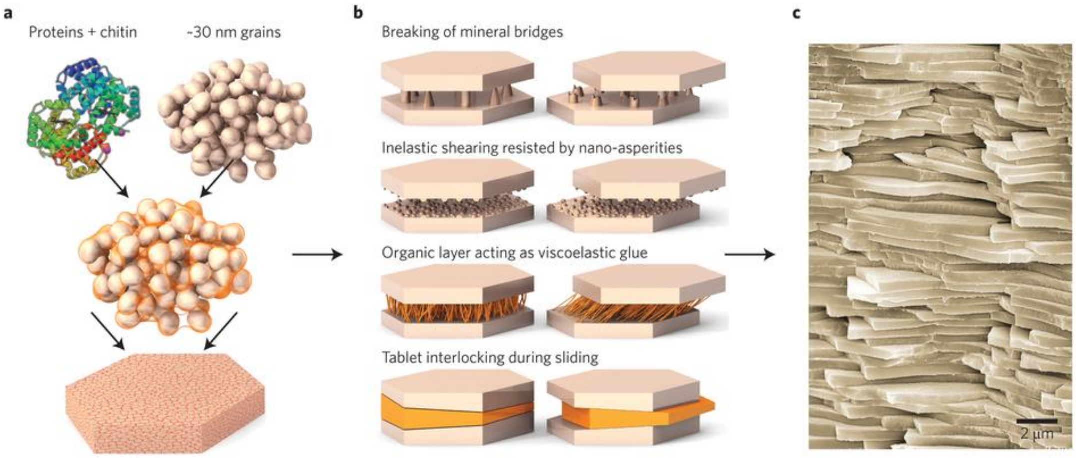

Figure 1.7 The hierarchical structure of Nacre [63].

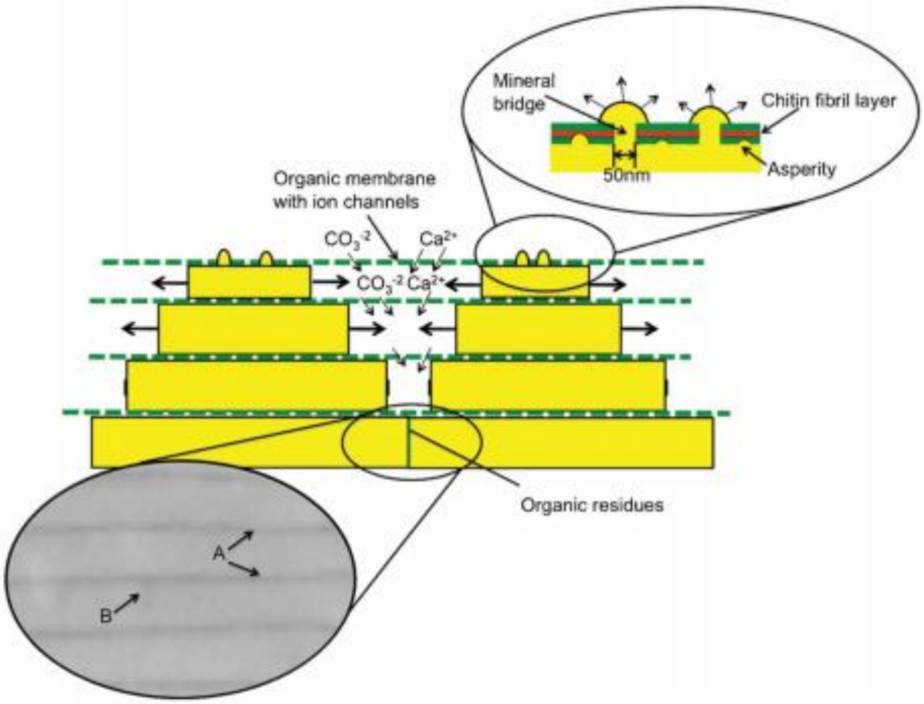

Figure 1.8 Mechanism of growth of Nacre in abalone shell [64].

1.2.2 Bone

Bone is another example of a damage-tolerant natural material that combines strength and toughness. Two inorganic nanophases comprise 95% of the dry weight of bone. The remaining 5% are organic molecules (non-collagenous proteins) and amorphous or poorly crystalline inorganic salts. The two nanophases are an organic matrix of collagen fibrils (300 nm long and 1.5 nm diameter), and plate-shaped hydroxyapatite ($(Ca_{10}(PO_4)_6(OH)_2)$) nanoparticles approximately 50 nm × 25 nm in size and 1.5 nm thick, surrounded by glycoproteins, mucopolysaccarides, and network cells. The c axis of the hydroxyapatite tablets is parallel to the collagen fibrils [63, 65-66]. A hierarchical structure of bone is shown in Figure 1.9. The minerals are formed in the extracellular collagenous matrix in vesicles, which contain nanoparticles of highly disordered calcium phosphate mineral. The apatite has hexagonal crystal structure but the crystals in bone are flat plates and do not represent hexagonal symmetry. This could be explained by crystal formation from an octacalcium phosphate (OCP) precursor phase [59].

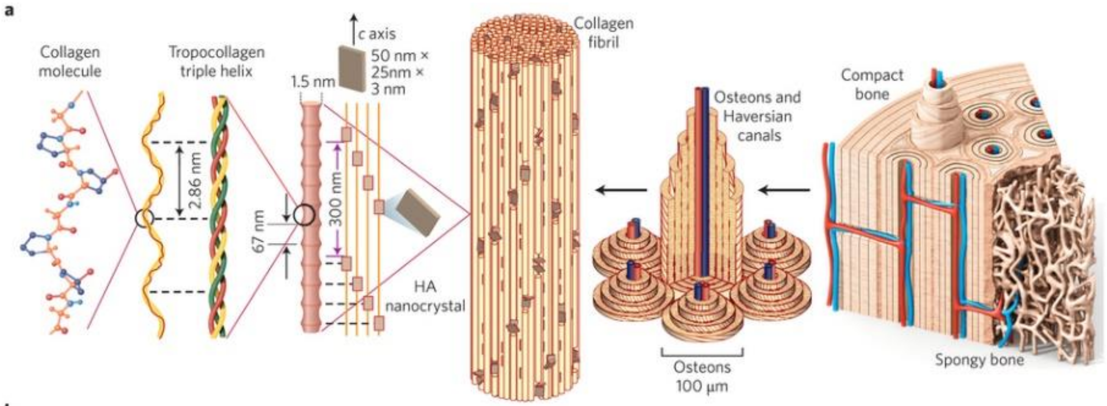

Figure 1.9 The hierarchical structure of Bone [63]. Toughening mechanisms in bone originate from the smallest length scales of uncoiling mineralized collagen to a coarser length scale. The hydroxyapatite/collagen interface and intermolecular crosslinking promote plasticity at this nanoscale through fibrillary sliding. At larger length scales (10-100) microns, the fracture resistance of bone comes from crack deflection by pores and apatite crystals [63].

Other biological materials such as horns and teeth consist of calcium phosphate crystals with non-stoichimetric carbonate-hydroxyl-apatite in their structures and an organic conponent, similar to bones [66].

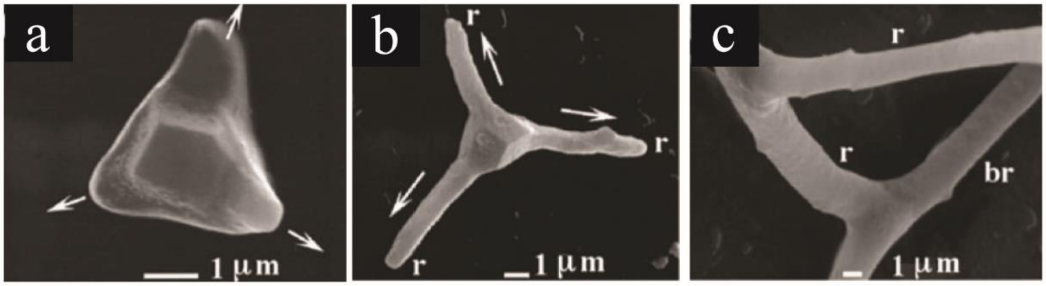

Figure 1.10 Sea urchin (*Paracentrolus lividus*) at different developmental stages. (a) Earliest stage of spiculogenesis with tree radii starting to grow. (b) Triradiate spicule at 25 h. (c) Fully developed state showing faceted calcite (r, radii: br, body rod) [67].

1.2.3 Sea urchin spines

Sea urchin spines consist of nano-particulate magnesium and calcite building blocks that are highly oriented in one direction (Figure 1.10) [58, 68]. Figure 1.10 shows larval spicules of the sea urchin (*Paracentrolus lividus*) at different stages of development. At the earliest stage, an amorphous calcium carbonate (ACC) is formed first in the sea urchin larvae which then transforms into calcite crystals later in a mature sea urchin [69]. Photoemission Electron Microscopy (PEEM-3) confirms that the sea urchin spicules are composed of three phases: hydrated amorphous calcium carbonate ($ACC \cdot H_2O$), anhydrous calcium carbonate (ACC), and calcite ($CaCO_3$). Therefore, the sea urchin spicules are formed via two amorphous mineral precursors ($ACC \cdot H_2O$ and ACC), which crystallize to form calcite. The $ACC \cdot H_2O$ is formed first at 36 h, then to ACC at 48 h, and finally transform to calcite at 72 h [70].

Once the sea urchin has matured, its spine is composed of nanoparticles with the ACC layers are coated on the calcite nanoparticles [71]. This mechanism can be observed in the mollusk larvae as the ACC transforms to Aragonite [58].

1.3. Bio-inspired cathode materials for lithium ion batteries

Based on the aforementioned examples of biomineralized structures, it is clear that Nature provides many examples of exquisite control over the nucleation and growth of inorganic materials using a combination of physical and chemical organic structures, control of pH, and precursor concentrations. Thus, the objective of this project is to utilize a similar strategy that integrates these parameters to synthesize lithium iron phosphate particles with controlled crystallization, particle size and distribution, shape, and crystallographic orientation, while maintaining a thin carbon coating to promote effective performance. To achieve this objective, various tasks were accomplished:

1.) Understand the crystal growth kinetics of crystalline $LiFePO_4$ upon annealing due to the post annealing requirements for carbon coating.

2.) Investigate the effects of a chemically functionalized organic (polyacrylic acid) on the size and shape of synthesized $LiFePO_4/C$ composites as a function of time and concentration under solvothermal conditions.

3.) Synthesize porous and conductive $LiFePO_4/C$ structures using an organic scaffolding polymer (polyvinyl alcohol) with controlled porosity and high tap density.

4.) Determine the structure-electrochemical performance relationships in the materials produced in tasks 2

To improve the electrochemical performance of $LiFePO_4$, understanding the relationships between synthesis, structure, and electrochemical performance is critical. Task 1 will provide grain growth information to control particle size during the annealing process, which is related to the kinetics of Li-ion transport. Task 2 provides information to influence the energy density and rate capacity of batteries by controlling the size and shape of $LiFePO_4$ particles. Task 3 will enhance the electronic conductivity and ion-transport kinetics by producing porous structures that will increase contact between liquid electrolyte and active $LiFePO_4$ particles. This will lead to improved specific capacity, rate performance and cycling life.

1.4. Objective

The goal of this project is to understand nucleation and growth mechanisms of bio-inspired modified $LiFePO_4$ cathode materials. This will offer the possibility for an increase in the electrochemical performance for lithium ion battery cathodes in comparison to currently available commercial $LiFePO_4$ cathode materials. The objectives are as follows:

1.) Understand the kinetics of $LiFePO_4$ crystallization upon annealing at temperatures required for carbon coating.
2.) Investigate the effects of a metal-chelating polyacrylic acid on the nucleation and growth of $LiFePO_4$ under solvothermal condition.
3.) Utilize an organic scaffold polymer (polyvinyl alcohol) to produce porous conductive $LiFePO_4$ structures.
4.) Determine the structure-performance relationships in the materials produced in objective 2

Chapter 2

Investigation of the crystal growth kinetics of $LiFePO_4$ during annealing

Investigation of the crystal growth kinetics of $LiFePO_4$ during annealing

Abstract

$LiFePO_4$ (LFP) particles were synthesized using standard industrial methods and annealed from 300 to 700 °C in a $5\%H_2/95\%N_2$ atmosphere to study the mechanisms of phase transformation and grain growth. Specifically, a solvothermal synthesis method was used, followed by ball milling for 6 h to obtain isotropic particles. We observed almost no grain growth at 300 °C. At higher temperatures, 400 and 500 °C, the results from the grain growth kinetic study indicate that the grain growth exponent is 2 (diffusion of ions along the particle boundary) and 3, (volume diffusion) respectively. Significant grain growth was found when the LFP particles were annealed at 600 and 700 °C.

2.1 Introduction

Several industrial methods are used to produce $LiFePO_4$ (LFP) materials as cathodes for batteries, of which solid state and solution routes are the most common. In solid state syntheses, LFP precursor powders (e.g., Li_2CO_3, $FeC_2O_4.2H_2O$ and $NH_4H_2PO_4$) are ground, pre-calcined at 250-300 °C, and finally calcined at 400-800°C to form LFP powder. This method takes a long time and often leads to large particles, broad particle distributions, and nonuniform shapes, resulting in a poor electrochemical performance [72]. Mechano-chemical activation, a modified solid state process, uses high energy ball milling to accelerate calcination, typically within temperature ranges from 600-900 °C and atmospheres such as nitrogen and 5% H_2/95% N_2 or vacuum for 0.5-10 h [73-75]. However, the ball milling medium can introduce impurities as $Li_9Fe_3(P_2O_7)_3(PO_4)_2$, and the LFP particles can get hotter than the desired temperature due to energy imparted from collisions, leading to large particles and broad size distributions from 0.02 to 2000 microns.

In the melt-synthesis method, precursor powders such as $FePO_4$ and $LiPO_3$ are heated at a temperature from 1000 °C to 1100 °C to form a liquid phase. This method leads to the presence of impurities such as Fe_2O_3, Fe_3O_4, $LiFeP_2O_7$, $Fe_2P_2O_7$ and $Li_3Fe_2(PO_4)_3$[76-78]. The carbo-thermal reaction is another process that uses Fe(III) compounds as Fe precursors and carbon source as a reducing agent. The precursors were mixed, ball milled for 2-4 h, and finally calcined at 550-850 °C for 8-10 h in an inert atmosphere[79]. Although temperature control is more precise for these methods, ball milling can still impart impurities and lead to large particle sizes, which results in a poor electrochemical performance[80].

Solution based methods such as sol-gel or hydrothermal syntheses are also widely used to produce LFP particles because these processes consume less energy than solid state processes and can produce small, uniform particles. Hydrothermal synthesis starts with mixing LFP precursors with the required stoichiometry and then treats a homogeneous mixture of precursors in an autoclave at temperatures above 100 °C [81-83]. Sol-gel synthesis is a wet chemical process where the precursors and solvent form a colloidal suspension in a gel at low temperatures such as 80 °C[84-85]. However, these methods also require heat treatment at 400-750 °C in an inert atmostphere[84, 86]. Moreover, in spray pyrolysis, mixed precursors are pumped into a pyrolysis furnace and then calcined at 700-800 °C in a nitrogen atmosphere. Co-precipitation is another solution method where the mixed precursors precipitate to form stoichiometric particles, which are then filtered and annealed at 500-800 °C for 12 h under N_2 or argon atmosphere to induce crystallization.

Although each of these processes are used to mass produce LFP, the high calcination temperatures result in nonuniform, large particles with sub-optimal electrochemical performances. More control over grain sizes is needed, and to do so, the mechanisms of grain growth during annealing must be understood. By understanding grain growth parameters at different temperatures, we can control grain size and distributions of LFP to optimize the electrochemical performance of batteries.

2.2 Experimental procedure

Preparation of materials

$LiFePO_4$ particles were synthesized by a solvothermal method using stoichiometric $LiOH \cdot H_2O$, $FeSO_4 \cdot 7H_2O$, and 85 wt % H_3PO_4 as starting materials in a 50 vol% triethylene glycol/ 50 vol% water system. Initially, stoichiometric mixtures of precursors were stirred for 10 min in a beaker. The pH of the mixed precursor suspension was adjusted to pH 6 using sodium hydroxide or sulfuric acid. Then, the precursor particle suspensions were transferred into Teflon liners. Argon was purged over the headspace of the liners to prevent oxidation. The liners were placed in steel autoclaves and heated in a conventional oven at 200 °C for 150 min. The precipitated powders were collected using a centrifuge and subsequently washed with deionized water and 70% ethanol. Then the obtained powder was dried overnight at 70 °C in a vacuum oven. After drying, the as-synthesized particles were ground using a ball mill for 6 h, and subsequently isothermally annealed at 400, 500, 600, and 700 °C, each for 20 min, 1 h, 3 h, and 12 h in a 5% H_2/95% N_2 atmosphere.

Material Characterization

The crystallite size and phase of the powder products were determined by X-Ray powder diffraction (XRD, Panalytical Empyrion) using Cu Kα radiation. The Scherrer method was used to calculate crystallite sizes based on the measurement of the full-width at half maximum (FWHM) of diffraction peaks. Scherrer's equation is as follows:

$$D = \frac{K\lambda}{\beta cos\theta} \tag{2.1}$$

Where D is the mean size of a small crystal

K is a dimensionless shape factor, usually a value of 0.9

λ is X-ray wavelength (1.54 Å)

β is the diffraction peak FWHM in radians

θ is the Bragg angle

Morphologies and particle sizes were observed using a Scanning Electron Microscope (SEM, Nova Nano 450, FEI) at 10 kV and Transmission Electron Microscope (Tecnai12, FEI) at 120 kV accelerating voltage. Adobe Photoshop® was used to measure particle sizes.

2.3 Results and Discussion

Characterization of synthesized LFP after solvothermal processing

Diffraction patterns of powders after the solvothermal reaction (Figure 2.1(a)) indicate that all peaks can be identified as a single phase of LFP with orthorhombic lattice structure and space group Pnma (JCPDS No. 81-1173). The peak intensity of the (020) reflection is significantly greater than that of the (200) reflection, suggesting that plate-like LFP particles were obtained[65]. Indeed, this was confirmed with SEM, which highlighted the formation of anisotropic particles. The crystallite size was calculated to be 53±8 nm using the Scherrer's equation.

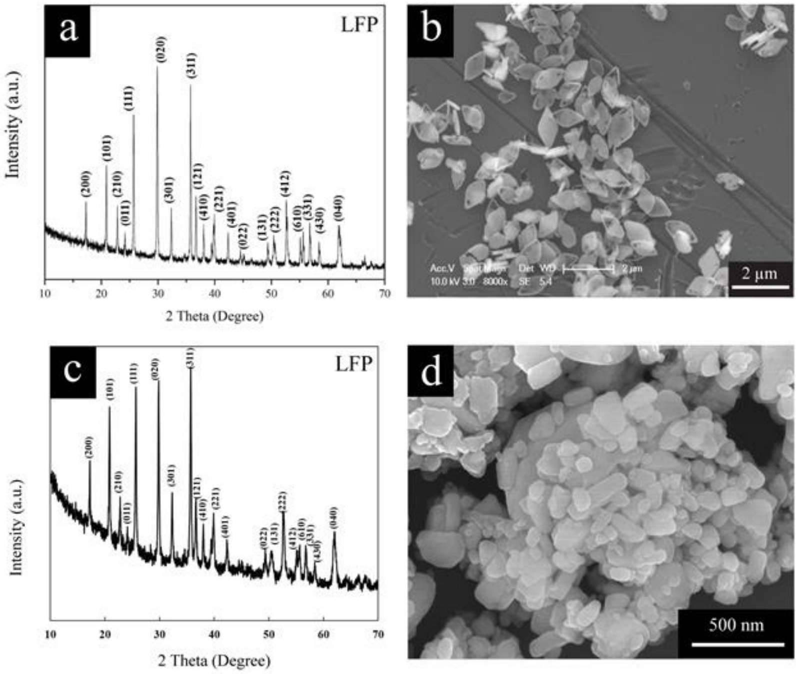

Figure 2.1 (a) XRD pattern and (b) SE micrograph of synthesized LFP after solvothermal. (c) XRD pattern and (d) SE micrograph of synthesized LFP after the ball milling process.

Subsequent ball milling produced more isotropic LFP particles with XRD spectrum indicate pure LFP with a less dominant (020) peak (Figure 2.1(c)). SE micrograph (Figure 2.1(d)) confirms isotropic morphology as shown in Figure 2.1(d). The average particle size was measured with TEM and was determined to be 35±6 nm (Figure S1, supplementary material). These particles were subsequently annealed and characterized to determine crystal growth kinetics.

-Phase transformation

XRD analysis of samples annealed at 300, 400, 500, 600, 700, and 800 °C for 180 min are shown in Figure 2.2. Those annealed at or below 700°C indicate pure LFP, but a Fe_2P impurity phase was observed at 800 °C. As expected, the FWHM of peaks decreases with increasing temperatures, indicating that the crystals are larger and that grain growth occurred.

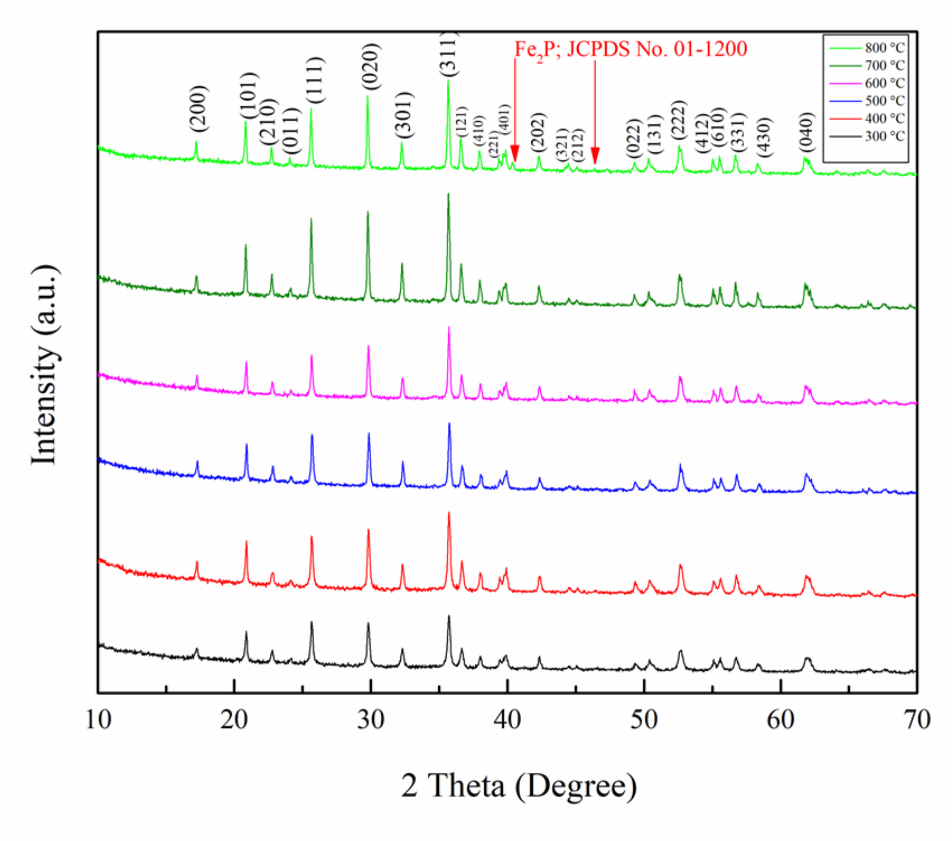

Figure 2.2 XRD patterns of LFP heated at 300, 400, 500, 600, 700, and 800°C for 180 min in 5% H_2/95% N_2 atmosphere.

Microstructural analysis

Depicted SE micrographs of LFP samples annealed at different temperatures in 5% H_2 / 95% N_2 for 1 h are shown in Figure 2.3. There is almost no observable grain growth from 300-500 °C, but growth was observed at higher temperatures as the shape of particles developed into round shapes, indicating that material was added to the particle edges.

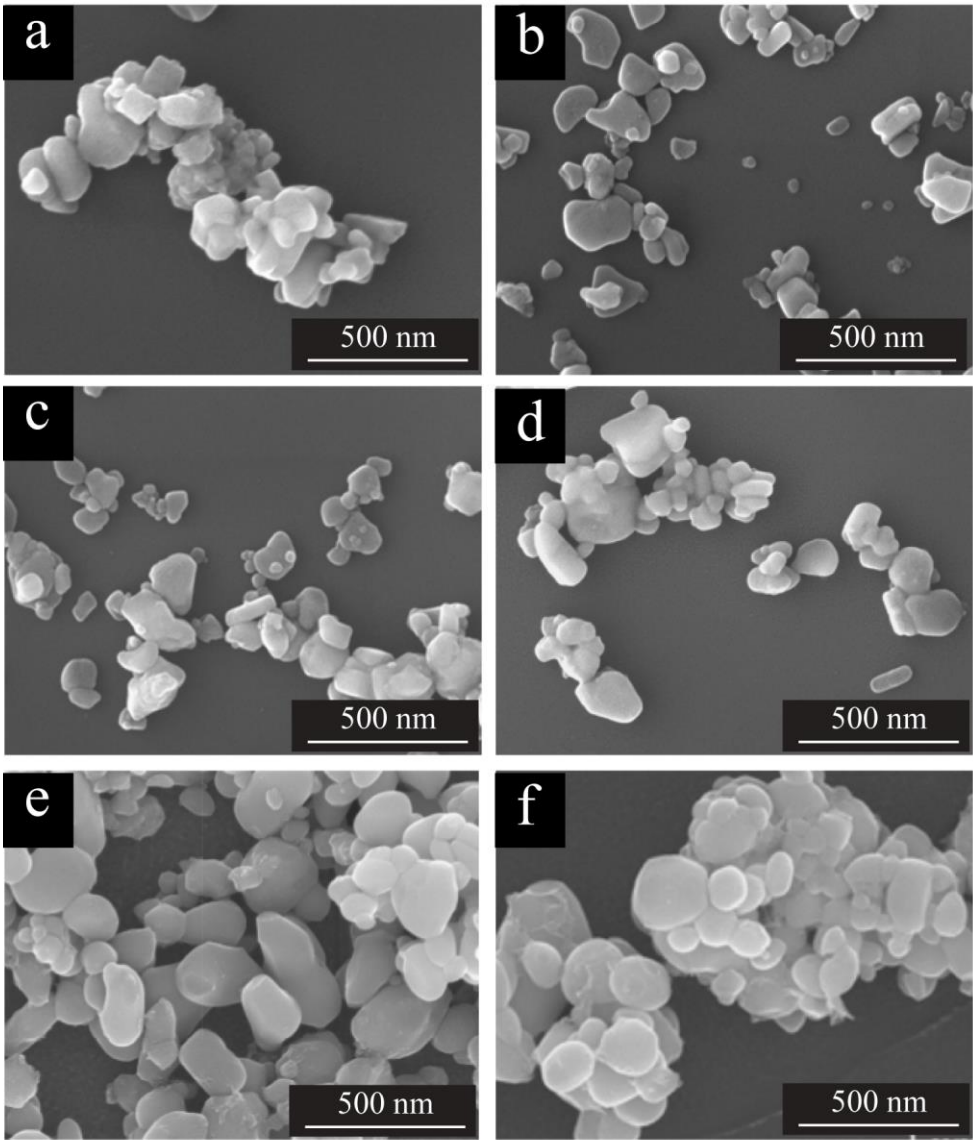

Figure 2.3 SE micrographs of LFP annealed at (a) 300°C, (b) 400°C, (c) 500°C, (d) 600°C, (e) 700°C, and (f) 800°C in 5% H_2 / 95% N_2 atmosphere for 1 h.

Figure 2.4 shows the average crystal diameter increasing with heat treatment times and temperatures for samples annealed at 300, 400, 500, 600, and 700 °C. Based on the slopes in the plot, there are 3 regions of crystal growth, described sequentially as follows:

minimal change (300-400 °C), significant growth (400-600 °C), and rapid increase (600-700 °C). This significant grain size increase at 600 and 700 °C suggests that some grains must shrink or disappear. The driving force for these temperatures is the energy difference between fine and large grains. This leads to the decrease in grain boundary and also total boundary energy.[87]

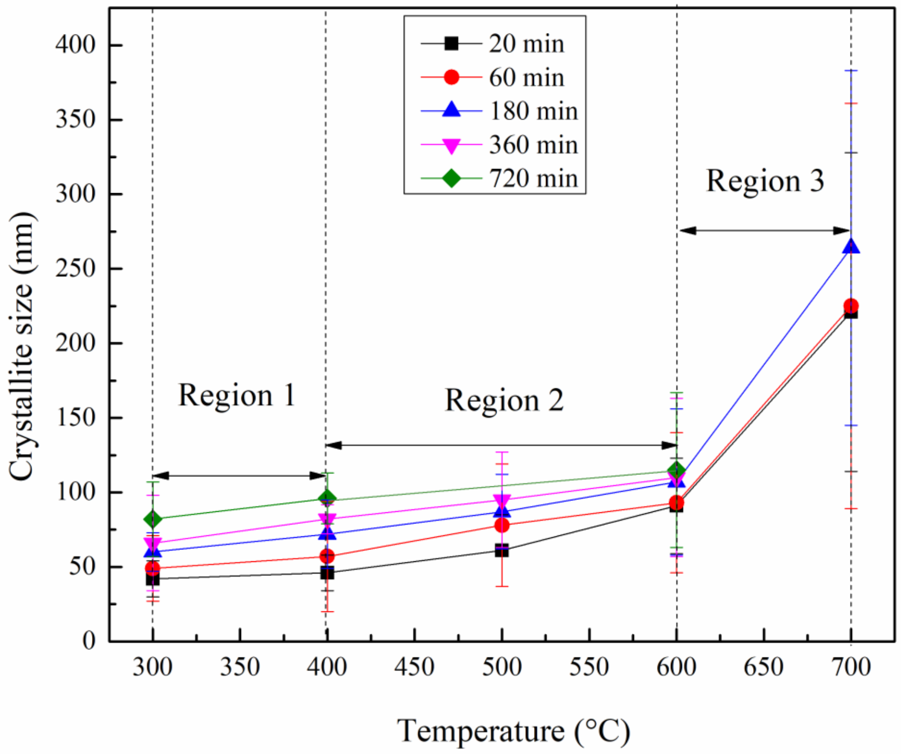

Figure 2.4 Average crystal diameters of LFP annealed from 300°C - 700°C for 20 min, 60 min, 180 min, 360 min, and 720 min. in 5% H_2 / 95% N_2 atmosphere.

Depicted bright field TE micrographs of LFP annealed at 400, 500, 600, and 700 °C for 3 h show crystal size increasing from 72±23 nm to 87±25 nm, 107±49 nm, and 264±119 nm, respectively (Figure 2.5). As measured previously, annealed particles at 600°C and 700°C were rounded corresponding to SE micrographs. Necks between these particles were observed, significantly at 700 °C.

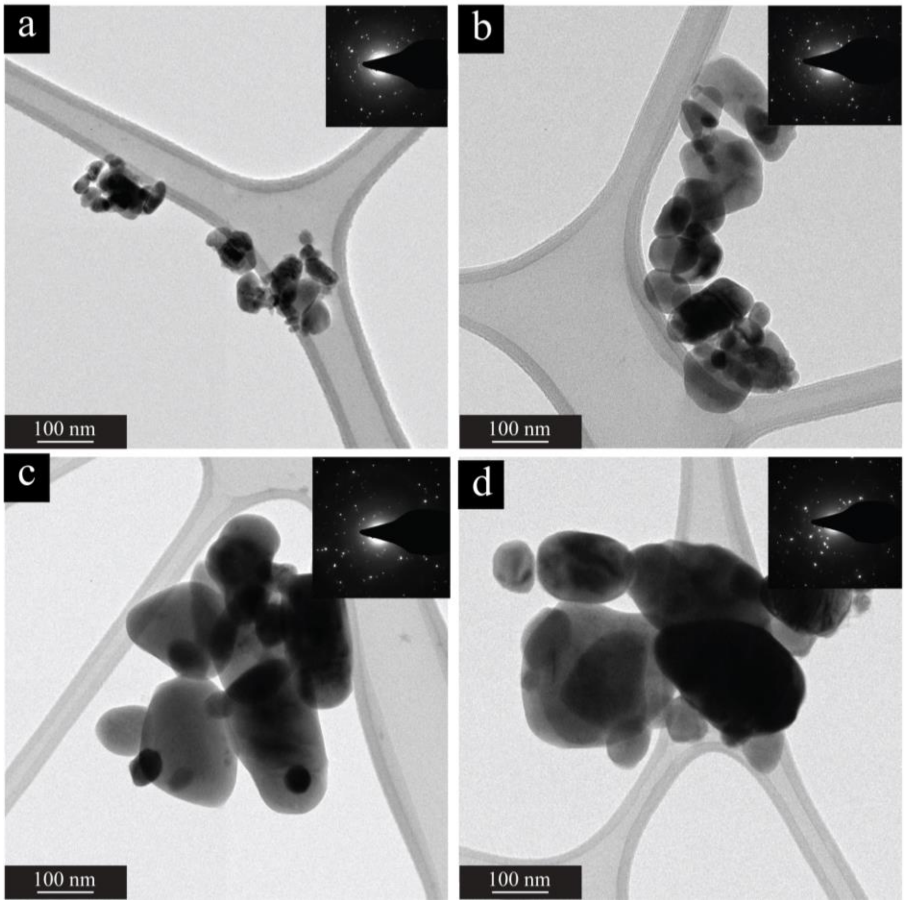

Figure 2.5 Bright field TE micrographs of LFP annealed at (a) 400°C, (b) 500°C, (c) 600°C, and (d) 700°C for 180 min. SAED insets in (a)-(d) confirmed LFP.

Growth mechanisms

In LFP manufacturing, sintering occurs during calcination or in a post-calcination heat treatment step, and it causes changes in grain size and shape, as well as pore size and shape. The driving force of sintering is similar to grain growth lowering the surface free energy across multiple particles by eliminating solid-vapor interfaces. Changes in the partial pressure and free energy along the particle surface affect material transfer. Adjacent particles tend to fuse together, starting with the formation of a thin neck, which grows through various diffusion processes, as shown in Figure 2.6. In surface diffusion, atoms can be transferred along a particle surface to a grain boundary or interface between two particles. During volume diffusion, atoms diffuse within the crystals from either the surface or the grain boundary area. Grain boundary diffusion is when atoms diffuse from an internal grain boundary to the grain boundary edge.

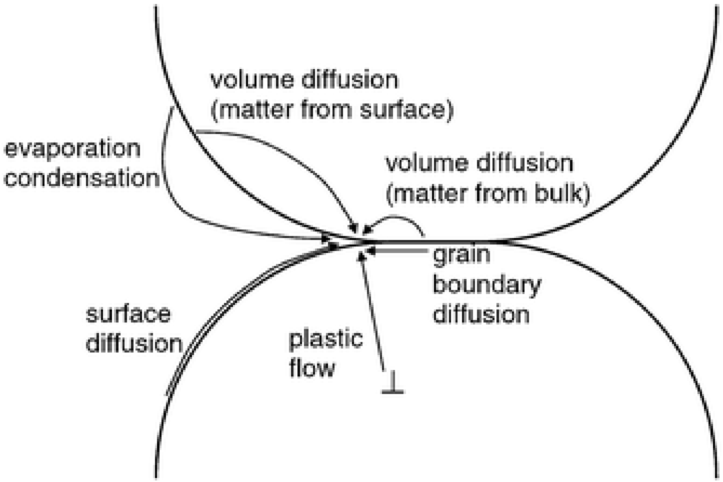

Figure 2.6 Transport mechanisms during the initial stage of solid state sintering stage [88-89].

The growth of average crystallite size with time can be explained using the theory developed by Lifshitz, Slyozov, and Wagner (LWS)[90] (equation 2.2).

$$D - D_0 = kt^{\frac{1}{n}} \tag{2.2}$$

Where D is the growth of individual crystals of average grain diameter.

t is time

D_0 is the initial crystallite size at $t = 0$

k is a temperature dependent parameter of the crystal growth rate

n is an exponent that describes the rate controlling mechanism [91-93]

$n = 2$, interface controlled

$n = 3$, volume diffusion controlled

$n = 4$, grain boundary controlled

$n = 5$, surface diffusion controlled

However, this exponent n can be found from 1.7 to 10 [94-95].

Then the crystal growth in the experiments can be determined by

$$\ln(D - D_0) = \frac{1}{n}\ln t + \ln k \tag{2.3}$$

We plot the relationship between ln(D-D_0) and ln(t) at different temperatures to calculate n and understand the mechanism of crystal growth. The slope plotted from this equation usually ranges from 0.1 to 0.5 as solute aggregation and particle size tend to inhibit grain growth [87, 92]. Thus, the experimental n values are often higher than the actual values.

The plots of LFP grain size at temperature between 300°C to 700°C are shown in Figure 2.7. Linear fits were calculated for each temperature and used to determine the grain growth exponent *n* using equation (2.3).

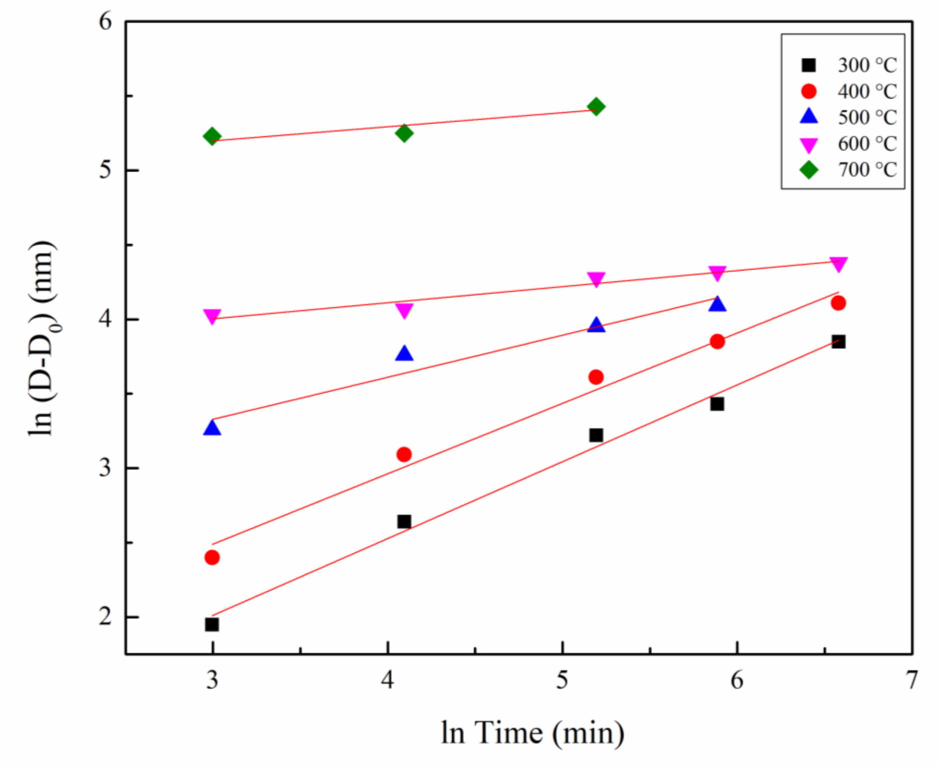

Figure 2.7 Relationship between crystal diameter and annealing time from 300 to 700°C in 5% H_2 / 95% N_2 atmosphere.

At an annealing temperature of 300 °C, $n = 1.9$, indicating the grain growth process is in a transient period since $n < 2$ [96]. The *n* value at 400°C is 2.1, which represents interface control of normal grain growth by diffusion of ions along the matrix-particles boundary[97, 98-99]. This grain growth was driven by grain boundary curvature[97]. This process does not result in a decrease of the distance between particle centers. When LFP was annealed at 500°C, $n = 3.54$. This indicates the crystal growth is controlled by volume diffusion of ions in the matrix[100]. A similar phenomenon was reported in Usta et al., during heat treatment of Magnesium silicide (Mg_2Si) particles at 590 °C with $n = 3.8$ [93].

Compared to other materials such as hydroxy apatite (HA) and zirconium dioxide (ZrO_2) that have the same n value ($n \sim 2$), LFP shows the bulk diffusion of ions along the matrix-particle boundary mechanism at 400 °C. Meanwhile, the bulk diffusion of HA and ZrO_2 occur at 1020 and 1600 °C, respectively. This lower heat requirement in LFP is due to the difference in bond strength and melting temperature such as the grain boundary diffusion of alumina (Al_2O_3) relates to the ionic bonding strength. At the molecular level of crystals, the atomic energies are different due to an electric dipole. The polarity of the polar bond increases with the increasing anion-cation orbital energy difference. ZrO_2 exhibits ionic bond, but LFP and HA exhibit ionic and covalent interactions [101]. However, zirconium dioxide has a higher melting temperature (monoclinic <1,170 °C, tetragonal 1,170–2,370 °C, and cubic >2,370 °C) than hydroxy apatite (1250 °C).

At 600 and 700°C, n values are 9.26 and 10.57, respectively, so the above model cannot be used. As a metal or ceramic is heated, grain growth can occur. Smaller grains will shrink and disappear, often being consumed by larger gains, causing those grains to grow. The driving force for this process is the reduction of energy associated with grain boundaries by decreasing the total grain boundary area and eliminating solid-vapor interfaces. The Gibbs free energy is associated with grain boundaries is given by the equation:

$$\Delta G = \gamma V\left(\frac{1}{r_1} + \frac{1}{r_2}\right) \tag{2.4}$$

Where ΔG is the change in free energy on going across the curved interface

γ is the boundary energy

V is the molar volume across a curved surface

r_1 and r_2 are the radii of curvature of the contacting grains

If two grains share a flat facet, growth will depend on the angle between edges once the shared facet ends. Grain growth will occur if the grain boundary energy (γ_{gb}) is less than the solid/vapor surface energy (γ_{sv}). This depends on the dihedral angle (ϕ) between the grains, which can be determined using equation 5.

$$\gamma_{gb} = 2\gamma_{sv}\cos\frac{\phi}{2} \tag{2.5}$$

If the dihedral angle is 120°, which is the case of two hexagonal grains sharing a face, the surface energy and boundary energy will be equal.

We observed the grain boundaries meet to form angles approximately 44° and 105° from samples annealed at 600°C for 20 min and 360 min, respectively (Figure 2.8(a-d)). The dihedral angles 104° and 111° were measured from the samples annealed at 700°C for 20 min and 360 min (Figure 2.8 (e-h)). Based on the equation (2.5), this means the interface of these two grains reached equilibrium for atom or vapor phase transformation[87].

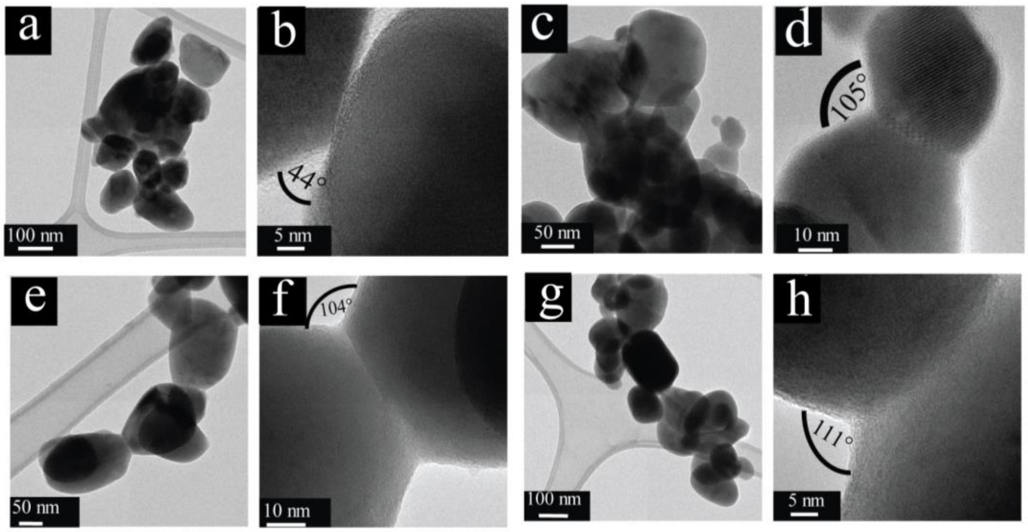

Figure 2.8 Bright field TE micrographs of LFP annealed at 600°C for (a and b) 20 min and (c and d) 360 min. Annealed at 700°C for (e and f) 20 min and (g and h) 360 min.

Based on the rate constant, k, from equation (2.3), an Arrhenius eqution[102] was used to calculate activation energies.

$$k = Ae^{\frac{-E_a}{RT}} \tag{2.6}$$

Where A is the pre-exponential factor

E_a is the activation energy

R is the universal gas constant

T is absolute temperature in Kelvins

The natural logarithm of Arrhenius' equation can be written as

$$\ln(k) = \frac{-E_a}{R}\left(\frac{1}{T}\right) + \ln(A) \tag{2.7}$$

The plot of $\ln(k)$ versus $1/T$ can be use to determine E_a for crystal growth. The activation energy for temperature range of 300-400 °C is 26 kJ/mol and, the temperature of 500-600 °C is 36 kJ/mol. These values correspond to the diffusion mechanism in the temperature ranges.

Conclusions

We investigated LFP crystal growth processes at differrent annealing temperatures and holding times. We found that LFP particles fuse together to eliminate of the solid/vapor interfaces and reduce particle surface energy, thus creating grain boundaries. The grain boundaries grow through different mechanisms depending on the annealing temperature. We also identify Fe_2P as an impurity phase that occurred when LFP is anneal at 800 °C for 3 h. From these results, we can establish the annealing process parameters to optimize crystal size and morphological features that influence to energy density, capacity, and cyclic stability of Li-ion batteries.

Supporting Information

Investigation of the crystal growth kinetics of $LiFePO_4$ during annealing

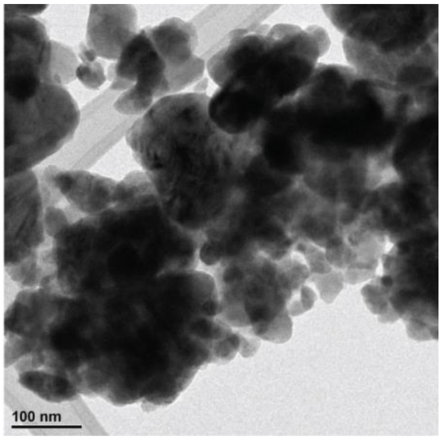

Figure S1. TE micrograph of synthesized LFP after the ball milling process.

Chapter 3

Bio-inspired crystallization of Li-ion cathodes

Bio-inspired crystallization of Li-ion cathodes

Abstract

A biologically inspired strategy for synthesis of Li-ion materials uses polyacrylic acid (PAA), which serves a similar function as polypeptides that regulate supersaturation in many biominerals. This was used to investigate the effects of templating molecules on the size and shape of synthesized LiFePO4-Carbon (LFP/C) composite particles. The resulting particle size, distribution, shape, and crystal orientation are dependent on time and PAA concentration under solvothermal conditions. From these observations, a mechanism is proposed for the crystallization pathway of LFP in the presence of PAA.

3.1 Introduction

$LiFePO_4$ (LFP) is a promising cathode candidate used in second generation of Li-ion batteries (LIBs) due to its non-toxicity, high thermal and cycling stability, and low cost. LFP is a polyanion compound with the olivine structure and has a high theoretical capacity (170 $mAhg^{-1}$)[2, 4]. LFP powders are synthesized using a variety of methods including solid-state reactions [103-104], sol-gel processing [86, 105-106], and solution-precipitation [105, 107-108] However, these processes often lead to the formation of inhomogeneous compositions, irregular morphologies, and uncontrollable particle growth that results in unpredictable electrochemical performance. Thus, a low temperature synthesis procedure that controls morphology, particle size and crystallite size is needed.

Biomineralized composites provide elegant hierarchical structures with unique properties and performance. These hierarchical structures are dictated by structural organics, which in combination with functional organics, serve as scaffolds that control the nucleation and growth of mineral with a precision unmatched by current synthetic methods. For example, the nacreous inner layer of the California red abalone (*Haliotis rufescens*) is an intricate composite consisting of aragonite ($CaCO_3$) tablets surrounded by an organic matrix (Figure 3.1). This organic matrix consists of a β-chitin framework, which supports aspartic acid-rich proteins that serve as nucleation sites for mineral formation. [109] The carboxylate groups of the aspartic acid moieties bind to Ca^{2+} ions, not only inhibiting precipitation by controlling supersaturation and stabilizing the mineral precursor in a gelatinous state, but also by forming site-specific nucleation points. Through controlled dehydration of the mineral precursor, single crystalline aragonite tablets nucleate and grow to fill the 3-dimensional chitinous scaffold [61, 110-111].

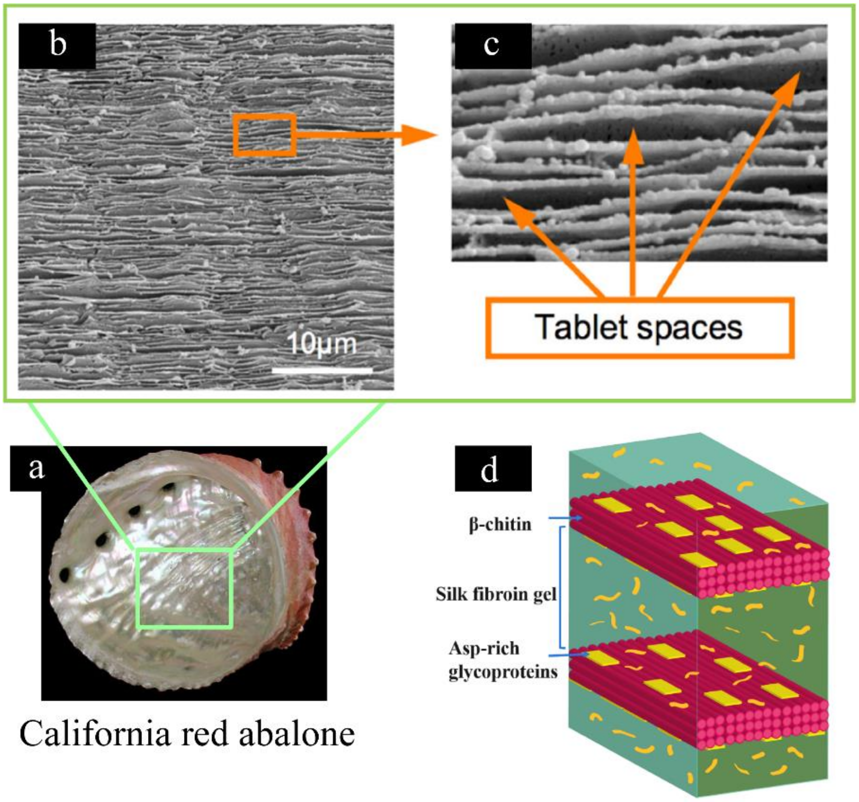

Figure 3.1 (a) California red abalone shell (b and c) Porous β-chitin organic scaffold revealed by dissolution of calcium carbonate tablets (d) Proposed model showing β-chitin scaffold with adsorbed Asp-rich glycoproteins which control crystal nucleation. The silk-like proteins are in a hydrated gel like state [112].

Classical crystallization

These biological crystallization pathways cannot be explained using classical nucleation theory. In classical nucleation theory (CNT), homogenous nucleation has been studied for over 70 years, originating with work by Gibbs in late 1800s [113]. Based on the CNT, crystals nucleate by adding monomeric solution species such as atoms, molecular complexes, or colloids in order to grow a particle. In most cases, nucleation events are heterogeneous, where preciptiation occurs along any surfaces (e.g., reactor walls, solid materials in the reactor, etc.) and interfaces in clean solutions. In reality, it often begins on solid impurities such as dust or gas bubbles. Nucleation on a surface is more favored when the interface energy of the crystal being formed with the substrate is lower than crystals formed in free solution [114]. Classical nucleation theory also shows that particles can grow when the chemical potential of the solid phase less than the solution phase [113].

Nonclassical crystallization

A variety of non-classical crystal growth mechanisms have been identified in the investigation of nucleation and growth processes in biological structures [115].

In a biological system, minerals can be deposited from aqueous solutions and crystallization can be shifted from thermodynamic to kinetic control. These kinetic crystallization pathways lead to the formation of different polymorphs, differing in thermodynamic stability, melting point, solubility, and mechanical properties[113] The different activation energy barriers to nucleation, growth, and phase transformation control these polymorphs [113, 116].Figure 3.2 highlights the various crystallization pathways under thermodynamic and kinetic control. Crystallization pathways under kinetic control can be composed of intermediate phases or particles between each step such as dissolution recrystallization, aggregation, and solid phase transformation[114, 117].

According to Wolfgang Ostwald's rule, several products can be found in a reaction, resulting in a formation sequence of phases in the crystallization event which is kinetic control of crystallization in non-classical pathways [16, 115, 118]. Typically, a less-dense phase will form first and densify later until the densest, most stable phase formed. Each step of the metastable phase sequence depends on the solubility of the minerals and free energies of activation of nucleation, which are strongly influenced by additives.

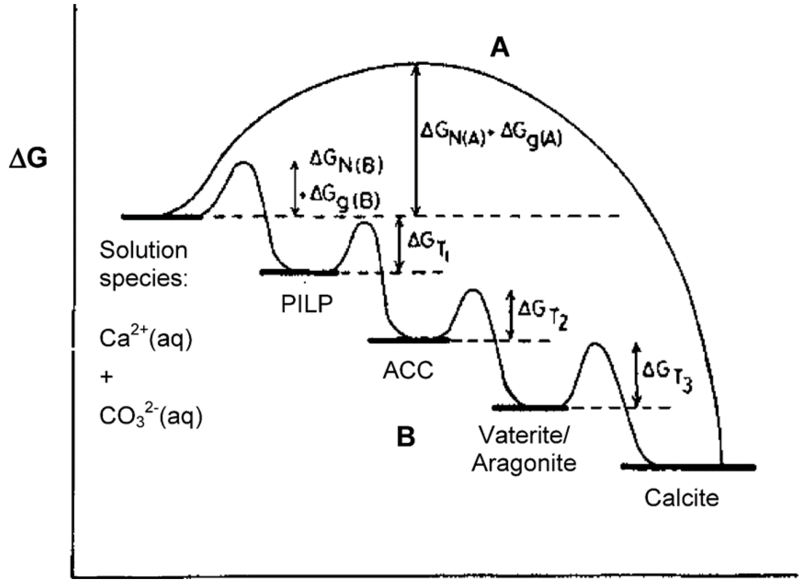

Figure 3.2 Classical and non-classical crystallization processes. In pathway (A) the system flows on one step route to the final phase. In pathway (B), the multiple steps for precipitated minerals (sequential precipitation) route depend on the free energy of activation related with (n) nucleation (g) growth, and (t) phase transformation[119].

As mentioned, the kinetic control is based on the modification of the activation energy barriers of nucleation, growth, and phase transformations. It can be achieved by high supersaturation then promote a rapid particle nucleation[114]. Figure 3.3 schematically compares the classical and non-classical processes. Mesocrystals can be obtained from a particle-mediated nonclassical pathway or self-assembly to form superstructures.

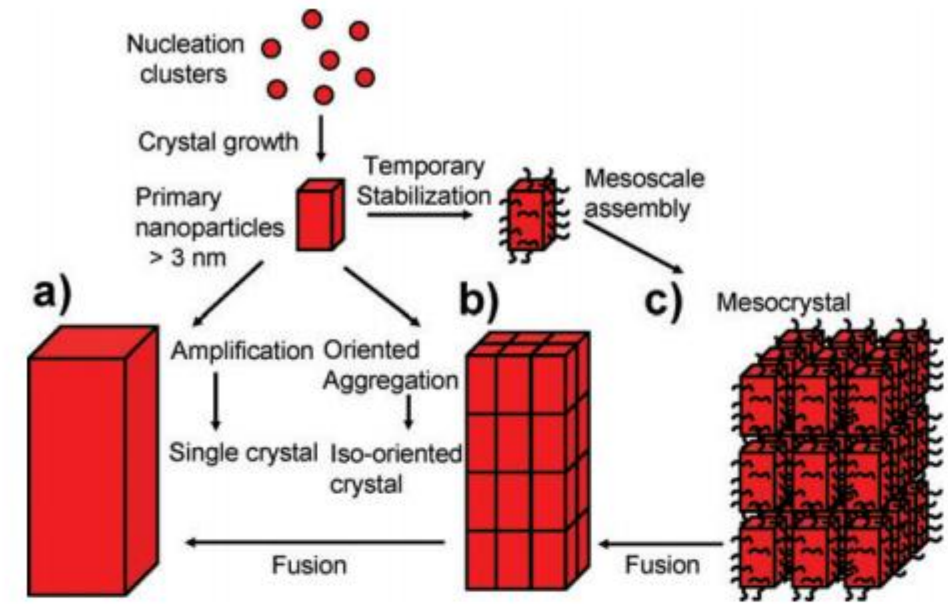

Figure 3.3 Schematic of classical and nonclassical crystallization pathway [120].

If additives are present in the system, they can interact in multiple ways to form amorphous or crystalline intermediates. In non-classical pathways, the least dense phase will form first and the densest forms last. The most thermodynamically phase also forms by metastable phases. If there are enough nucleation centers that provide the dissolving of metastable phase, it can be act as a template to nucleate the stable on the metastable phase.

The different aspects of non-classical nucleation and growth, including a number of bio-inspired systems, are described below:

Precursor formation

Non-classical crystallization is applied to systems far from equilibrium. The precursor structures from this pathway are difficult to detect. If crystallization is inhibited amorphous precursors will form, otherwise the precursors will be liquid or nanocrystalline [114].

Amorphous precursors

In many mineral systems, amorphous precursors are the first species to form in a crystallization pathway, especially in systems that have low precursor or intermediate phase solubilities [114]. Crystalline and amorphous materials can coexist in early stages of crystallization[121]. Typically, transformation occurs through local dissolution and re-precipitation caused by the release of water from a hydrated phase. This can result in the formation of a new crystalline phase. For example, amorphous calcium carbonate (ACC) is an initially hydrated phase that forms in an aqueous calcium carbonate solution [122]. When the ACC dissolves, it returns calcium ions to the solution, which then crystallize as calcite once the solution becomes supersaturated [122-123].

Liquid precursors

There has been a lot of research on bio-inspired syntheses of calcium carbonate ($CaCO_3$) due to its abundance in nature (e.g., as the main mineral component of mollusk shells as well as in limestone) where specific control of size in biomineralized organisms have been demonstrated[124]. Gower et al. have developed an amorphous calcium carbonate precursor (ACC) system using polymers such as sodium salts of poly(aspartic acid) and poly(glutamic acid) to stabilize the mineral from precipitation as crystalline domains[125-126]. They proposed liquid-like amorphous intermediate phases form during the process of precipitation of $CaCO_3$. For example, polyelectrolytes are added into a calcium chloride solution to form Ca-ion bound polymer solutions. Subsequently, ammonium carbonate vapor is gradually diffused into a Petri dish containing the calcium chloride-polymer solution. This process, termed “polymer-induced liquid-precursor” (PILP) process, has been used to describe this process. The first step in this process is reached where liquid-liquid phase separation occurs in the solution. Then, highly hydrated droplets of amorphous precursor (containing the polymer and mineral) are formed. Next, these droplets coalesce into films and crystallize to form thin films (Figure 3.4) and tablets[119], spheres[127], or fibers[119, 126].

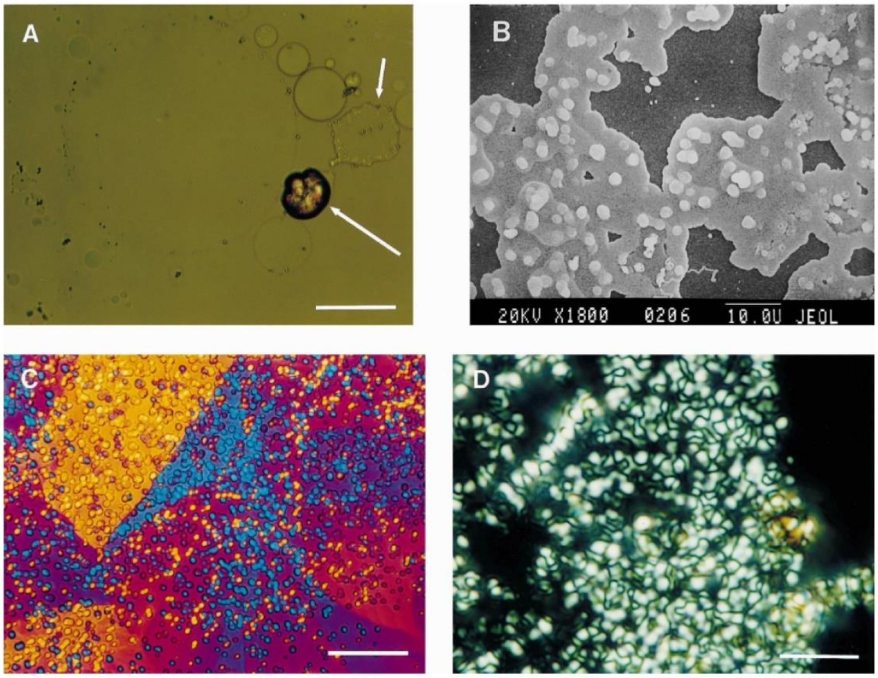

Figure 3.4 Liquid-precursor phase (a) PILP droplets on the surface of an air bubble (b) Scanning electron micrograph illustrates the large droplets likely formed by the agglomeration of smaller droplets. (c) The polarized optical micrograph shows different orientations of calcite. (d) dark field micrograph of solidified droplets (Scale bar = 20 microns) [126].

Crystalline nanoparticles

In some systems, nanocrystals form without progressing through an amorphous phase, and then aggregate to form larger crystals. The highly-ordered structures of crystalline nanoparticles influence particle-particle interactions due to an uneven distribution of surface charge on their rough surfaces. Nanoparticle structure depends on atomic bonding, particle morphology, and surface construction [115]. For example, the nanoparticle structure of 3 nm ZnS can be changed in response to its environment. This leads to a different in distortion and surface interactions of core shell structure [128].

Oriented attachment[114]

In oriented attachment, nanocrystals will attach themselves to a larger crystal with common crystallographic orientation. The interfaces of these particles join together, eliminating two high-energy surfaces by crystallographic fusion. Oriented attachment can occur in one, two, or three dimensions as shown in Figure 3.5.

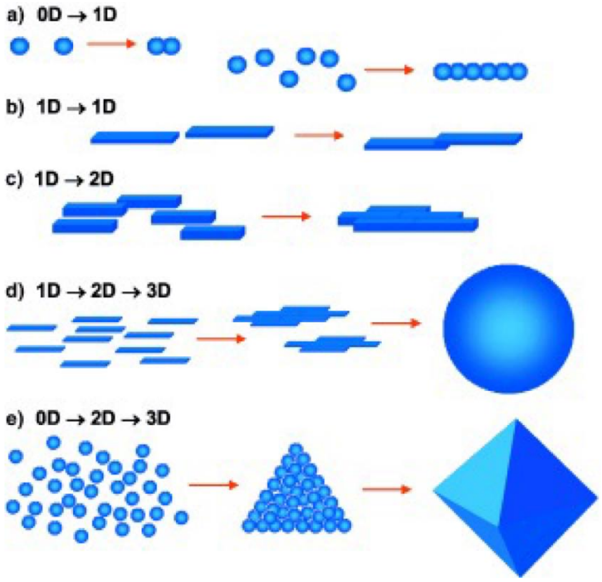

Figure 3.5 Schematic of self-construction of nanostructures by oriented attachment [129].

The first evidence of oriented attachment was found for Titanium dioxide particles synthesized by the hydrothermal method as shown in Figure 3.6. Oriented attachment was also observed in $LiFePO_4$ particles using the solvothermal method (Figure 3.7).

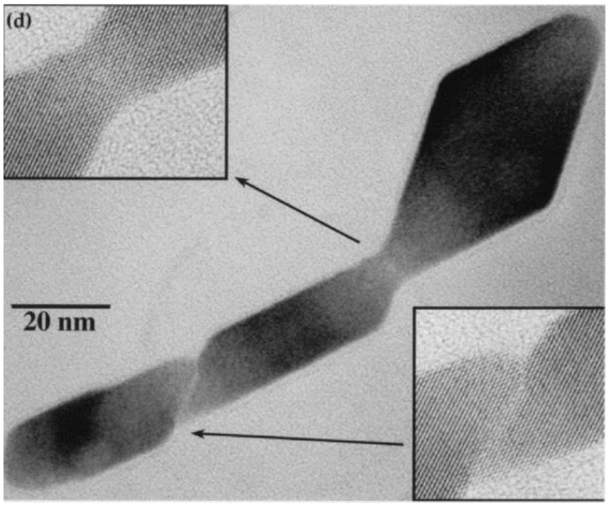

Figure 3.6 Single crystal fusion of anatase via oriented attachment with magnified inset of the attachment interfaces [130].

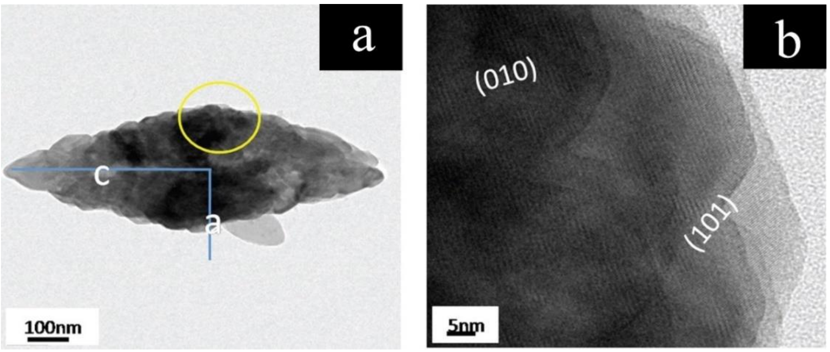

Figure 3.7 Polycrystalline $LiFePO_4$ reveals oriented attachment and crystals are aligned in [001] and [100] directions, Reprinted with permission from (Jianxin Zhu, Joseph Fiore, Dongsheng Li, et al, Solvothermal Synthesis, Development, and Performance of $LiFePO_4$ Nanostructures, Crystal Growth and Design, American Chemical Society). Copyright (2013) American Chemical Society [83].

Mesocrystals

Mesocrystals are colloidal crystals built from individual nanocrystals and aligned in a common crystallographic direction. Sea urchin spines and nacre are the good examples of mesocrystalline structures. Mesocrystals can consist of multiple interspersed phases. For example, two phases where one phase is oriented crystalline nanoparticles and another phase is amorphous. Figure 3.8 shows an example of a calcite mesocrystal that synthesized using double-hydrophilic block copolymers as additives to modify the morphology of calcite particles [131].

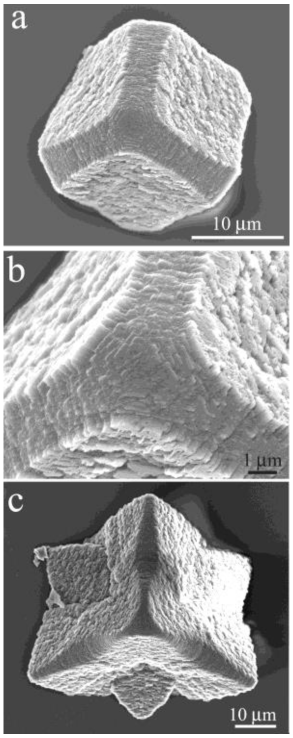

Figure 3.8 Calcium carbonate crystals precipitated from a solution containing 1 mM Ca and PEO22-PNaStS49 at a copolymer concentration such that the [Ca]:[S] molar ratio was (a) 2.5:1 and (b and c) 1.25:1 [131], "Reprinted with permission from (Alex N. Kulak, Peter Iddon, Yuting Li, et al, Continuous Structural Evolution of Calcium Carbonate Particles: A Unifying Model of Copolymer-Mediated Crystallization Mar 1, 2007). Copyright (2007) American Chemical Society."

Additional Bio-inspired methods of non-classical nucleation:

Beyond the PILP work by Gower et al., others have demonstrated the use of non-classical crystallization pathways using bio-inspired methods. Xu et al. reported that the presence of poly(styrene-alt-maleic acid) (PS-MA) can modify the crystal growth of $CaCO_3$ to form a superstructure by mesoscale assembly of anisotropic nanoparticle subunits[132]. Pipich et al. studied the nucleation and growth of $CaCO_3$ mediated by ovalbumin from egg white. This former example would be considered "bio-mediation" rather than bio-inspired since they utilized an actual biological protein to control the growth of mineral. In this work, they found amorphous particles formed after an induction period of about 1.5 h, subsequently redissolved and transformed to crystalline polymorphs of $CaCO_3$ (vaterite and aragonite)[133]. Oaki and Imai synthesized superstructures of potassium sulfate (K_2SO_4)/polyacrylic acid (PAA)/dye composite. PAA molecules are strongly incorporated within a microscopic 2D structure. This results in specific adsorption of PAA molecules on the crystal faces. At high concentrations of PAA, an excess of PAA molecules act as growth medium that leads to diffusion controlled conditions. This effects crystal morphology leading to helical and twisted morphologies[134-135]. Therefore, using polymer-mediated methods can act as bio-inspired pathways, acting like proteins that are used to modify particle size, size distribution, shape, orientation and morphology.

Herein, we utilize a biologically inspired strategy to synthesize LFP by using PAA, which serves a similar function to polypeptides that regulate supersaturation in many biominerals, to study its effects on the size and shape of synthesized LFP/C composite particles. We investigate the resulting particle size, distribution, shape, and crystal orientation as a function of time and PAA concentration under solvothermal conditions.

3.2 Experimental Section

Preparation of precursors and LFP/C particles:

$LiOH.H_2O$, $FeSO_4 \cdot 7H_2O$, and 85 wt % H_3PO_4 were used as LFP precursors with a molar ratio of 3:1:1(Table S1, Supporting Information). The lithium hydroxide and ferrous sulfate were dissolved in degassed Milli-Q water separately and stirred at room temperature for 20 min until a gray suspension was obtained. PAA, (M_w = 1800 g/mol) was dissolved in Milli-Q water and mixed with the $LiFePO_4$ precursor suspensions to yield reaction mixtures. By modifying the concentrations of polymer, $[Fe^{2+}]$:$[COO^-]$ ratios of 1:0, 10:1, 4:1, 2:1, 1:1, 1:2 and 1:10 were obtained. 10 mL suspensions of precursor were transferred to 23 mL-capacity Teflon-lined autoclaves and argon gas was flowed across the head space to reduce the amount of oxygen to inhibit the oxidation of Fe^{2+}. The room temperature autoclaves were sealed and placed in a convection oven that was preheated to 200°C. The autoclaves were heated for up to 150 min, and their temperature was monitored using a thermocouple inserted and sealed within the reactor. The temperatures corresponding to the reaction times are listed in Table 3.1. After heating for the prescribed times and cooled, products were transferred to centrifuge tubes and precipitates were collected and washed with deionized water 3 times and ethanol twice with intermittent 1 minute probe sonication to ensure unused precursor was removed. Collected powders were then dried in a vacuum oven at 70°C for 12 h.

Table 3.1 Autoclave Temperature During Reaction

Reaction Time (min)	**Reactor Temperature (°C)**
0	25
14	47
40	135
60	170
90	190
150	200

***Characterization*:**

Crystallinity and phase of the powder products were determined by X-ray powder diffraction (XRD, Panalytical Empyrion) using Cu Kα radiation. The Scherrer method was used to calculate the crystallite size based on measurement of the full-width at half maximum (FWHM) of diffraction peaks. Particle sizes and morphologies were observed by Scanning Electron Microscopy (SEM, Nova Nano 450) at 10 kV accelerating voltage. Adobe Photoshop® was used to measure particle sizes. Transmission Electron Microscopy (TEM, at 120 keV, FEI Tecnai 12 and Titan Themis 300 STEM, at 300 keV) was used to observe morphologies, crystallite sizes (especially for crystals > 50 nm), crystal orientation, and phase of reaction products. The surface areas of samples were measured via BET nitrogen adsorption using a Micromeritics Tristar 3000. Fourier Transform Infrared spectroscopy (FTIR, Nicolet 6700) was used to identify any residual polymer while Raman spectroscopy (Horiba LabRam) was used to confirm the state of carbon species (e.g., graphitic carbon) in the synthesized materials.

Electrochemical performance

R2032 type coin cells were used to investigate the electrochemical performance of LFP samples. As-synthesized LFP powder (the active material), conductive carbon black, and poly (vinylidene fluoride) (PVDF) were mixed in a 78:14:8 wt % ratio and dispersed in N-methylpyrrolidone (NMP) to produce a viscous slurry. The slurry was cast on aluminum foil and dried in a vacuum oven at 120°C for 12 h. After that, the cells were assembled in an Ar-filled glove box with lithium metal foil as the negative electrode, trilayer Polypropylene-polyethylene-polypropylene membrane (Celgard) as a separator, and 1.0 M $LiPF_6$ in ethylene carbonate–diethyl carbonate (50:50 vol%) as an electrolyte solution. Cyclic voltammograms were performed on a VMP3 multichannel electrochemical station from 2.7 to 4.2 V at room temperature. The rate capacity and charge-discharge cycler of batteries were tested at room temperature using Arbin battery test system (Arbin Instruments, model BT2043)

3.3 Results and Discussion

Effect of PAA on LFP crystallinity and morphology

In order to determine the effect of PAA on resulting LFP crystal sizes and morphologies, a series of syntheses were performed with varied quantities of polymer added to the precursors in solvothermal reactors for different durations at 200°C. Product morphologies were investigated with and without PAA using SEM and TEM (Figure 3.9).

In the absence of PAA, smooth, plate-like LFP particles measuring 1300 nm long and 100 nm thick were produced (Figures 3.9a and 3.9b). Selected Area Electron Diffraction (SAED, Figure 3.9c) revealed the single crystalline nature of these particles. Based on the SAED analyses, the large faces in Figures 3.9a and 3.9b correspond to the (010) planes (*ac* planes). D-spacings of 1.03 nm and 0.42 nm corresponding to the {100} and {101} lattice fringes, respectively, of LFP can be observed (Figure S1, Supporting Information).

The addition of PAA clearly affected the morphologies and sizes of LFP particles (and crystal sizes, Figures 3.9d, 3.9g, 3.9j, and Figure S2, Supporting Information). Small additions of polymer (i.e., $[Fe^{2+}]:[COO^{-}]$ 10:1) yield LFP particles that also display a plate-like shape (Figure 3.9d), similar to those observed without polymer. However, the surface of these particles appears textured, suggesting that these particles consist of aggregated primary particles. Indeed, further analyses by bright field TEM and SAED (Figures 3.9e and 3.9f, respectively) revealed that these particles consisted of highly textured 30-50 nm primary nanocrystals assembled to form nearly-single crystalline larger particles that are 300-1000 nm in length and 100-500 nm in width. SAED also indicates that the primary nanocrystals were aligned and oriented along the [101] direction and interconnected along the [020] direction (Figure S3, Supporting Information).

SEM micrographs show that with increasing polymer content (i.e., $[Fe^{2+}]:[COO^{-}] = 4:1$) a combination of larger (300-600 nm) and smaller (30-50 nm) isotropic particles formed (Figures 3.9g and 3.9h). Bright field TEM (Figure 3.9h) and SAED (Figure 3.9i) of the larger particles confirmed their aggregated nature, highlighting smaller (30-50 nm), aligned nanocrystals growing along [020] direction. This suggests that the smaller crystals observed in Figure 3.9g are assembled into larger, oriented particles. This assembly has been previously observed with LFP synthesized under hydrothermal conditions, where large quantities of primary particles observed at short reaction durations assembled into hierarchically arranged secondary particles [136]. The crystallite size was decreased from 69 nm ($[Fe^{2+}]:[COO^-] = 1:0$) to 49 nm ($[Fe^{2+}]:[COO^-] = 4:1$) due to a diffusion control mass transport of adsorbed PAA on the crystals [137].

Finally, high concentrations of added PAA (i.e., $[Fe^{2+}]:[COO^-]$ 1:2) led to the formation of larger (700-1000 nm) spherical secondary particles that consisted of 30 nm primary particles (Figure 3.9j and 3.9k). Yet, even at these larger concentrations of polymer, the resulting secondary particles appeared nearly single crystalline (Figure 3.9l). At even higher PAA concentrations, such as $[Fe^{2+}]:[COO^-]$ 1:10, SEM and TEM observations show polycrystalline particles about 100-700 nm composed of 2-3 nm secondary particles (Figure 3.9m, 3.9n, and 3.9o). Here, it is likely that PAA adsorbed onto the nucleating LFP crystals and suppressed their growth through diffusion controlled mass transport. [18] In addition, adding polymer in the reactions regulated the supersaturation from the fromation of PAA/Fe^{2+} complex. Therefore, the supersaturation is low in high concentration of PAA resulting in less free Fe^{2+} in the solution for nucleation.

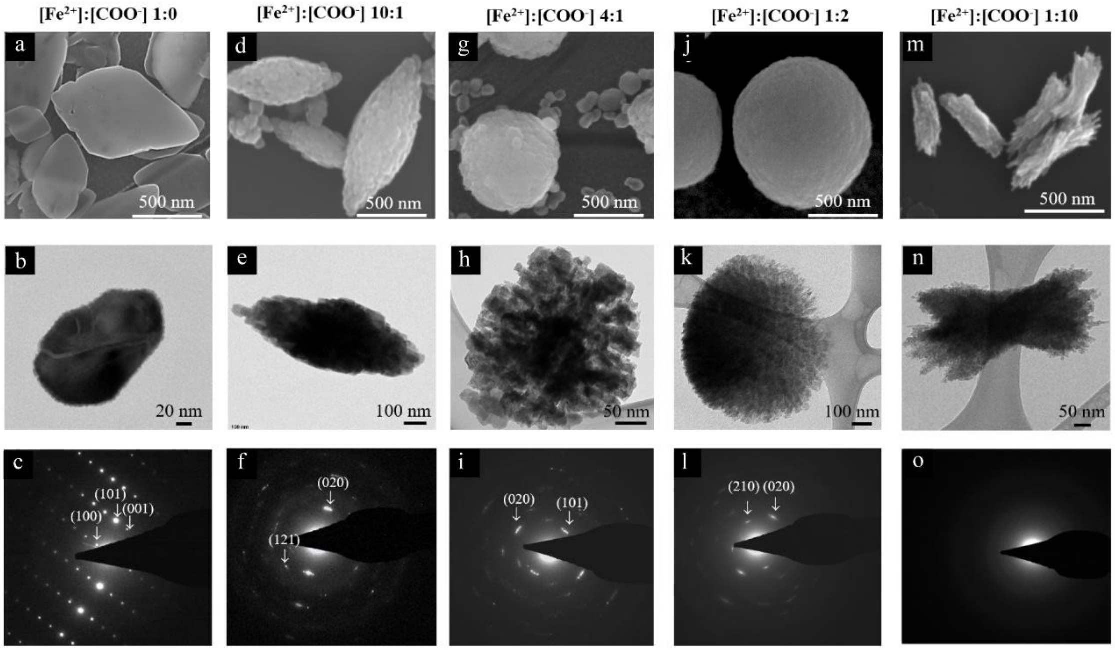

Figure 3.9 Characterization of the samples synthesized for 150 min, reactor temperature200°C. (a) SEM micrograph of plate-like structure of LFP, (b) bright field TEM micrograph, and (c) SAED indicating (100), (101), and (001) planes of LFP crystal with a [010] zone axis of sample obtained at [Fe^{2+}]:[COO^{-}] 1:0. (d) SEM micrograph highlighting aggregated of primary particles, (e) bright field TEM micrograph with corresponding (f) SAED of the sample prepared from [Fe^{2+}]:[COO^{-}] 10:1 confirmed the nanocrystals were aligned along [020]. (g) SEM micrograph of small and large spherical LFP and (h) bright field TEM micrograph show growth of LFP in the presence of [Fe^{2+}]:[COO^{-}] 4:1, corresponding (i) SAED highlights (020) and (101) planes with a zone axis of [20-2]. (j) SEM micrograph of spherical LFP prepared from [Fe^{2+}]:[COO^{-}] 1:2 and (k) bright field TEM micrograph highlighting the assembled secondary particles, with corresponding (l) SAED pattern showing (020) and (210) planes of nearly single crystal. (m) SEM micrograph of lamella branches prepared from [Fe^{2+}]:[COO^{-}] 1:10 (n) bright field TEM micrograph illustrates the assembled secondary particles, with corresponding (o) SAED pattern showing amorphous or nanocrystals.

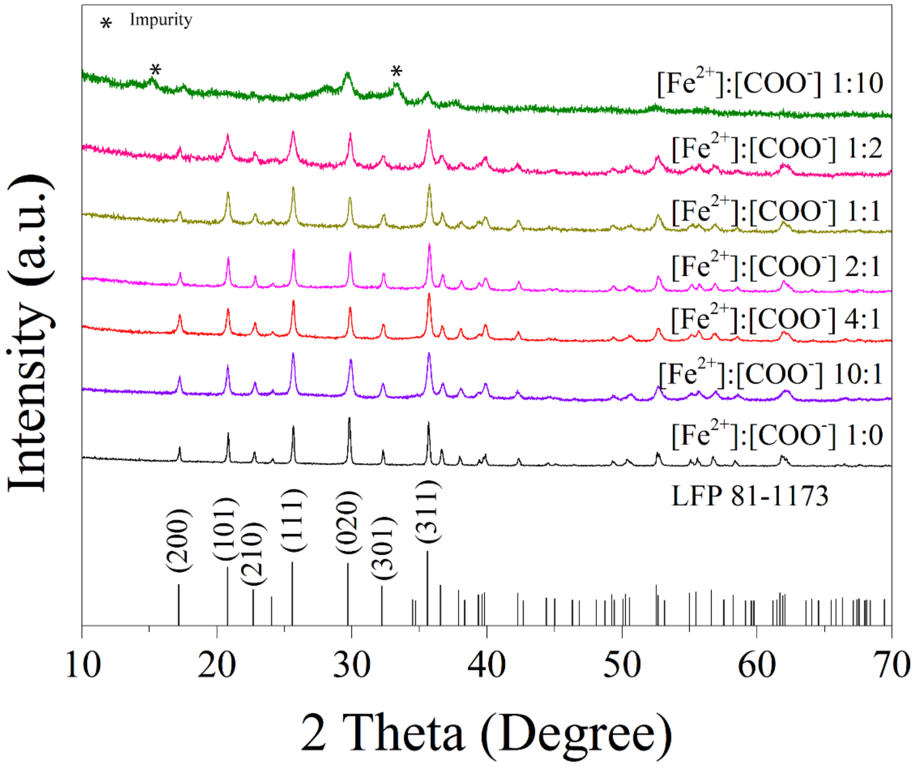

Figure 3.10 XRD patterns of LFP samples synthesized with different PAA concentrations for 150 min, reactor temperature 200°C.

X-ray diffraction confirmed TEM observations that show crystalline LFP was obtained for all materials (with or without PAA). Without PAA (Figure 3.10), the (020) reflection has the highest intensity, in agreement with the TEM results. The diffraction peaks of particles synthesized with PAA are broader and the intensity of the (020) reflection is slightly reduced relative to its intensity in LFP without PAA, suggesting that PAA modifies the growth behavior of LFP. At extremely high concentrations of PAA (i.e., $[Fe^{2+}]:[COO^{-}]$ 1:10, a weakly nanocrystalline LFP forms as well as an unidentified impurity phase.

Measurements of the full width at half maximum (FWHM) of diffraction peaks reveals an increase in peak width with increasing PAA concentration. Without PAA, the crystal size of LFP at 150 min reaction duration is 69 nm (+/- 12 nm) continuously decreasing (Table S1, Supporting information) to 15 nm (+/- 1 nm) when using $[Fe^{2+}]:[COO^{-}]$ 1:10. These observations confirming that the addition of polymer modifies the growth behavior of LFP.

It is highly likely that polymer is adsorbed to the LFP primary particles and becomes entrapped within secondary particles. Thermogravimetric analysis (TGA) of PAA-mediated LFP particles show that the quantity of adsorbed PAA ranges from approximately 3 to 10 wt% with increasing concentration of PAA (Figure S4, Supporting Information).

In fact, FTIR analysis of powders synthesized for 150 minutes and reactor temperature 200°C at different PAA concentrations show that the spectra not only strongly correlate with crystalline phosphates [138] (Figure 3.11), but that PAA still exists, even after washing. For example, peaks are observed at 1412 and 1460 cm^{-1} in samples with ratios of $[Fe^{2+}]:[COO^{-}]$ 2:1, 1:2, and 1:10. These peaks can be assigned to C-O stretching vibration and CH_2 bending, respectively. The peak at 1563 cm^{-1} due to -C=O or C=C stretching was found for $[Fe^{2+}]:[COO^{-}]$ 10:1, 2:1, 1:2, and 1:10 samples. A weak peak of CH_2 or C-H stretching was also observed in $[Fe^{2+}]:[COO^{-}]$ 1:2 and 1:10 samples, and the carbonyl dispersion band at 1722 cm^{-1}, which is the characteristic peak of bulk carboxylic acid dimers ($\nu C{=}O$)[139], also confirmed that the PAA was adsorbed on the surface of LFP crystals.

Also, broad peaks of O-H stretching at 3540 cm^{-1} were found [140-141]. Additionally, splits near the PO_4^{3-} bands in samples with PAA at 986, 1052, and 1101 cm^{-1} were detected. This could be due to symmetry changes in the phosphate complex. This suggests that there are multiple species of LFP and PAA present on the surfaces, which result in multiple surface complexes of electrostatic attraction of COO^- and Fe^{2+} [142].

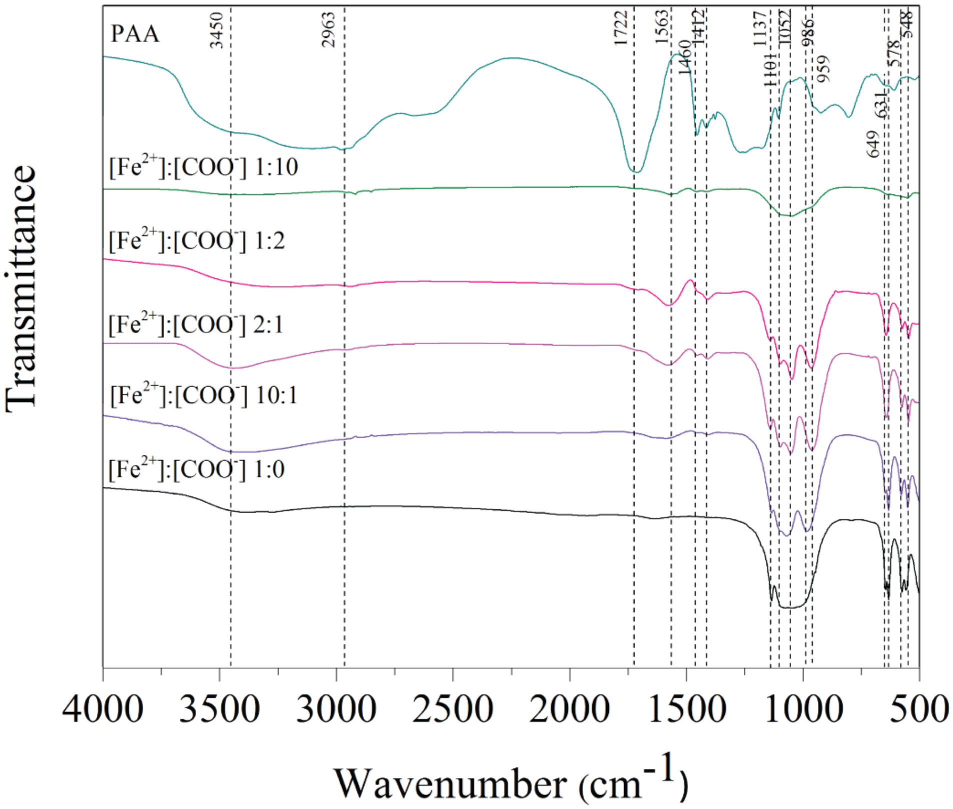

Figure 3.11 FTIR spectra of pure PAA, [Fe^{2+}]:[COO$^-$] 1:0,10:1, 2:1, 1:2, 1:10 synthesized for 150 min, reactor temperature 200°C.

In order to understand the formation of LFP powders at different PAA concentrations, a set of syntheses at shorter reaction durations was conducted. At 60 minutes reaction duration (170°C), XRD (Figure 3.12) reveals pure LFP (JCPDS No. 81-

1173) for samples with [Fe^{2+}]:[COO^-] 1:0, 10:1, and 4:1 ratios. With increasing PAA concentration above the 4:1 ratio (i.e., [Fe^{2+}]:[COO^-] 2:1 to 1:2), PAA shows a significant influence, severely retarding crystallization.

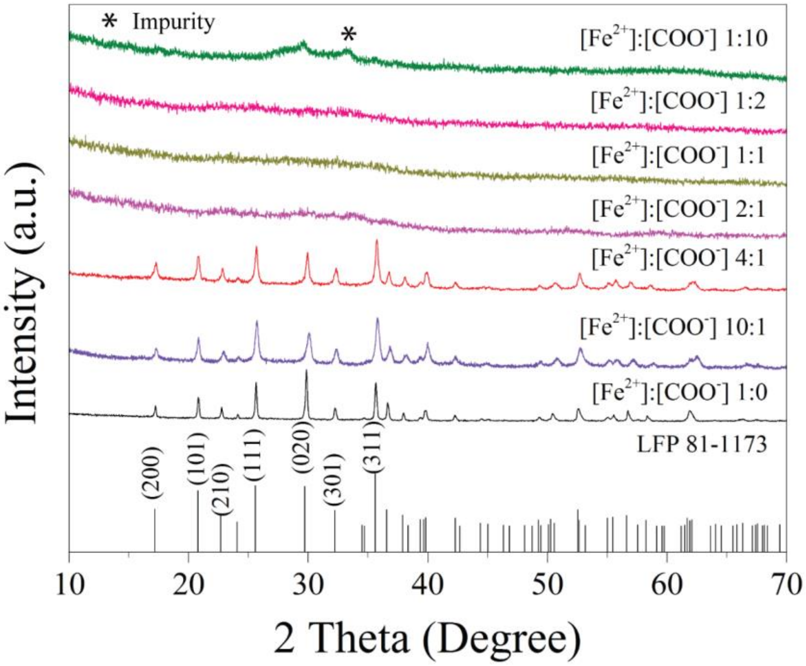

Figure 3.12 XRD patterns of LFP samples synthesized with different PAA concentrations for 60 min, reactor temperature 170°C.

when the concentration of PAA increases to [Fe^{2+}]:[COO^-] 1:10 along with an impurity phase, which is likely sodium phosphate Na_3PO_4 (JCPDS No. 01-084-0195). Similar to samples heated for 150 minutes, those heated to 60 minutes also showed the presence of PAA adsorbed on LFP particles, even after extensive washing (Figure 3.13).

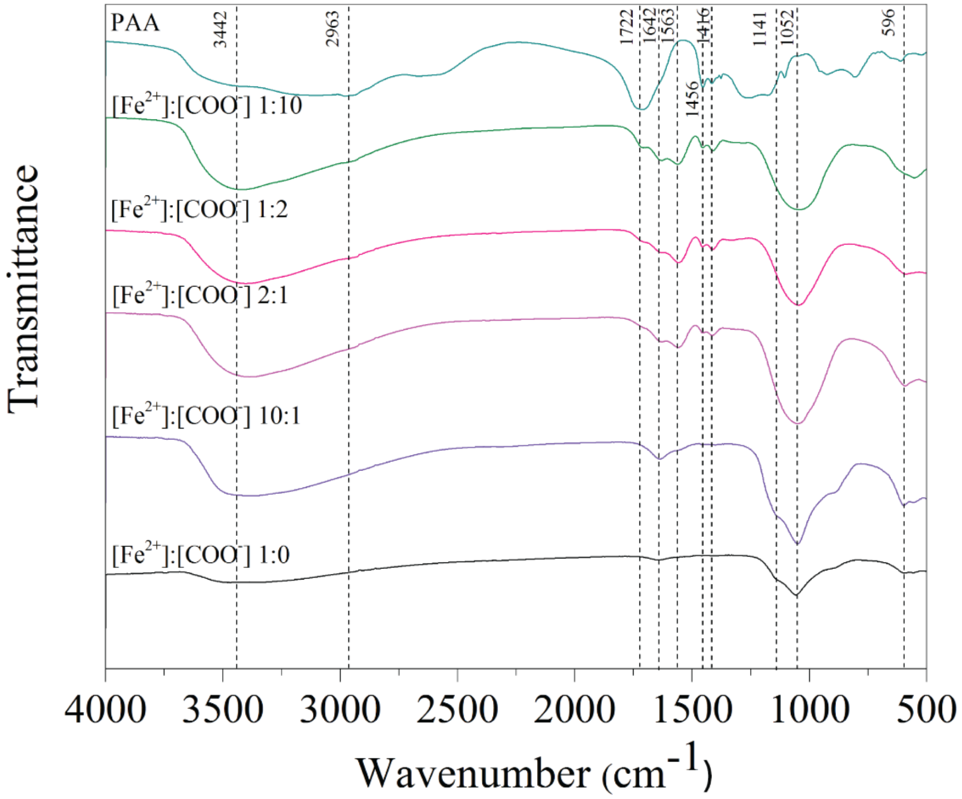

Figure 3.13 FTIR spectra of pure PAA, $[Fe^{2+}]:[COO^-]$ 1:0,10:1, 2:1, 1:2, 1:10 synthesized for 60 min, reactor temperature 170°C and pure PAA.

Peaks from C-O stretching coupled with O-H in plane bending are found at 1416 cm^{-1}. The peak at 1456 cm^{-1} was assigned to CH_2 bending. The peaks found at 1563, 1642, and 1722, cm^{-1} are characteristic of COO^- asymmetric, -C=O or C=C stretch, or -C=O from free COOH. Finally, the peaks at 2963 and 3442 cm^{-1} were assigned to CH_2 or C-H stretching and the broad peak of O-H stretching [140-141]. In addition, bands of phosphate at 596 cm^{-1} of $\nu_4PO_4^{3-}$, 1052 cm^{-1} of $\nu_3PO_4^{3-}$, and 1141 cm^{-1} of HPO_4^{2-} were detected. Broad bands observed in samples [Fe^{2+}]:[COO^-] 2:1, 1:2, and 1:10, signify amorphous phosphates, in agreement with xrd results [143].

LFP formed under low polymer concentrations

The structural evolution of LFP at a low polymer concentration ([Fe^{2+}]:[COO^-] 2:1) was investigated by heating the reactors for different durations: 14, 40, 60, 90 and 150 minutes. After heating for 14 minutes, bright field TEM (Figure 3.14a) shows ~ 100 nm spherical aggregated particles. SAED highlights a diffuse diffraction ring (Figure 3.14b) suggesting a weakly crystalline material. Analysis of the diffraction rings revealed that vivianite ($Fe_3(PO_4)_2.8H_2O$) nanocrystals were formed. Subsequent dark field analysis (Figure 3.14c) shows that these aggregates consist of very small (~ 3 nm) primary particles that are randomly oriented within secondary aggregates. Lattice imaging of these primary particles (Figure 3.14d) as well as (Figure 3.14e) also confirmed the presence of nanocrystalline VVT. In this initial state, most Fe^{2+} ions were complexed with COO^- from the PAA, limiting the number of Fe^{2+} ions available in solution for LFP nucleation. However, unbound Fe^{2+} formed VVT as it is known to form first in the system without PAA [83].

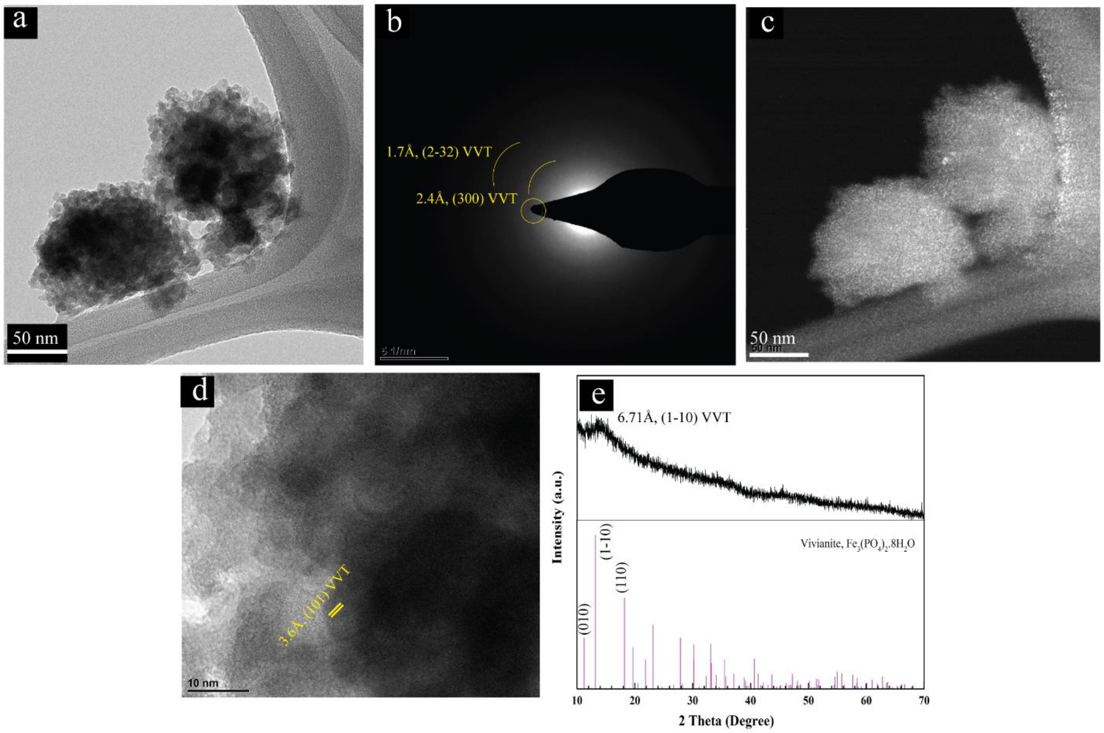

Figure 3.14 LFP [Fe^{2+}]:[COO^{-}] 2:1 synthesized for 14 min (reactor temperature = 47°C). (a) Bright field TEM micrograph and (b) SAED with diffuse rings, corresponding to VVT, (c) dark field TEM micrograph showing randomly oriented nanocrystals (~ 3 nm diameter), (d) High resolution TE micrograph shows lattice fringes of nanoparticles. (e) XRD of weakly nanocrystalline VVT.

After 40 min reaction duration (135°C), thin plates of vivianite with small particles and clusters of nanocrystals appeared (Figure 3.15a, b). Powder XRD verifies vivianite as the main phase present (Figure S5, Supporting information). SAED (Figure 3.15c) also has diffuse rings, indicating amorphous or weakly nano-crystalline particles. Analysis of another region (Figure 3.15(d)) shows 40-80 nm aggregates that, through electron diffraction (Figure 3.15(e), were confirmed to consist of nanocrystalline LFP. Dark field TEM (Figure 3.14f) of one of the clusters reveals these particles are comprised of 2-3 nm

LFP primary particles. Based on previous work [35] that showed VVT dissolves with a reduction in pH below 6, and the observation that even with small amounts of polymer, the pH still decreases, it is likely that the initially formed, but weakly nano-crystalline VVT (which will have a high radius of curvature) is also dissolving here. The slowly dissolving and metastable VVT is thus likely to provide a high concentration of nutrient for LFP nucleation (K_{sp} of VVT = $1\text{x}10^{-36}$) [83].

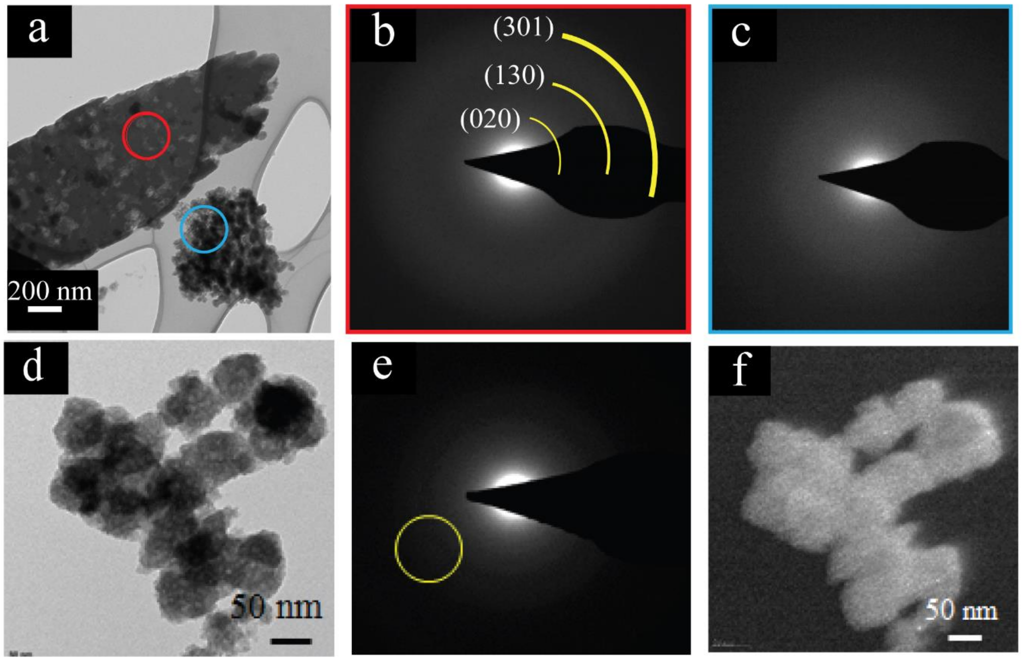

Figure 3.15 Time-study of crystallization of LFP [Fe^{2+}]:[COO^-] 2:1 synthesized 40 min, where the reactor temperature is 135°C. (a) Bright field TEM micrograph of thin plate and cluster of nanocrystals (b) SAED of weakly crystalline nanoparticles of vivianite from region 1 (red circled area), with (c) SAED from region 2 (blue circled area) of nanoparticles showing diffuse diffraction ring as a characteristic of amorphous or weakly nanocrystalline material. (d) Aggregates of nanoparticles showing several nanocrystals interrogated by electron diffraction in (e) and dark field imaging (f**).**

At 60 minutes, the reaction temperature was 170°C. Here, TEM micrographs illustrate the formation of larger aggregates (Figure 3.16a). SAED (Figure 3.16b) reveals that these aggregates consist of nanocrystals with no preferred crystallographic orientation. This was further confirmed by dark field imaging and high magnification TEM (Figures 3.16c and d, respectively).

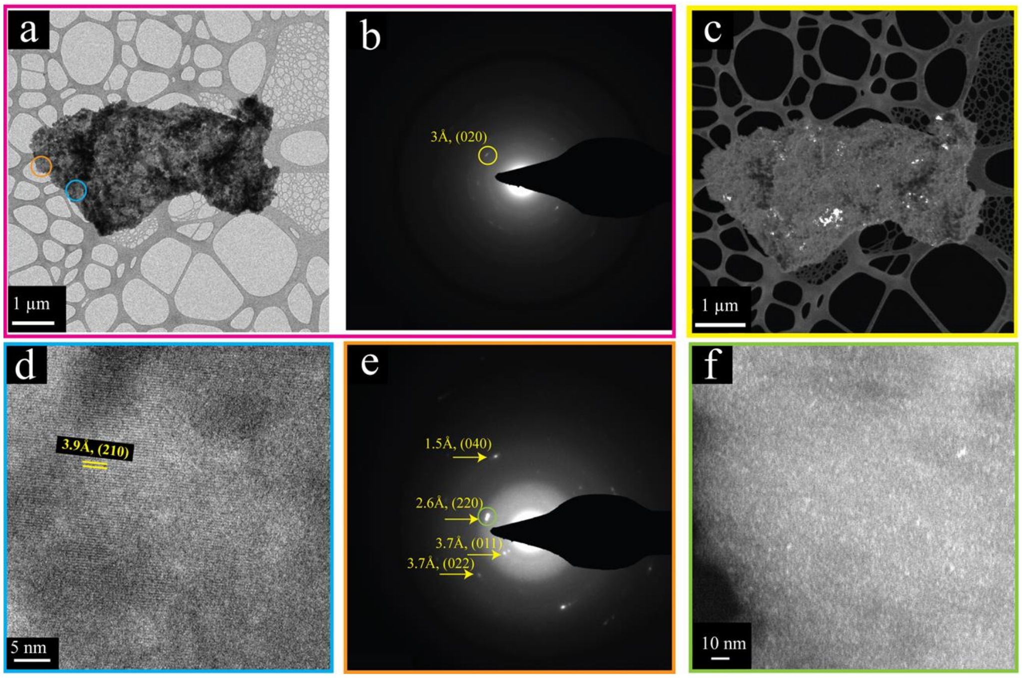

Figure 3.16 Crystallization time-study of LFP [Fe^{2+}]:[COO^{-}] 2:1 synthesized for 60 min, reactor temperature was 170°C: (a) Bright field TEM micrograph and (b) SAED of crystalline nanoparticles, with (c) dark field TEM micrograph showing several nanocrystals that are 25 nm. (d) high magnification TEM micrograph showing lattice planes in randomly oriented LFP crystals. (e) SAED of smaller area of crystalline in orange circle in (a) showing polycrystalline and (f) dark field of (220) showing nanocrystals aligned in that direction.

At 90 minutes, the temperature inside the autoclave increased to 190°C and resulted in an increased number and size of LFP crystals (Figure 3.17a). LFP nanocrystals formed nearly spherical secondary particles with aligned crystals (Figure 3.17b - d). The lattice fringes belonging to the (200) plane were observed in high magnification TEM (Figure 3.17b). SAED of the particle in Figure 3.17a highlights that the particle is nearly single crystalline. Dark field TEM (Figure 3.17d) confirms the high level of ordering in this larger particle, but shows that it is composed of smaller primary particles that are oriented along the <020> direction.

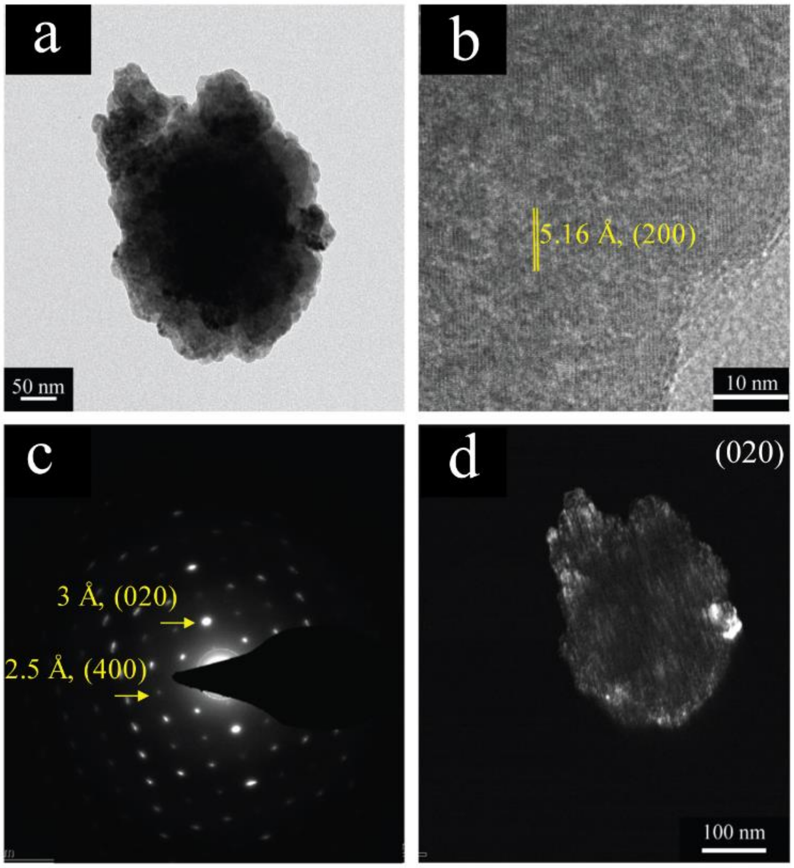

Figure 3.17 Crystallization time-study of LFP [Fe^{2+}]:[COO^-] 2:1 synthesized 90 min: (a) Bright field TEM micrograph, (b) high magnification TEM micrograph, and (c) SAED of crystalline nanoparticles, with (d) dark field TEM micrograph showing several nanocrystals.

To further analyze the particle's internal structure, powder samples were embedded in an epoxy matrix and then cut into thin sections with a microtome. Subsequent analysis by TEM of some of these particles shows a dumbbell-like shaped particle consisting of highly oriented nanocrystals. SAED analysis shows arcs, indicating the crystals are highly oriented in one direction (in the [020] direction), but with some off-axis in plane orientation (Figure 3.18b). Dark field micrographs (Figures 3.18c and 3.18d) of selected reflections from SAED confirm that the orientation of nanocrystals is in the [020] direction perpendicular to [001] direction. This particle structure exhibits characteristic radiating features, suggesting a spherulite-like growth mechanism[144-145]. Here, these particles often form from the polycrystalline growth centers. The second nucleation of new grains occur by growth front nucleation that the new grains nucleate at the surface when solute trapping occurs at the liquid-solid interface with randomize orientation different from the parent crystal which retaining isotropic at large scales. This can be a result of high concentration of PAA that increases a viscosity in a system and limits diffusion of nutrient.

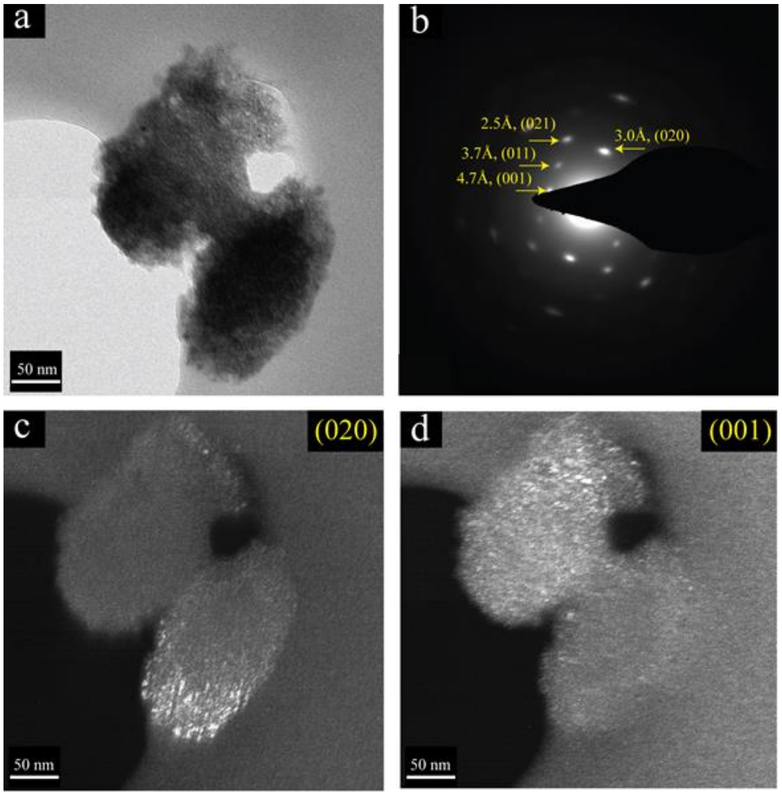

Figure 3.18 Sample cross-section obtained by microtome cuts of LFP [Fe^{2+}]:[COO^{-}] 2:1 synthesized for 90 min (a) Bright field TEM micrograph and (b) SAED of crystalline nanoparticles, with (c and d) dark field TEM micrographs of dumbbell shape showing nanocrystals are aligned. Dark field TEM micrographs were constructed from (020) and (001) reflections.

After 150 min (200°C), the sample consists of powdered granules that are fully grown spheres. The particles were significantly large (ca. 350 nm) that ultramicrotome sectioning was required to investigate their internal structure (Figure 3.19a). SAED of the particles highlights a highly-textured material (Figure 3.19b). Dark field TEM confirms that secondary particles consist of 30-40 nm primary particles aligned along the <001> zone axis (Figure 3.19c). Lattice fringes are clearly observed in Figure 3.19d, and correspond to the (210) face.

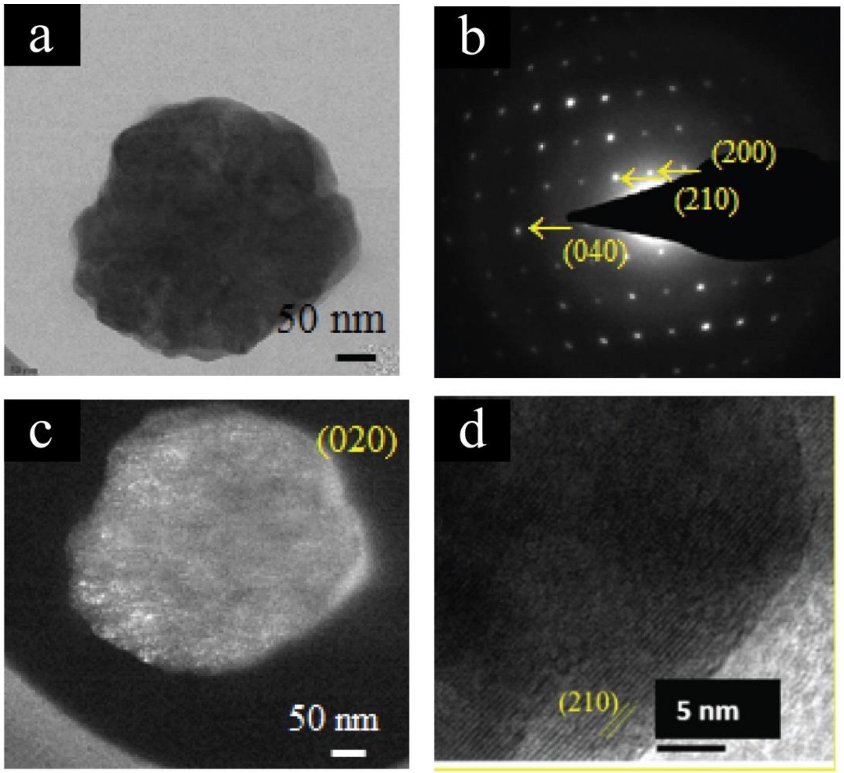

Figure 3.19 (a) Bright field TEM micrograph of spherical particle from [Fe^{2+}]:[COO^-] 2:1 for 150 min, reactor temperature 200 ºC (b) SAED showing (200), (040), and (210) planes with <001> direction of single crystal structure, and (c) dark field TEM micrograph. (d) High magnification TEM micrograph shows lattice fringes of the (210) plane extending across multiple aligned particles.

The development of spherulite growth can be explained by two different mechanisms. Category 1 spherulites are formed by growth from core single crystal nuclei and subsequently branch out to form spheres by a space filling mechanism. Category 2 spherulites grow from needle-like precursor fibers and then branch out in a low-angle from both sides of the fibers. This leads to nearly spherical crystals which can exhibit two eyes on both sides of the nucleation site[145-148]. However, the spherical particles can form by 3-dimensional oriented attachment in the presence of additives [120, 149]. For example, the adsorption of triethanolamine of the surface of ZnO leads to the formation of spheres ZnO sphere by oriented attachment [150].

To further understand the role of PAA in solution, pH values of solutions from the supernatant of reactors at different reaction times (t = 0 to 150 minutes) were obtained (Figure 3.20). Without PAA, the solution pH decreased from ~6 (at t = 0 min) to 4.42 (at t = 150 min). This is due to the deprotonation of H_3PO_4 to H_2PO^{4-} in the solution and mainly the consumption of Fe in the suspensions to form LFP [151]. When the ratios of PAA were $[Fe^{2+}]$:$[COO^-]$ 10:1, 2:1, and 1:10, the final pH decreased from ~ 6 (at t = 0) to 4.63, 5.22, and 5.84, at 150 min respectively. This suggests that carboxylate groups in PAA act as buffering agents that can stabilize the pH of reactions, as indicated by the reduced rate of pH change, by absorbing protons released from phosphoric acid. In fact, these negatively charged carboxylate moieties within the PAA molecules also sequester ferrous ions (Fe^{2+}) [39], preventing their release into solution, reducing supersaturation and thus inhibiting LFP formation.

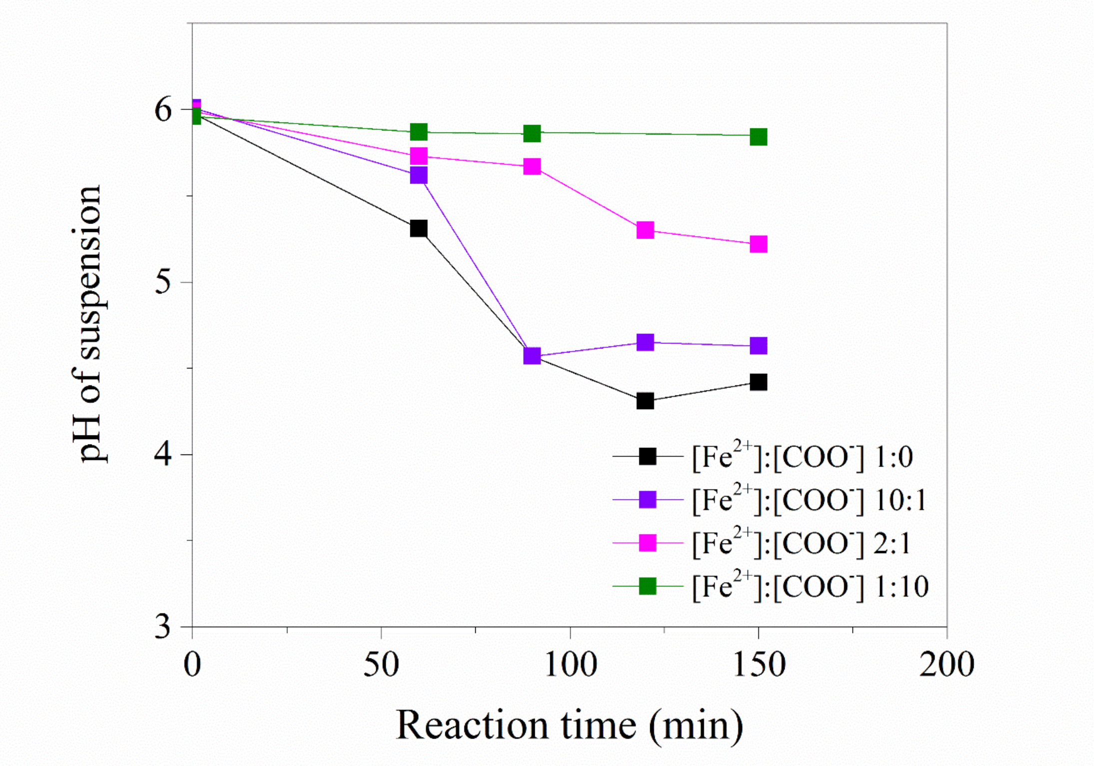

Figure 3.20 Relationship between pH of the supernatant and reaction times at various PAA concentrations.

In fact, this binding of carboxylate groups in PAA to Fe^{2+} ions effectively reduce the concentration of ferrous ions in the supernatant after short reaction times and confirms that PAA retards LFP crystallization (Figure 3.21). Without PAA in the reaction media, Fe^{2+} concentrations at early stages was low due to Fe^{2+} ions being consumed to form vivianite (VVT) $Fe_3(PO_4)_2 \cdot 8H_2O$ (decrease concentration of Fe^{2+} ions in the solution). Subsequently, VVT particles slowly dissolve, releasing Fe^{2+} ions back into the solution as a nutrient to forming LFP [83]. This leads to increase of Fe^{2+} concentration in the solution. Lower ratios of $[Fe^{2+}]:[COO^-]$ represent stronger increased chelation of COO^- with Fe^{2+} in the solution, leading to fewer free Fe^{2+} ions in solution to form LFP crystals and therefore delay in nucleation formation was observed due to less nutrient to form LFP [152].

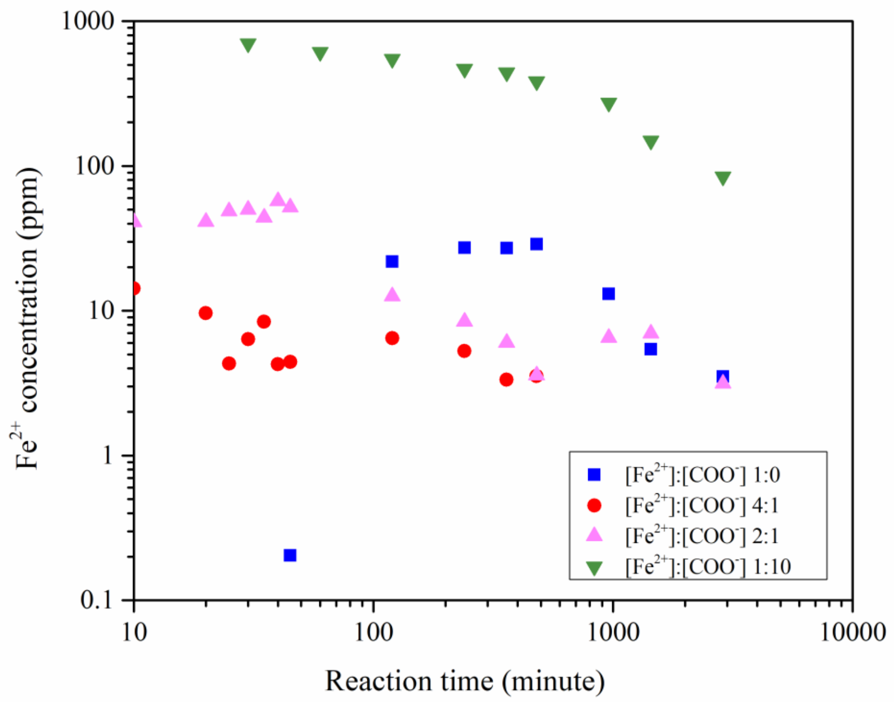

Figure 3.21 Fe^{2+} concentration in the supernatant versus the reaction time.

Once nucleation has occurred, it is highly likely that PAA molecules will interact with LFP particles through electrostatic interactions between the carboxylate moieties and the LFP surfaces and may affect LFP particle interactions. In order to observe the effect of PAA on the surface charge of LFP powders as a function of pH, zeta potential measurements of $[Fe^{2+}]:[COO^-]$ 1:0 and $[Fe^{2+}]:[COO^-]$ 2:1 were conducted (Figure S6). The isoelectric point of LFP without PAA addition was at pH 3.7. In contrast, the isoelectric point of polycrystalline LFP from previous reports by Zhu et al. was at pH 4.8. This is likely due to differences in morphology of LFP particles, where different facets are expressed on the surface[83]. Addition of PAA to the reaction media results in a significant increase in negative charge on the particles as well as a shift in the isoelectric point to lower pH value (i.e., pH = 2.8). These results suggest that PAA is adsorbed on the surface of LFP particles, where COO^- groups are in contact with solution media. As shown in the colloidal chemistry modification of polyethyleneimine (PEI) addition on the surface of LFP particles, the positive charge of particles was measured due to the protonation [153].

This change in isoelectric point as well as the magnitude of the surface charge are likely to effect the solubility of LFP particles as well as how LFP particles interact with each other to form hierarchically arranged (i.e., secondary particles). For example, when no polymer is present (i.e., Fe: COO^- is 1:0, there is a drop in pH over time. Subsequently, we observe single crystalline LFP particles forming with highly faceted surfaces. This is indicative of an Ostwald ripening process [83], where small primary particles with locally high curvature will dissolve (LFP's solubility product is $10^{-24.6}$ [154]) and recrystallize as larger, single crystalline materials. However, as PAA is added, there is a noticeable change in the solution behavior. The pH value does not drop as sharply as more PAA is added. This is primarily due to the fact that the PAA is buffering the solution, absorbing protons (that would lead to a reduction in pH) released from H_3PO_4 and other phosphate species. In addition, the change in isoelectric point and magnitude of zeta potential (towards more negative values) suggests that particles have PAA adsorbed on their surfaces, and subsequently, their interactions will change. The more highly negative charged on the particle surface indicates the acid group (COOH) became ionized and transferred into the COO^- form[155]. This results in the nanoparticles electrostatically repel each other. The degree of ionization of PAA decreased as pH increased or the reaction duration increased, the charge on nanoparticles become less negative. Then, the nanoparticles will come closer an then finally assembly by oriented attachment[156]. The aligned nanoparticles were observed. The bonding of high energy surfaces by crystallographic fusion between primary particles allow the system to win a substantial amount of energy. Therefore, adding PAA adsorbed on particle surfaces results in tuning the surface energies of primary unit and then the nanocrystal morphology [157] as we observed the changed in crystallographic orientation when PAA is added into the reactions. Moreover, PAA get occluded between primary particles, then prevent the crystallographic fusion of the aligned nanoparticles.

Higher concentration of PAA, [Fe^{2+}]:[COO^-] 1:10

In order to better understand the initial precursor state, a similar time study was performed using a [Fe^{2+}]:[COO^-] of 1:10. At 40 min, reactor temperature 135°C, SAED shows weakly nanocrystalline LFP (Figure 3.22).

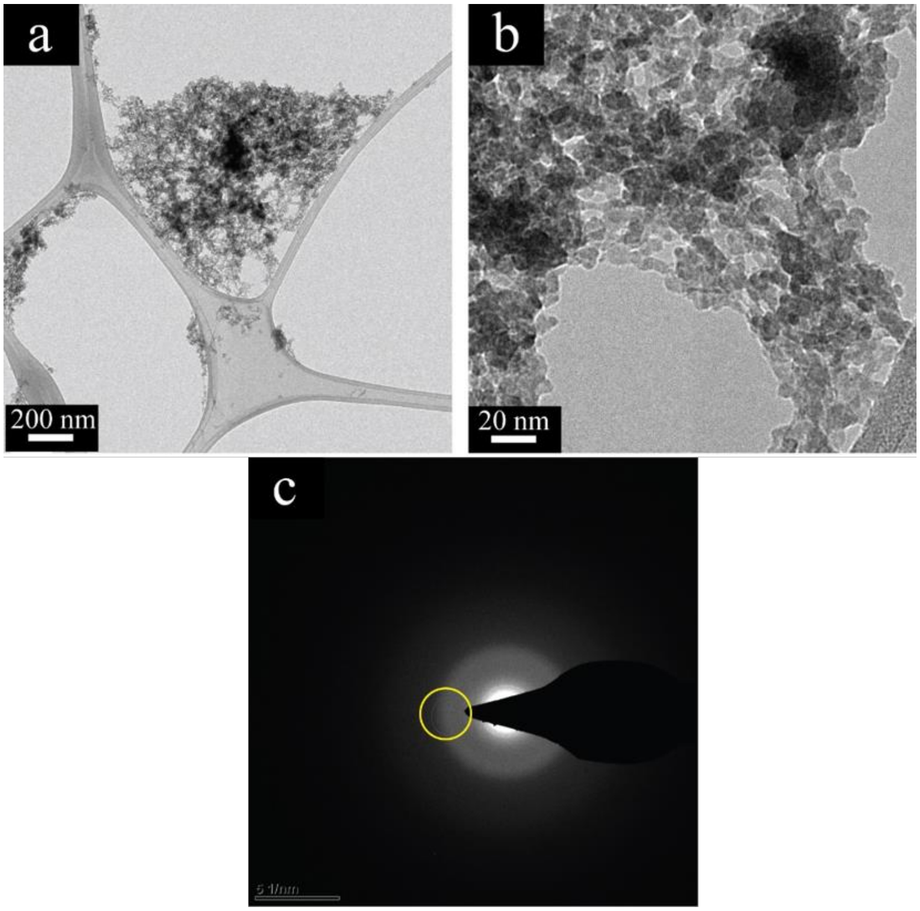

Figure 3.22 [Fe^{2+}]:[COO^{-}] 1:10 synthesized for 40 min, reaction temperature 135°: (a and b) Bright field TEM micrograph and (c) SAED of weakly crystalline nanoparticles

Particles at 60 min reaction time are peanut or rod-shaped and consist of 3-5nm primary particles which have aggregated to form secondary particles (Figure 3.23a and 3.23b). SAED demonstrates the particles are crystallized with texture and align in (020) direction (Figure 2.20c and 3.23 d). This also corresponds to the XRD pattern in Figure S7. Supporting information showing the (020) plane of LFP is dominant.

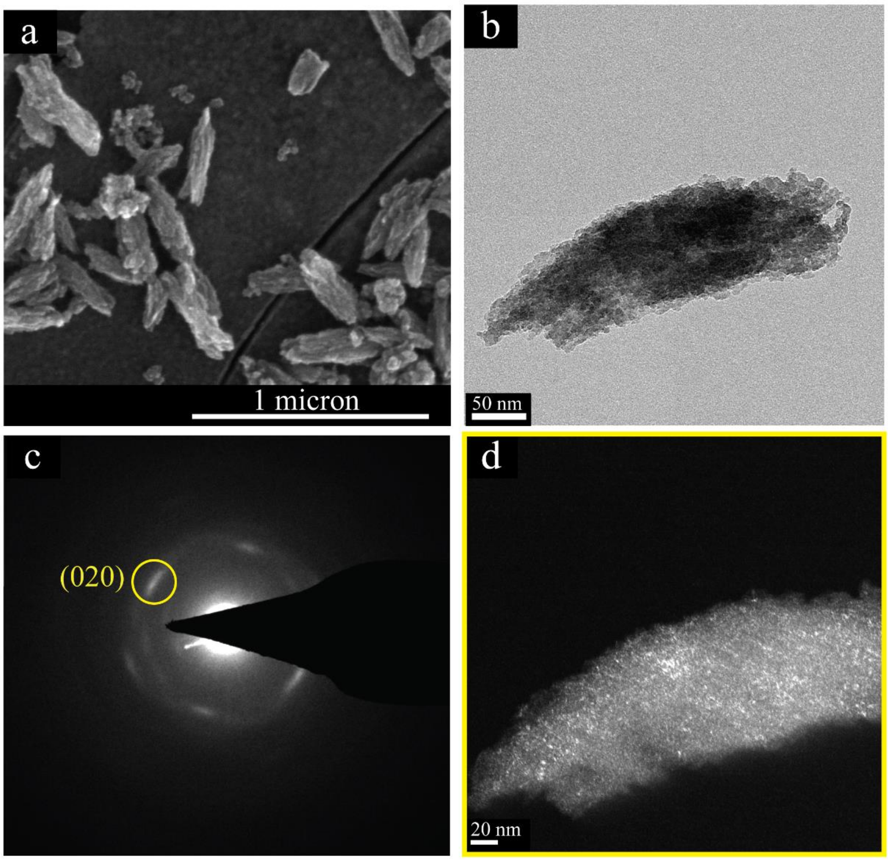

Figure 3.23 [Fe^{2+}]:[COO^{-}] 1:10 synthesized for 60 min: (a) SEM micrograph (b) Bright field TEM micrograph and (b) SAED of crystalline nanoparticles, with (c) dark field TEM micrograph showing several nanocrystals.

High resolution TEM micrographs in Figure 3.24 (a and b) illustrate the rod is formed by fine crystals in size range of 3-5 nm. These nanocrystals were crystallized, as shown by lattice fringes on the (020) (Figure 3.24(c)) and (001) plane (Figure 3.24(d)) with the same orientation relative to fast Fourier transform (FFT).

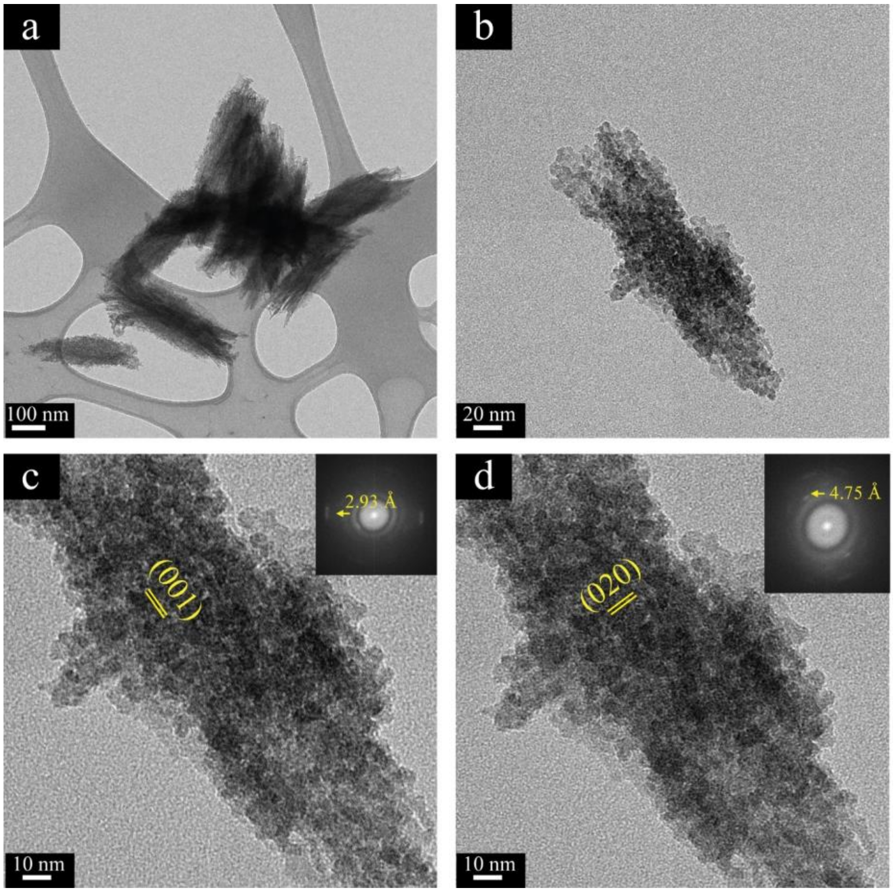

Figure 3.24 TEM micrographs of [Fe^{2+}]:[COO^{-}] 1:10 synthesized for 60 min, reactor temperature 170°C: (a) Bright field TEM micrograph showing rod-like morphology (b) Bright field TEM micrograph of one particle corresponding to (001) plane (c) and (020) plane (d) . The insets show FFT nanorod.

At 90 min, the rod-like particles increase in size to about 500 nm. They consist of crystalline nanoparticles with aligned lattice planes (Figure 3.25). The alignment of nanoparticles was observed using high resolution TEM as shown in Figure 3.25. The tips of these rods are perfectly aligned and have begun branching out on the <300> direction. This state most likely occurs at low levels of supersaturation similar to previous observations made in a $CaCO_3$ system [158].

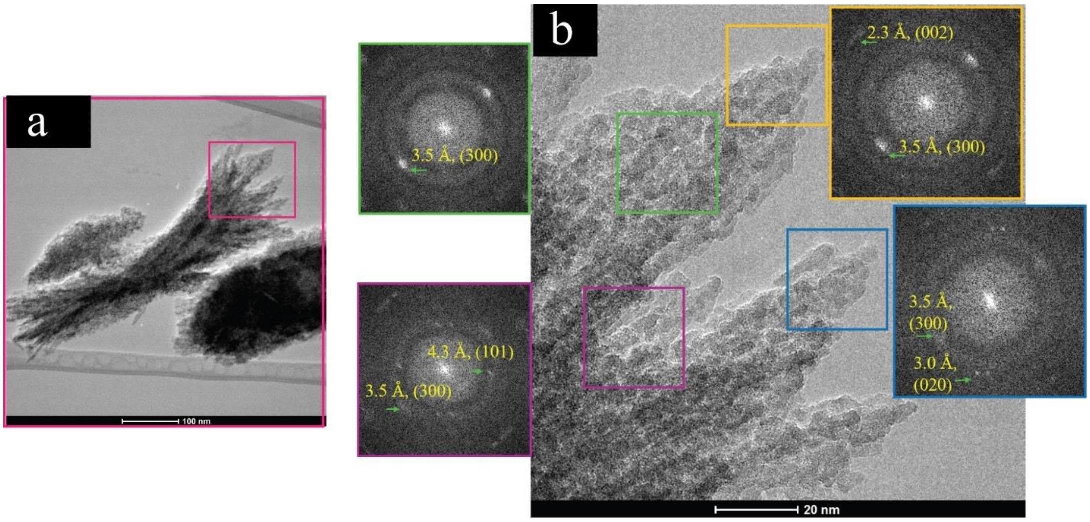

Figure 3.25 Crystallization time-study of LFP [Fe^{2+}]:[COO^{-}] 1:10 synthesized for 90 min, reactor temperature 190°C: (a) Bright field TEM micrograph and (b) SAED of crystalline nanoparticles, with (c) dark field TEM micrograph showing several nanocrystals.

STEM in Figure 3.26 a and b alignment of nanoparticles forming rods. TEM energy-dispersive X-ray spectroscopy elemental maps of particles synthesized from [Fe^{2+}]:[COO^{-}] 1:10 for 90 min show the distribution of Oxygen (Figure 3.26c), Phosphorus (Figure 3.26d), Iron (Figure 3.26e), and Carbon with Fe (Figure 3.26f),. We can see that carbon is mostly distributed on the edges of crystals. However, Na is also present as shown in the EDS spectrum in Figure S8.

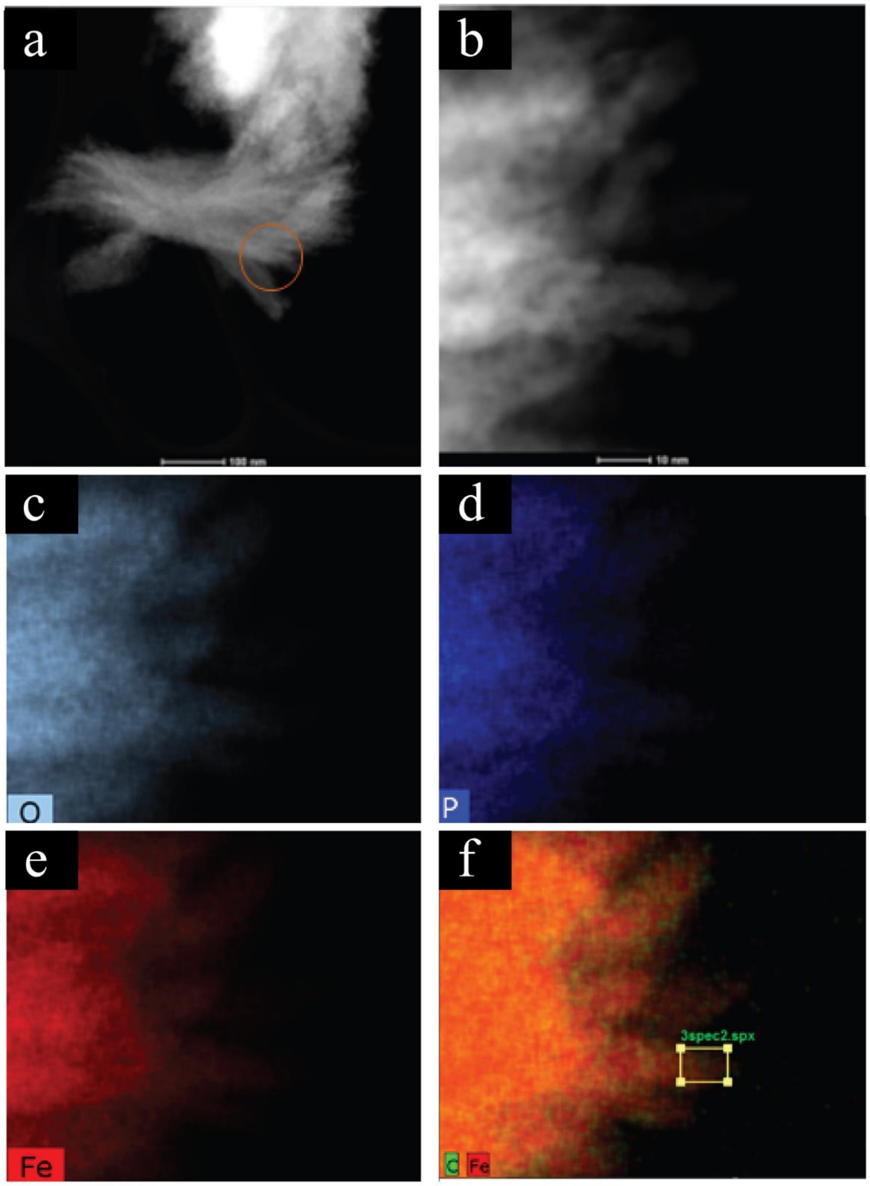

Figure 3.26 EDS mapping of LFP $[Fe^{2+}]:[COO^{-}]$ 1:10 synthesized for 90 min, reactor temperature 190°C: (a) High resolution STEM micrographs (b)-(f) EDS elemental mapping images

At 150 min, the growth of aggregates was still rod like-structure (Figure 3.27a). SAED in Figure 3.27b reveals polycrystalline structure with confirm by dark field (Figure 3.27c)

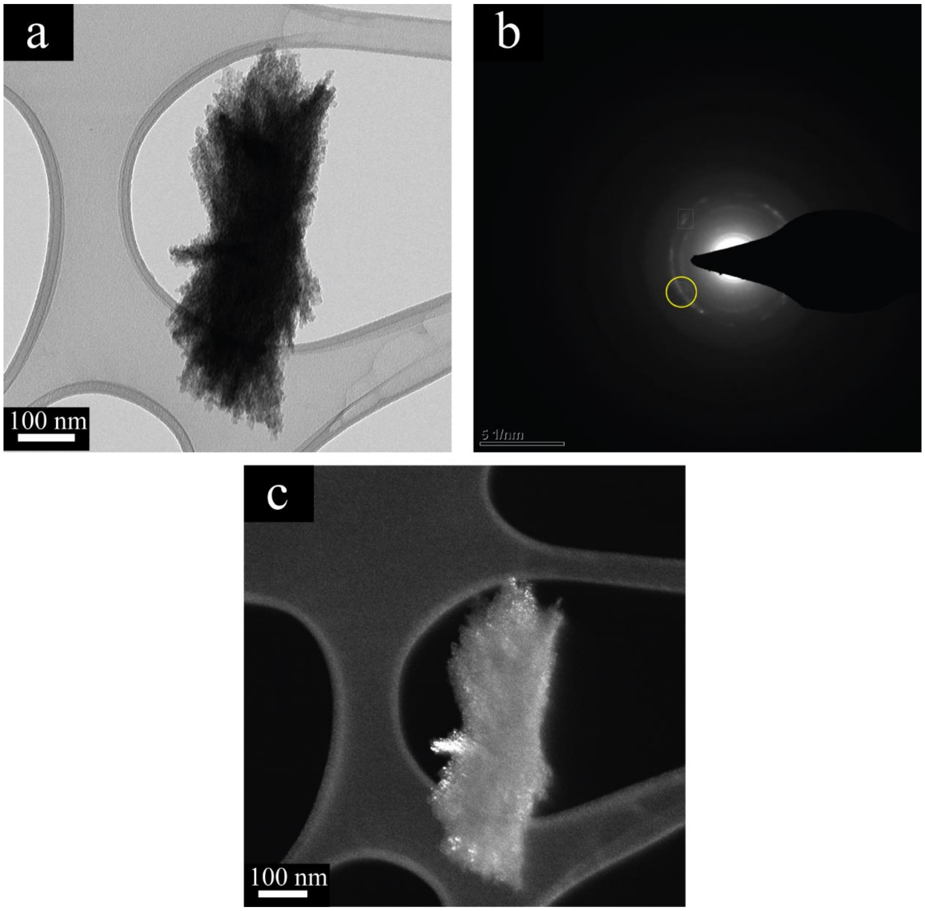

Figure 3.27 LFP $[Fe^{2+}]$:$[COO^{-}]$ 1:10 synthesized for 150 min, reactor temperature 200ºC: (a) Bright field TEM micrograph and (b) SAED of crystalline nanoparticles, with (c) dark field TEM micrograph showing several nanocrystals.

Bright firld TEM micrograph of particles at 150 min (Figure 2.28a) shows rod like particles. High resolution TEM micrographs show the nanorods at the tip of particles were aligned in the same direction (Figure 3.28b). High magnification micrographs in Figure 3.28c and 3.28d reveal that the growth direction of theses rods was <300> as correspond to FFT in Figure 3.28d and 3.28f.

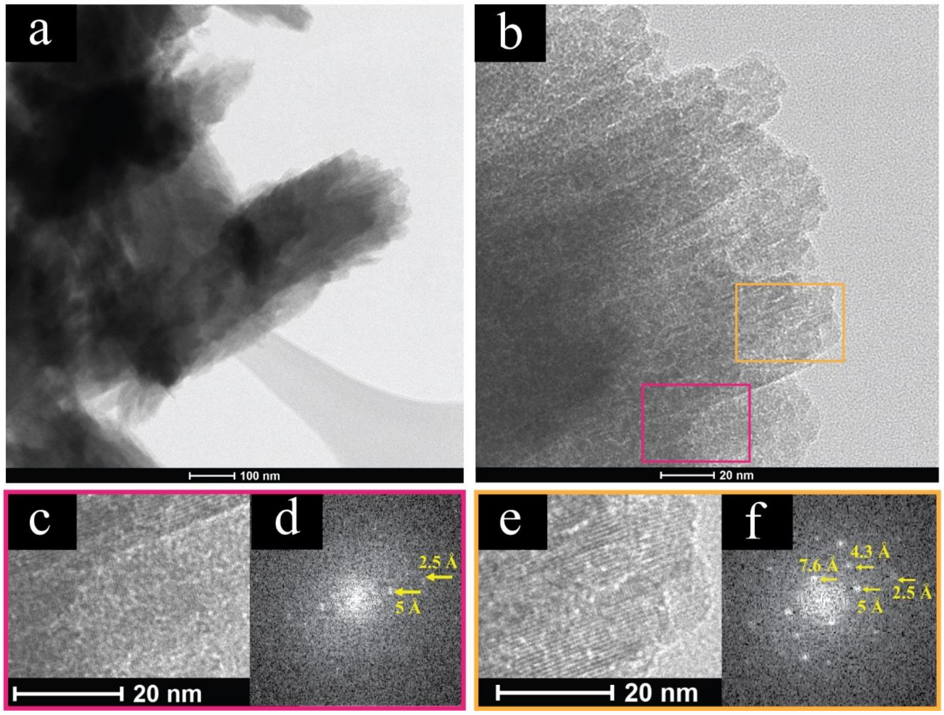

Figure 3.28 Crystallization time-study of LFP [Fe^{2+}]:[COO^-] 1:10 synthesized reactor temperature 200°C: (a) and (b) Bright field TEM micrographs. (c) and (e) TEM micrographs showing several nanocrystals at 150 min. (c-f) SAED of crystalline particles from c and e.

Increased concentration of PAA to [Fe^{2+}]:[COO^{-}] 1:10 shows the morphology of nanorods is consistent with oriented attachment of nanoparticles.

Based on the results, PAA play an important role to control LFP formation mechanism. A probable crystallization mechanism of morphological evaluation of LFP crystals in the presence of low concentration of PAA ([Fe^{2+}]:[COO^{-}] 1:10) behaves similarly to other systems which crystallized by particle attachment, especially biomineralization[120, 159-162]. The small primary particles were attached to neighboring particles, eliminating two high energy surfaces by crystallographic fusion. Then, mesocrystals are observed with common crystallographic orientation as we observed in the polycrystalline LFP [83], confirming an oriented attachment of nanoparticles to form ellipsoidal-like structures. Therefore, the suggested crystallization pathway is as follows: nanocrystalline VVT nanoparticles form, aggregate into larger, metastable particles, which then dissolve; amorphous and nanocrystalline LFP nucleates from the ions released by the VVT; these LFP crystals grow until they form bulk crystals through a nearly orientated attachment mechanism [**114-115**]..

Crystallization of LFP in the presence of high concentration of PAA such as [Fe^{2+}]:[COO^{-}] 2:1, amorphous or poorly crystalline nanoparticles (1-3 nm) were formed first. This is based on the dark field TEM and SAED results which showed small VVT nanocrystals at early reaction stages. Next, poorly crystalline VVT plates formed as a metastable phase and coexisted with weakly crystalline LFP nanoparticles. However, the synthesized LFP particles with [Fe^{2+}]:[COO^{-}] 1:1 and higher concentration of PAA, poorly crystalline nanoparticles were found without VVT formation. Then these nanoparticles formed thread-like fibers at early stage of spherulite growth, especially in polymeric systems[145, 148, 163]. These fibers continued to grow by branching out and forming two-fold symmetry which misorientation angle. Finally, the array pattern of spherulite crystals were formed as a supersaturation increased with reaction temperature[144-145].

Growth mechanism at long reaction time

SEM micrographs in Figure 3.29 for longer duration reactions of LFP [Fe^{2+}]:[COO^-] 4:1 synthesized at 200°C, reveal the size of secondary particles and number of grain boundaries decreased but the primary particle size increases. For example, the secondary particles were approximately 300-500 nm at 150 min reaction time and consist of 40-70 nm primary crystals. After 2910 min, the secondary particles shrank to 200-500 nm, while the primary particles grew to 120-500 nm. This indicates Ostwald ripening of these polycrystalline LFP particles due to the decreasing of pH in the solution which increasing reaction times. This increases the solubility of LFP in the solution, enabling dissolution-recrystallization of these particles.

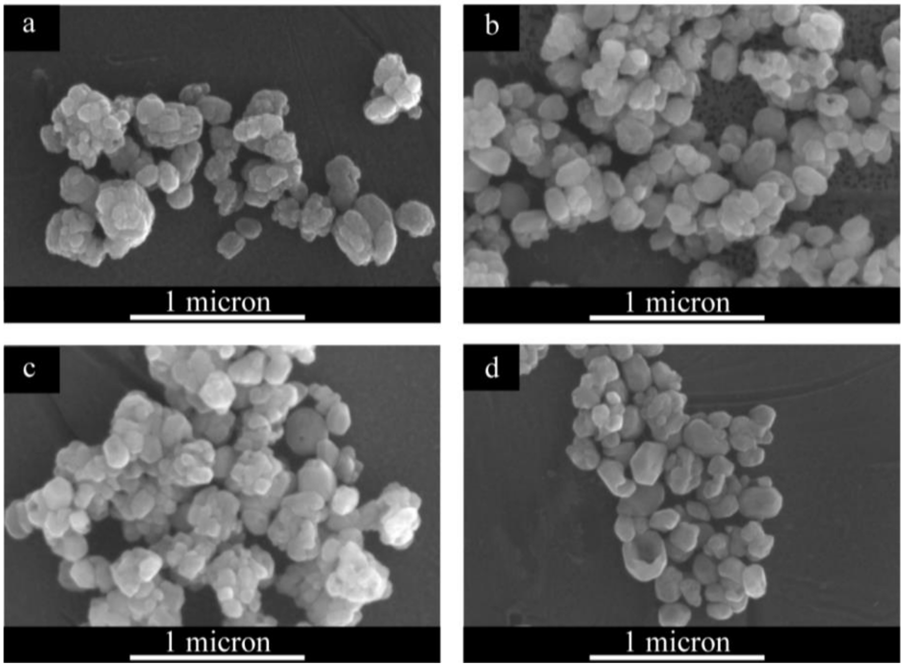

Figure 3.29 SEM micrographs of LFP [Fe^{2+}]:[COO^{-}] 4:1 synthesized at 200°C: (a) 150 min (b) 510 min (c) 1470 min (24.5 h) (e) 2910 min (48.5h)

Table 3.2 shows the specific surface area increases with the amount of PAA measured using BET porosimetry. This is due to an increase in the smaller primary particles. However, a thick layer of polymer on the surface of particles and between grains inside the particles with very high concentration of PAA as [Fe^{2+}]:[COO^{-}] 1:2, can be observed as from TGA (Figure S4) and Raman showing disordered carbon (Figure S9). [164] [165] This leads to an decrease in the surface area.

After etching with 0.01 M HCl for 1 h, the surface areas of theses samples increased. For example, the surface area of [Fe^{2+}]:[COO^{-}] 1:2 was increased from 7.6 to 88.11 m^2g^{-1} since the polymer was etched away, increasing the porosity inside the particles and exposing the surface of crystals as shown in Figure 3.30.

Table 3.2 BET analysis of LFP samples synthesized with [Fe^{2+}]:[COO^{-}] 1:0, 4:1, 2:1, and 1:2 at 200°C for 150 minutes

	BET surface area before etching (m^2/g)	BET surface area after etching (m^2/g)
[Fe^{2+}]:[COO^{-}] 1:0	10.7763	-
[Fe^{2+}]:[COO^{-}] 4:1	15.0986	-
[Fe^{2+}]:[COO^{-}] 2:1	16.4658	37.4832
[Fe^{2+}]:[COO^{-}] 1:2	7.6456	88.1150

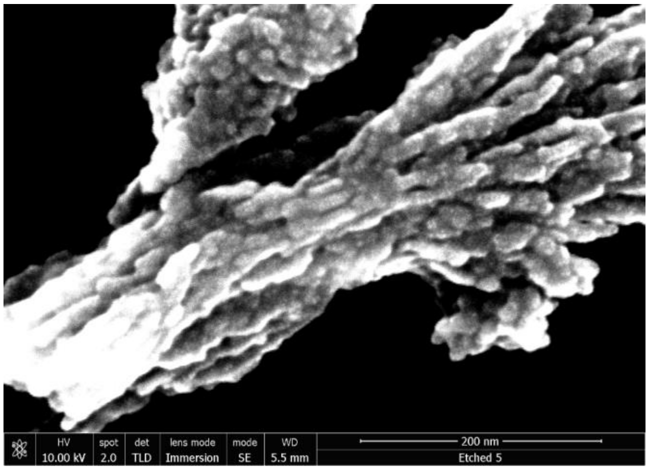

Figure 3.30 Etched [Fe^{2+}]:[COO^{-}] 1:10 synthesized for 90 min using 0.01 M HCl for 1 h

In order to understand the nanostructure and orientation of subunits in the interior of the particles, fractured samples were prepared by grinding synthesized powders under with liquid nitrogen. Figure 3.31 shows fractured samples of LFP incorporated with PAA. Particles prepared from [Fe^{2+}]:[COO^{-}] 4:1 and 2:1 have larger subunits than [Fe^{2+}]:[COO^{-}] 1:1, 1:2, and 1:10 as mentioned above. However, most secondary particles are composed of small primary particles as building units. The polymer serves as an adhesive mortar between these inorganic nanobricks.

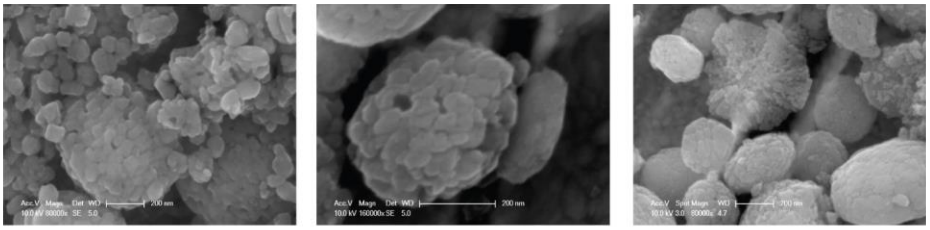

$[Fe^{2+}]$:[OH] 4:1, 2.5 h

$[Fe^{2+}]$:[OH] 2:1, 2.5 h

$[Fe^{2+}]$:[OH] 1:1, 2.5 h

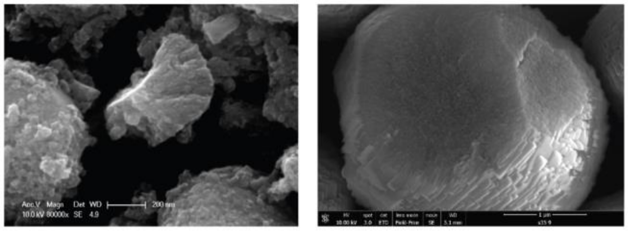

$[Fe^{2+}]$:[OH] 1:2, 2.5 h

$[Fe^{2+}]$:[OH] 1:10, 24.5h

Figure 3.31 SEM micrographs of fractured LFP $[Fe^{2+}]$:$[COO^-]$ synthesized 2.5 h

3.4. Electrochemical performance

The CV curves in Figure 3.32 demonstrate that the PAA-mediated sample displays a voltage hysteresis of 0.2 V with a peak current of 0.125 A/g while the sample without PAA shows a voltage hysteresis 0.6 V and a peak current at 0.04 A/g. These results imply that the $[Fe^{2+}]$:$[COO^-]$ 2:1 sample has better kinetic performance compared to $[Fe^{2+}]$:$[COO^-]$ 1:0 sample during lithiation and delithiation process due to the smaller LFP particle size and increased porosity, which increases the active surface area and causes faster ion and electron transport.

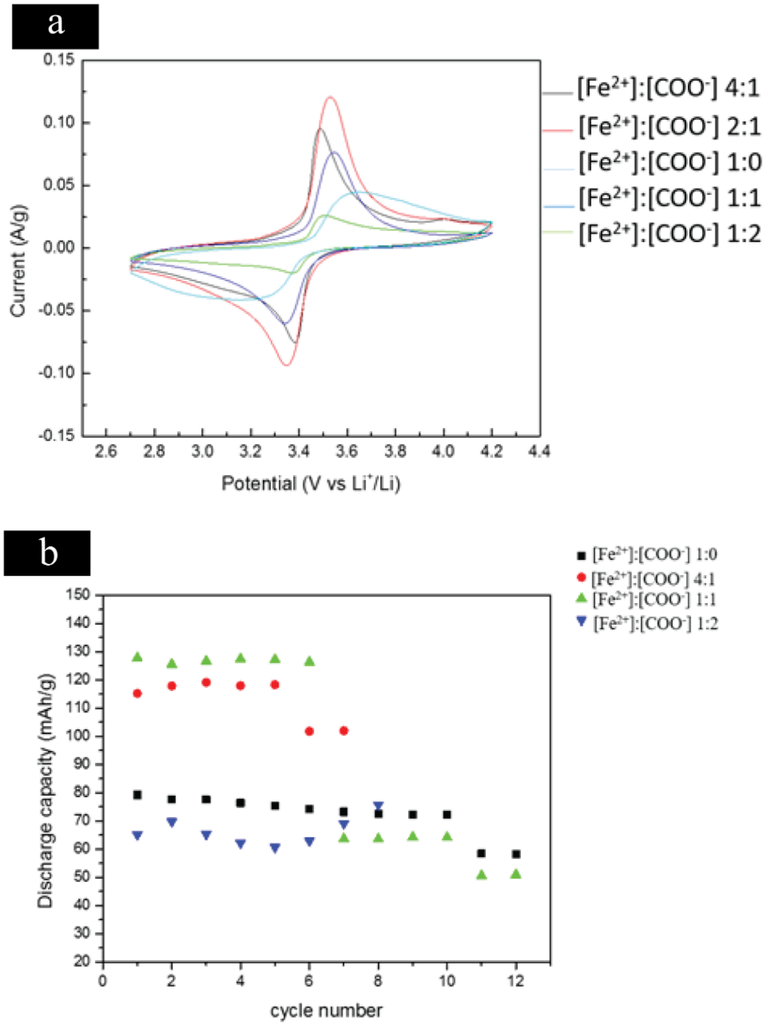

Figure 3.32 (a) CV profiles of the LFP products synthesized from $[Fe^{2+}]$:$[COO^{-}]$ 1:0, 4:1, 2:1, 1:1, and 1:1 at 200°C for 150 min. (b) Discharge capacity for $[Fe^{2+}]$:$[COO^{-}]$ 1:0, 4:1, 1:1, and 1:2 at 200°C for 150 min.

3.5. Conclusions

We investigated crystal nucleation and morphology of $LiFePO_4$ synthesized in the presence of various concentrations of PAA. The addition of PAA in the precursor suspension delays crystal formation due to the chelation of COO^- and the Fe^{2+} ion, which inhibits LFP precipitation. At higher PAA concentrations, more PAA adsorbs on the surface of LFP nanoparticles, leading to a diffusion controlled morphology. Through PAA mediated synthesis, polycrystalline LFP was obtained which provided better electrochemical performance due to smaller primary crystals and more active sites for Li ions compared to single crystal of LFP synthesized without PAA additive.

Acknowledgements

We would like to acknowledge funding from Winston Chung Global Energy. We thank Professor Juchen Guo and Professor Haizhou Liu for using of his facilities. We also acknowledge the support from Professor Krassimir Bozhilov and Mathias Rommelfanger for use of The Central Facility for Advanced Microscopy and Microanalysis facilities.

Supporting Information

Bio-inspired crystallization of Li-ion cathodes

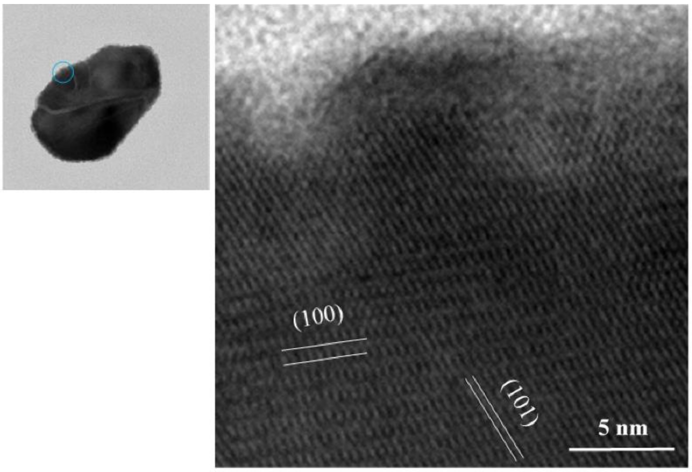

Figure S1. HRTEM micrograph of particle synthesized from [Fe^{2+}]:[COO^-] 1:0 at 200°C for 2h.

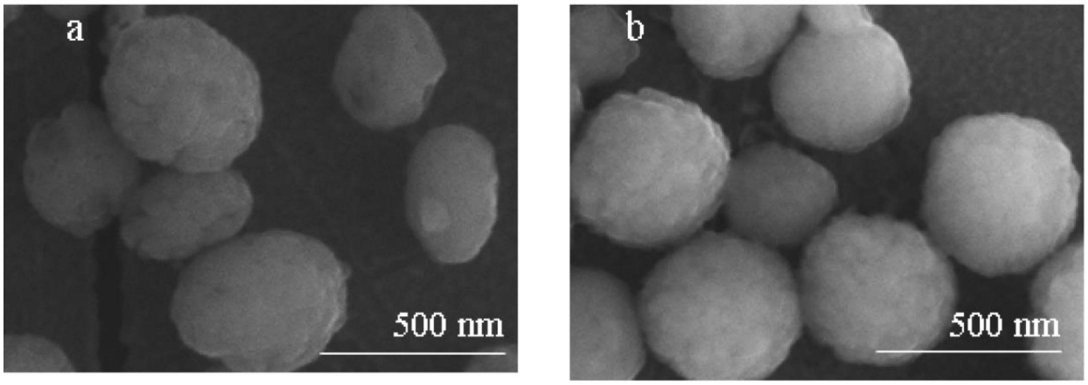

Figure S2. SEM micrographs of LFP particles (a) synthesized from [Fe^{2+}]:[COO^-] 2:1 at 200°C for 2h, (b) synthesized from [Fe^{2+}]:[COO^-] 1:1 at 200°C for 2h.

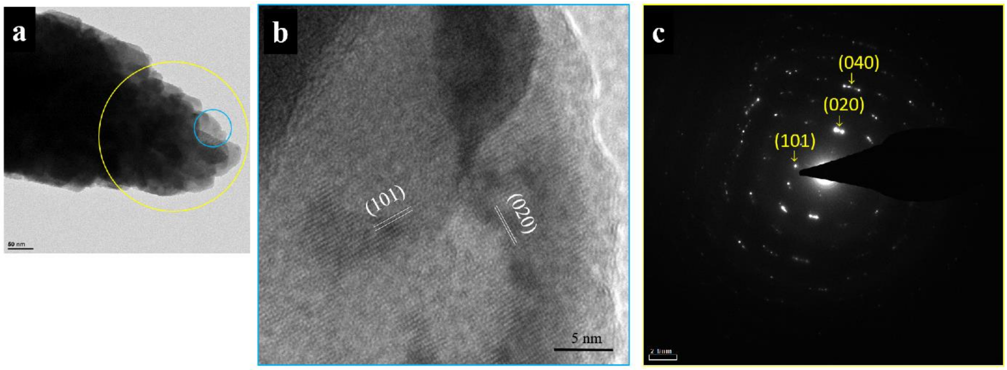

Figure S3. Characterization of particle synthesized from $[Fe^{2+}]:[COO^{-}]$ 10:1 at 200°C for 2h. (a) Bright field TEM micrograph, (b) HRTEM from circled blue area and, (c) SAED from yellow circled area.

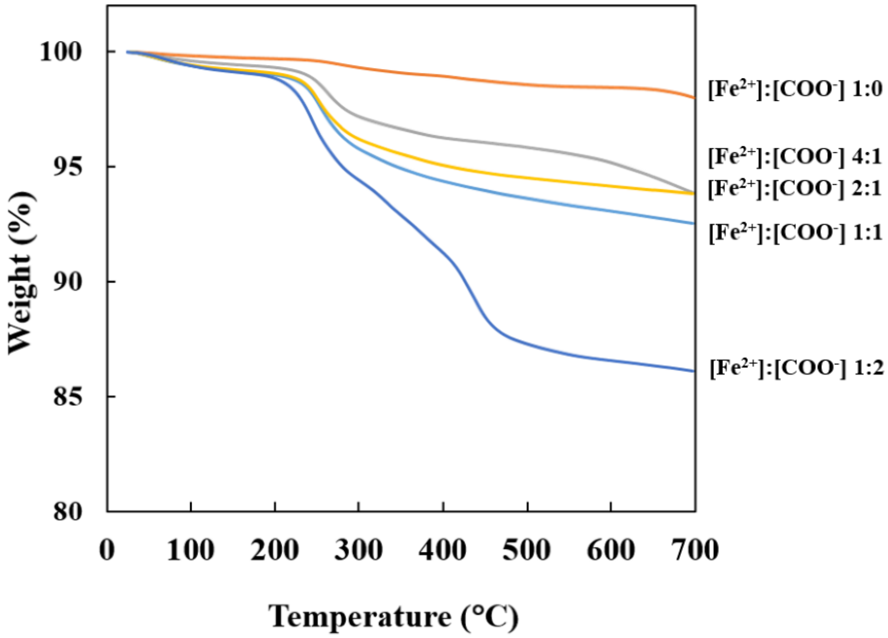

Figure S4. TGA results of $LiFePO_4$ samples synthesized with $[Fe^{2+}]:[COO^{-}]$ 1:0, $[Fe^{2+}]:[COO^{-}]$ 4:1, $[Fe^{2+}]:[COO^{-}]$ 2:1, $[Fe^{2+}]:[COO^{-}]$ 1:1 and $[Fe^{2+}]:[COO^{-}]$ 1:2 at 200°C for 150 minutes in $N_2/5\%H_2$ atmosphere from room temperature to 700°C.

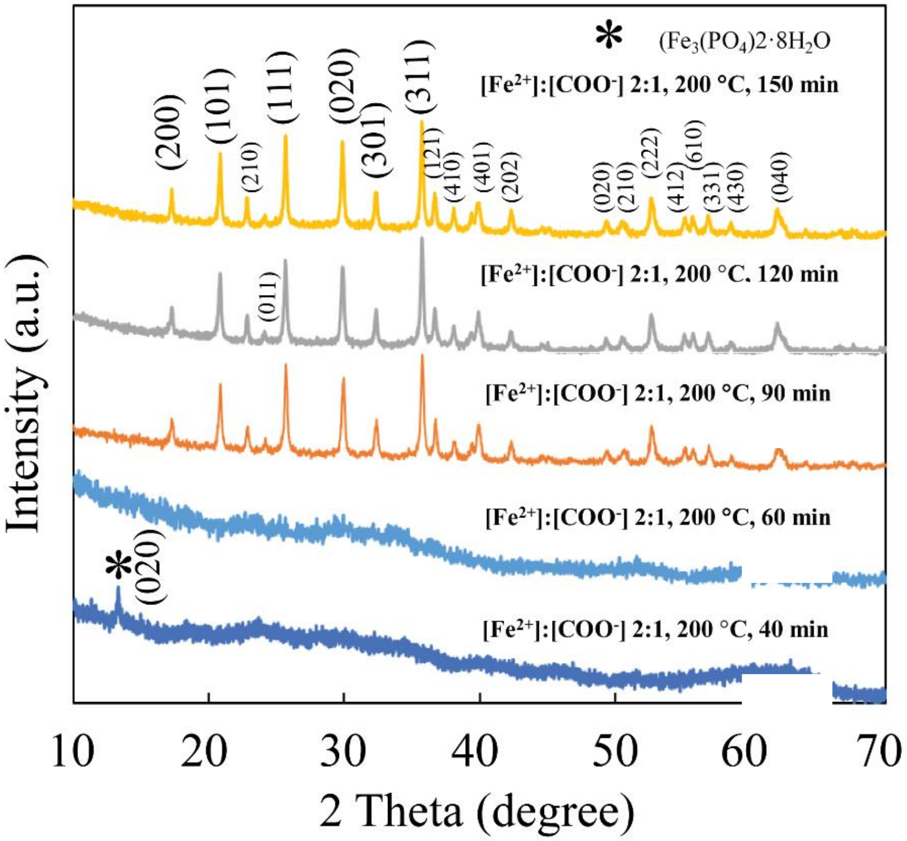

Figure S5. XRD patterns of products after heating for 60 min, 90 min, 120 min, and 150 min. The index is LFP. The crystals were obtained after 90 min reaction time.

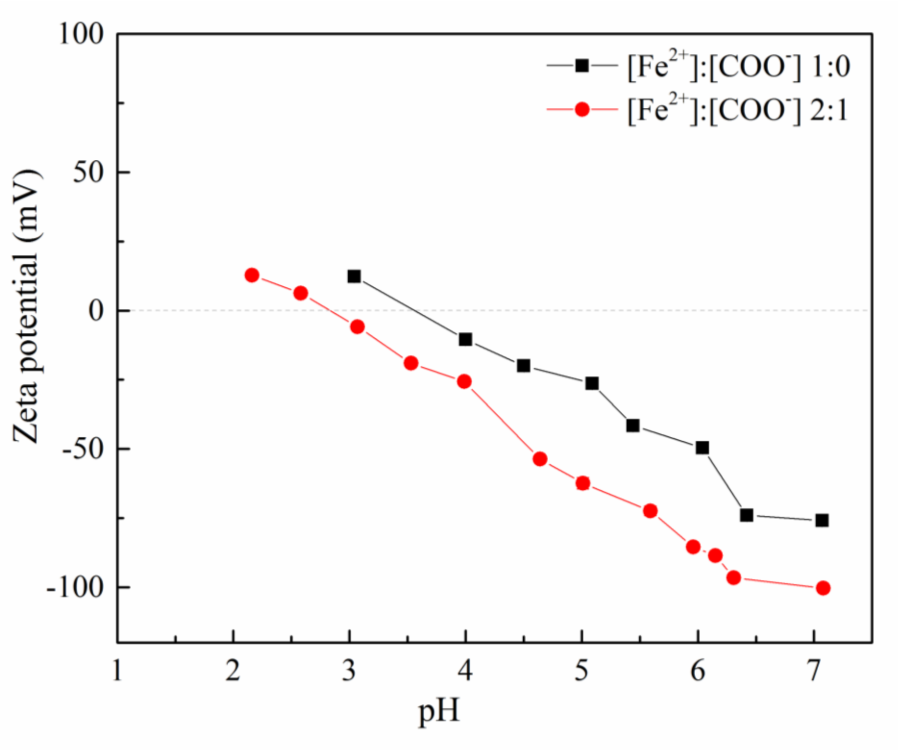

Figure S6. Zeta potential of [Fe^{2+}]:[COO^-] 1:0 and [Fe^{2+}]:[COO^-] 2:1.

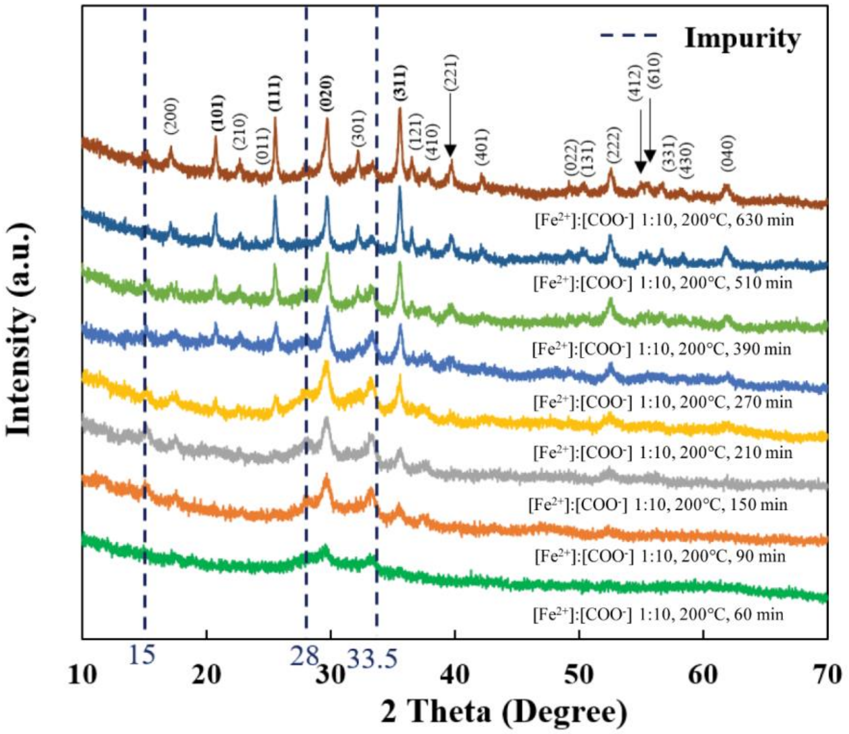

Figure S7. XRD patterns of [Fe^{2+}]:[COO^{-}] 1:10 at different reaction times from 60 min to 630 min.

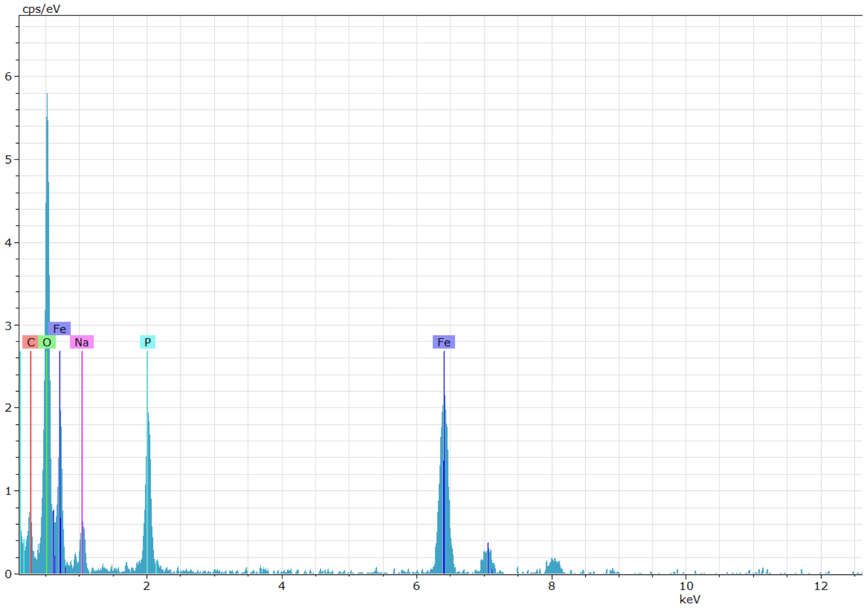

Figure S8. EDS spectrum of [Fe^{2+}]:[COO^{-}] 1:10 at 90 min reaction time showing Na peak as impurity.

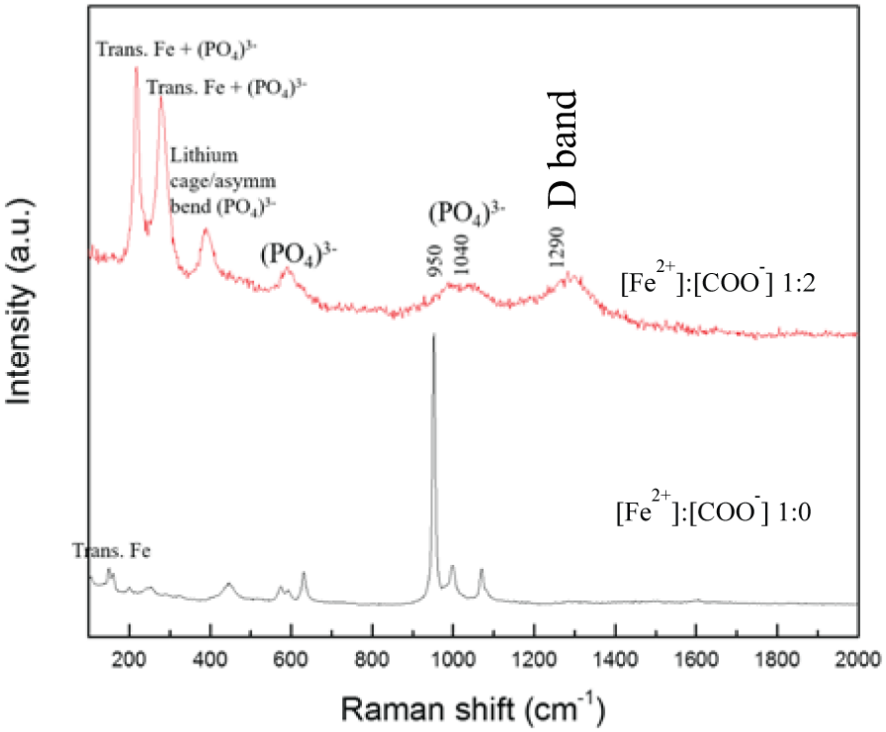

Figure S9. Raman spectra of $[Fe^{2+}]$:$[COO^-]$ 1:0 and 1:2, synthesized at 200°C for 150 minutes. The spectrum $[Fe^{2+}]$:$[COO^-]$ 1:2 shows the broad peak at 1290 cm^{-1} corresponding to amorphous carbon from PAA. The intermolecular stretching modes of the $(PO_4)^{3-}$ anion are much weaker compared to $[Fe^{2+}]$:$[COO^-]$ 1:0, suggesting that the carbon might coat on the surface of LFP particles and screen the LFP from the detection. Moreover, the broad peaks from $[Fe^{2+}]$:$[COO^-]$ 1:2 confirm less crystallinity compared to $[Fe^{2+}]$:$[COO^-]$ 1:0 [166].

Table S1. Crystallite size of LFP samples synthesized with $[Fe^{2+}]$:$[COO^-]$ 1:0, 4:1, 2:1, 1:1, and 1:2 at 200°C for different reaction times.

	Crystallite size (nm)			
	60 min	**90 min**	**120 min**	**150 min**
$[Fe^{2+}]$:$[COO^-]$ 1:0	56	62	69	69
$[Fe^{2+}]$:$[COO^-]$ 4:1	33	34	45	49
$[Fe^{2+}]$:$[COO^-]$ 2:1	Amorphous	31	34	42
$[Fe^{2+}]$:$[COO^-]$ 1:1	Amorphous	16	32	32
$[Fe^{2+}]$:$[COO^-]$ 1:2	Amorphous	17	32	32

Table S2. Compositions of precursor solutions for solvothermal synthesis.

Sample No.	H_2O (ml)	$LiOH \cdot H_2O$ (mg)	H_3PO_4 (µl)	$FeSO_4 \cdot 7H_2O$ (mg)	TEG (ml)	PAA (mg)	$[COO^-]/[Fe^{2+}]$
1	5	125.9	68	278	5	-	-
2	5	125.9	68	278	5	7.2	10:1
3	5	125.9	68	278	5	18	4:1
4	5	125.9	68	278	5	36	2:1
5	5	125.9	68	278	5	72	1:1
6	5	125.9	68	278	5	144	1:2
7	5	125.9	68	278	5	720	1:10

Chapter 4

LFP/C composite

LFP/C composite

Abstract

We synthesized porous $LiFePO_4$/C composite by the solvothermal method and subsequent annealing at 400 °C and 600 °C under 95% N_2/5% H_2. Based on inspiration from nature, polyvinyl alcohol (PVA) was added into the reactors during the solvothermal process as an organic scaffold. In the absence of polymer, plate-like LFP particles were obtained. However, with the addition of the polymer, the polycrystalline particles and small primary particles were observed. Thus, PVA limits the diffusion of LFP within the PVA matrix. Annealed LFP/C composites at 600 °C reveals the ultrathin carbon coating on polycrystalline LFP/C composite with a low ratio of disorder to graphite (I_D/I_G) as 0.55.

4.1. Introduction

Lithium iron phosphate (LFP) is used as a cathode material for batteries with application in electric vehicles (EVs), hybrid electric vehicles (HEVs), and energy storage devices, primarily because of its high-energy density, relatively high chemical and thermal stability, and environmentally friendly processing techniques[18, 38, 167-168]. However, it has been found to have low intrinsic electronic conductivity (10^{-9} to 10^{-10} Scm^{-1}) and Li-ion diffusivity (1.8×10^{-14} cm^2S^{-1}),[169] limiting its utility for certain industrial applications. Research has been carried out to overcome this by synthesizing nanoscale LFP particles,[170-171] introducing conductive materials such as carbon and conductive polymers,[51, 172] and doping LFP with cations.[80, 173-174] Another important factor that is directly related to the battery capacity is the Li intercalation/de-intercalation capability of the electrodes.[167] Porous LFP-carbon (LFP/C) composite materials can enhance lithium intercalation during cycling due to the change in the interfaces between carbon and the surface of the Li-nanoparticles and can provide access to the electrolyte ions through the pores.[175] Doherty et al., reported that the capacity of porous LFP/C composites was increased to 160 $mAhg^{-1}$ at 0.1C discharge rate compared to the theoretical capacity of LFP (170 $mAhg^{-1}$).[176] Amongst different methods applied to increase the power capacity of LFP, a three-dimensional porous LFP/C architecture is the most significant approach to improve electrical conductivity and Li-ion diffusion.[177-179] Yu et al. determined that 3D-porous nanostructured LFP/C composites with a crystallite size of 54 nm, a pore diameter of 24.3 nm, and 3.2 wt% carbon coating can significantly increase the Li-ion diffusion rate, resulting in a higher Li-ion diffusivity of 7.40×10^{-12} cm^2S^{-1}. [180] Moreover, increasing the surface area of LFP particles results in a larger fraction of carbon coated on the particles and a decrease in tap density. Chen et al. demonstrated that the presence of less than 1% carbon in the sample could reduce tap density, thus increasing the volumetric energy density. For example, volumetric energy density decreases by 22% from 2.1 to 1.6 Wh/cm^3 when the amount of carbon in the LFP/C composite is increased to 15 wt%. Carbon coating with higher sp^2 bonded carbon provides better electrochemical properties when compared to sp^3-like disordered carbon.[181,182-183] Therefore, producing LFP/C composites with a porous structure, homogeneously coated carbon on the LFP surface, and a high ratio of sp^2/sp^3 carbon is critical to improving the electrochemical performance of batteries.

Nature provides a variety of biomineralized systems with controlled nanostructures to achieve specific functions.[184] These biominerals are usually formed in the presence of organics such as proteins and polysaccharides. These organics have different functional groups which control the nucleation and crystal growth, as found in nacre, sea urchins, and bones.[185] The crystallization process may be through heteroepitaxial growth on organic molecules, attachment of particles, or self-assembly and are controlled kinetically, resulting in precise crystallite morphologies.[186-188] Here, based on inspiration from these natural processes, we used polyvinyl alcohol (PVA), an organic matrix that can form a hydrogel under the solvothermal condition to control the crystal size, particle size, and shape of LFP nanoparticles. Annealing the resulting PVA-LFP produces a three-dimensional LFP/C composite with high surface area, small crystallite size, and a layer of carbon coating the surface of LFP particles that improve electrochemical performance kinetics.

4.2. Experimental procedure

Preparation of materials

$LiFePO_4$/C composites were synthesized under solvothermal conditions by adding polyvinyl alcohol (PVA, M_w 31,000-50,000, 99% hydrolyzed) to the reaction. First, $LiOH.H_2O$, $FeSO_4.7H_2O$, and 85 wt% H_3PO_4 were used in a molar ratio 3:1:1 to form a precursor suspension. The suspension was stirred at room temperature for 10 minutes under an argon atmosphere and then transferred to a Teflon-lined autoclave. Polyvinyl alcohol powders were then added into the precursor suspension. The ratios of [Fe^{2+}]:[OH] were 1:0, 1:10, 1:60 and 1:100. The autoclaves were sealed and heated at 160°C for 150 min. After that, the autoclaves were cooled down to room temperature and the resulting products were washed with deionized water and 70% ethanol, and subsequently dried in a vacuum oven. The synthesized samples were placed in an alumina boat and annealed at various temperatures from 400 to 600°C for 1 hour (ramp rate 5°C/min) in 95%N_2/5%H_2 or air at a flow rate of 100 CC/min.

Material Characterization

The crystallite size and phase of the powder products were determined by X-Ray powder diffraction (XRD, Panalytical) using Cu Kα radiation. The Scherrer method was used to calculate the crystallite size based on the measurement of the full-width at half maximum (FWHM) of the relevant diffraction peaks. Particle sizes and morphologies were observed using secondary electron (SE) imaging with a scanning electron microscope (SEM, FEI NNS450 and TESCAN MIRA3 GMU) at 10 keV accelerating voltage at a working distance of 5 mm. A transmission electron microscope (TEM, FEI Tecnai 12), operated at 120 keV, was used to identify crystallite size, morphology, and phase. Adobe Photoshop® was used to measure particle sizes. Thermal degradation analysis was performed using a Thermogravimetric Analyzer (TGA, TA Instrument Q600) with a temperature range from 25 – 700°C in a 95%N_2/5%H_2 or air atmosphere. Fourier Transform Infrared spectroscopy (FTIR, Nicolet 6700) was used to identify any residual polymer while Raman spectroscopy (Horiba LabRam) was used to identify graphitic carbon in the annealed materials.

4.3. Results and Discussion

4.3.1 Effect of PVA concentration on structure of LFP/C composite

The concentration of PVA was optimized during the solvothermal process to obtain an LFP/C porous composite structure. Scanning electron micrographs, in Figure 1, reveal the structural morphologies of LFP/C composites, synthesized using different PVA concentrations. LFP, without any PVA, yields particles with plate-like morphologies averaging 0.5-1.5 micrometers in length, as shown in Figure 4.1(a). Following addition of PVA, the samples are observed to contain heterogeneities, likely due to nonhomogeneous of LFP particles in a PVA matrix (Figure 4.1 (b-d)). LFP/C composites were washed with dimethyl sulfoxide (DMSO) to etch away the polymer and reveal the underlying LFP crystallites and imaged using SEM. Samples with [Fe^{2+}]:[OH] 1:10 ratio displayed faceted plate-like LFP particles, with dimensions averaging from 100 nm - 1 μm, as shown in Figure 4.1 (e). Increasing the PVA concentrations to [Fe^{2+}]:[OH] 1:60 and [Fe^{2+}]:[OH] 1:100, polycrystalline particles were observed (Figure 4.1 (f and g)).

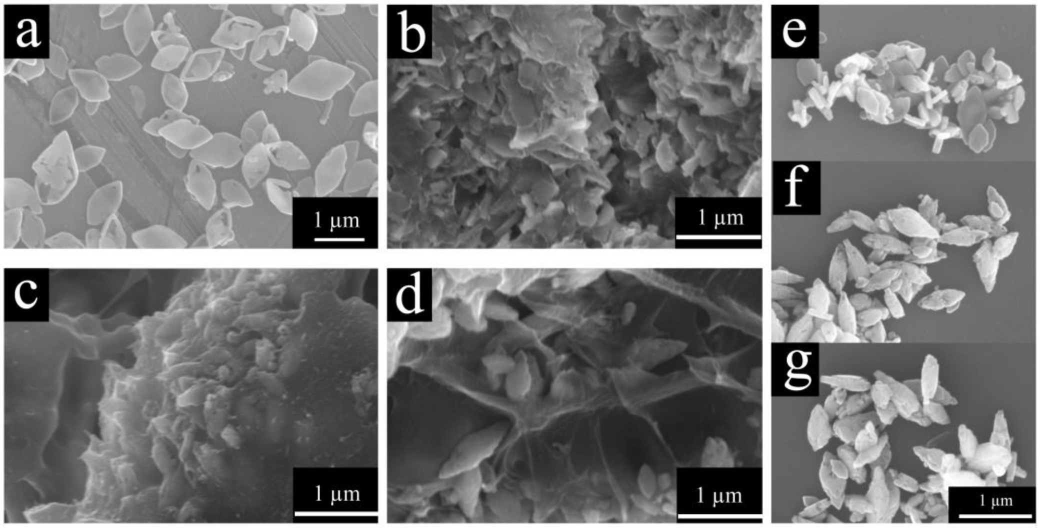

Figure 4.1 SE micrographs of fractured sections of LFP/C composites after solvothermal at 160°C for 150 min (a) [Fe^{2+}]:[OH] 1:0, (b) [Fe^{2+}]:[OH] 1:10, (c) [Fe^{2+}]:[OH] 1:60, (d) [Fe^{2+}]:[OH] 1:100. SE micrographs of washed LFP/C composites using DMSO after solvothermal at 160°C for 150 min (e) [Fe^{2+}]:[OH] 1:10, (f) [Fe^{2+}]:[OH] 1:60, and (g) [Fe^{2+}]:[OH] 1:100.

The XRD patterns of the LFP/C composites after solvothermal synthesis with different PVA concentrations are shown in Figure 4.2. The LFP was indexed to an orthorhombic olivine structure (JCPDS No. 81-1173). The broad peak at 20° 2Θ represents crystalline domains within the PVA (JCPDS No. 61-1401). With increasing amounts of PVA, FWHM increases while the peak intensity decreases; this effect indicates the smaller crystalline regions of polymer. We used the Scherrer equation [189] to determine that the crystallite size of LFP decreased from 45±3 nm ([Fe^{2+}]:[OH] 1:0) to 33±5, 32±2, 30±4, and 28±3 nm as the concentration of PVA increased to [Fe^{2+}]:[OH] 1:10, 1:20, 1:60 and 1:100, respectively. Moreover, a significant decrease of the peak intensity of (020) was observed when PVA is added to LFP, suggesting that PVA inhibits crystal growth on the (020) plane.

TEM reveals a single crystalline particle that synthesized without PVA and $[Fe^{2+}]$:[OH] 1:10 (Figure 4.2 (b and d)), which was confirmed by Selected area electron diffraction (SAED, Figure 4.2 (c and e)). The ellipsoidal particles were found when $[Fe^{2+}]$:[OH] 1:60 was added. These secondary particles (average size ~ 200-800 nm) consist of primary particles averaging 60-80 nm in a polymer matrix as shown in Figure 4.2 (f and g). Based on the morphological differences observed, PVA plays a critical role in the formation of these secondary particles. The morphology of LFP in the presence of PVA can be explained based on the formation mechanism of LFP under solvothermal synthesis reported by Zhu et al.[51, 83] The findings indicated that after primary particles nucleated, their surface charge changed with time, which allowed them to approach each other and to fuse by oriented attachment. In our experiments, adding PVA in the reaction leads to an increase in the viscosity of the solution, which we believe reduces the diffusivity of LFP primary particles after nucleation, but does not inhibit attachment. Thus, we obtain polycrystalline secondary particles. Moreover, it is likely that PVA is trapped between the primary particles. The PVA acts as physical crosslinking sites with the secondary LFP particles, forming an elastomeric LFP-PVA composite structure. [190] [191]

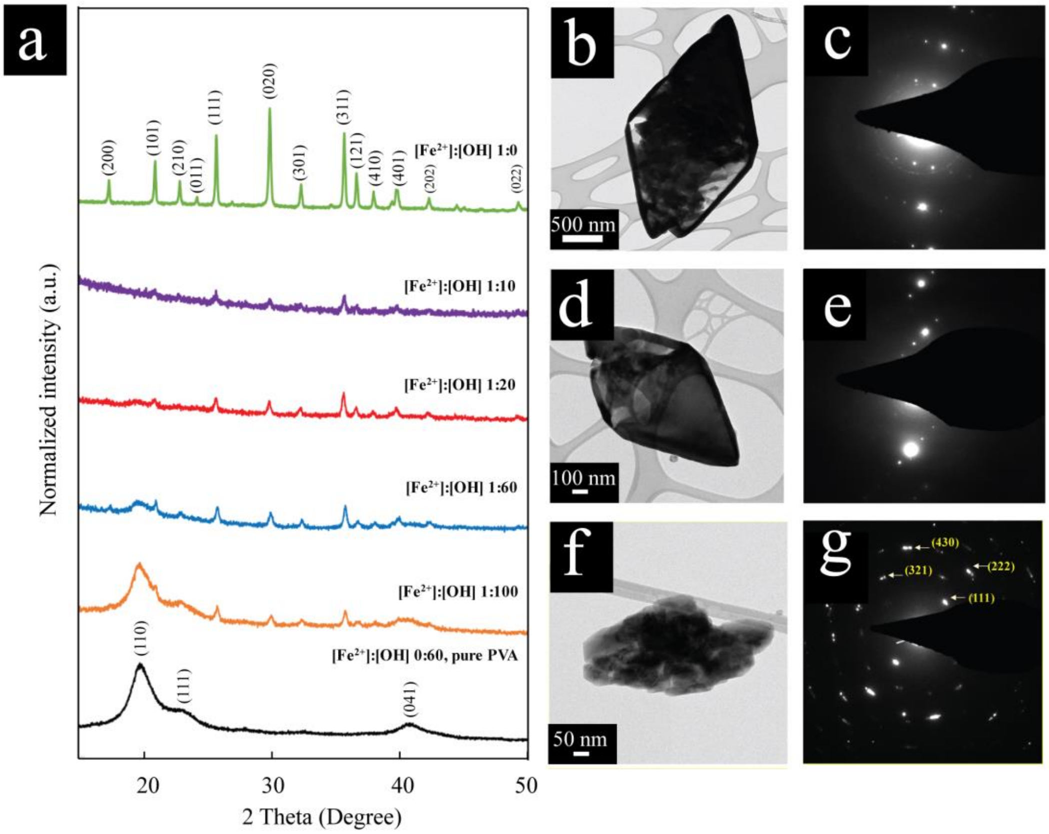

Figure 4.2 (a) XRD patterns for PVA, LFP samples synthesized with [Fe^{2+}]:[OH] 1:0, 1:10, 1:20, 1:60 and 1:100 at 160°C for 150 min. TE micrographs and SAED of washed of LFP/C composites with DMSO after solvothermal at 160°C for 150 min (b-c) [Fe^{2+}]:[OH] 1:0, (d-e) [Fe^{2+}]:[OH] 1:10, and (f-g) [Fe^{2+}]:[OH] 1:60.

The FTIR spectra of pure LFP, [Fe^{2+}]:[OH] 1:60, and pure PVA (see Figure 4.3) confirms the presence of PVA on the surface of LFP crystals when PVA was added. We observe the presence of a broad peak at 3292 cm^{-1} in the pure PVA and [Fe^{2+}]:[OH] 1:60 samples that indicate the stretching of O-H, which broadens due to intermolecular and intramolecular hydrogen bonds[192]. The other characteristic absorption bands of PVA occur at 919 cm^{-1} (bending of CH_2), 1141 cm^{-1} (stretching of C-O from crystalline PVA), 1328

cm^{-1} (wagging vibration of CH_2), 1415 cm^{-1} (symmetric band mode of $\nu_\delta(CH_2)$ and bending of O-H), [193-194] and 2900-3000 cm^{-1} (CH and CH_2 stretch). In the spectrum of $[Fe^{2+}]$:[OH] 1:60, the broad peak of O-H stretching decreases to 3248 cm^{-1} in comparison to pure PVA. This suggests that the strength of hydrogen bond in $[Fe^{2+}]$:[OH] 1:60 is weaker than in pure PVA, suggesting some hydroxyl groups are complexed with LFP. [195-196] The $[Fe^{2+}]$:[OH] 1:0 spectrum features for PO_4^{3-} at 1045 cm^{-1} and 1137 cm^{-1} correspond to the stretching mode of PO_4^{3-}, which is also observed in the $[Fe^{2+}]$:[OH] 1:60 spectrum. [138] The evidence of PVA on the surface of LFP particles can be used as a source of carbon to increase the electronic conductivity of LFP. However, to maximize tap density as well as the electrical conductivity of batteries, the thin layer of carbon is required.[40] Therefore, we must burn off most of the PVA but not all. Thus, Thermogravimetric analysis (TGA) was performed to observe the decomposition of PVA and LFP in air and 95% N_2/5% H_2 atmospheres.

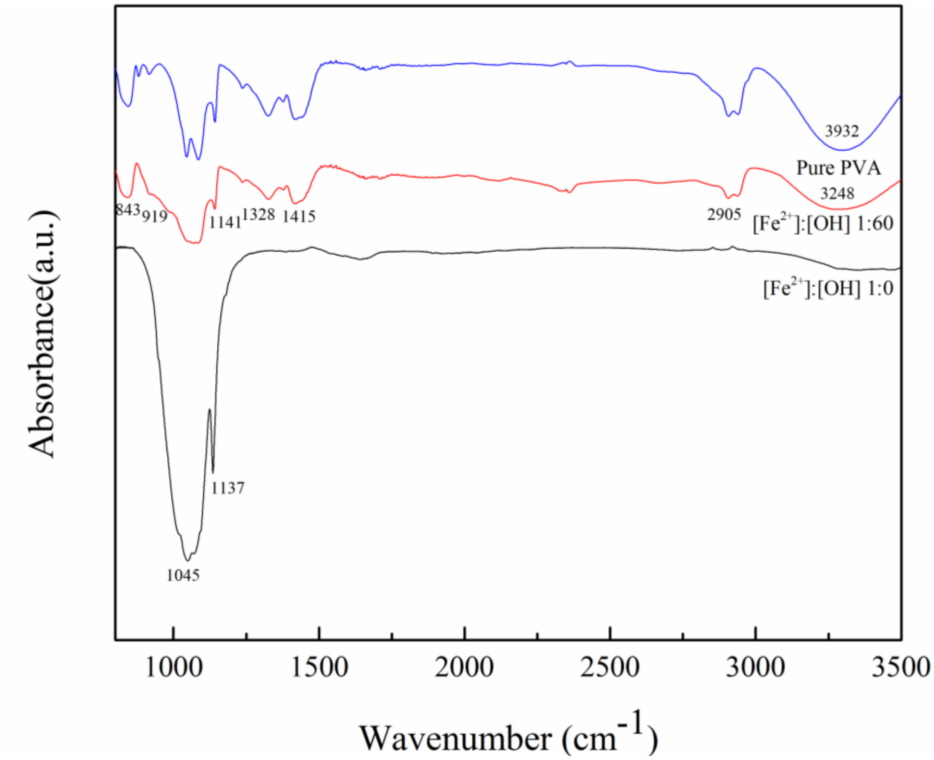

Figure 4.3 FTIR spectra of pure LFP, [Fe^{2+}]:[OH] 1:60, and pure PVA after solvothermal at 160°C for 150 min.

Pure PVA completely decomposes after heating to 510 °C under air (Figure 4.4a). However, the amount of remaining carbon from PVA heated in 95% N_2/5% H_2 is 5% by weight. The first decomposition step is observed at 120 °C, which could be attributed to the weight loss from the loss of water from chain-stripping elimination reactions and continues up to 180 °C (15% weight loss). Then, the second degradation starts from its melting point at about 200 °C until 310 °C weight loss due to the loss of -OH groups in cyclization reactions.[197-198] After that, we observe a gradual increase in weight loss until 480 °C. This second decomposition stage may correspond to the chemical degradation of the polymer, resulting from the chain scission of carbon-carbon bonds in the polymeric backbone. Finally, there is 5% carbon remaining in the sample. TGA of pure LFP (Figure 4.4b) shows a significant increase in the weight of LFP at 210 °C when it is heated in air. This is likely due to an exothermic oxidation of Fe(II) to Fe(III),[199] which is in agreement with the DSC curve collected simultaneously. In contrast, approximately 3% weight loss of pure LFP occurs when the sample is heated in 95% N_2/5% H_2. The summary of an evaluation of the individual steps is shown in Table 1.

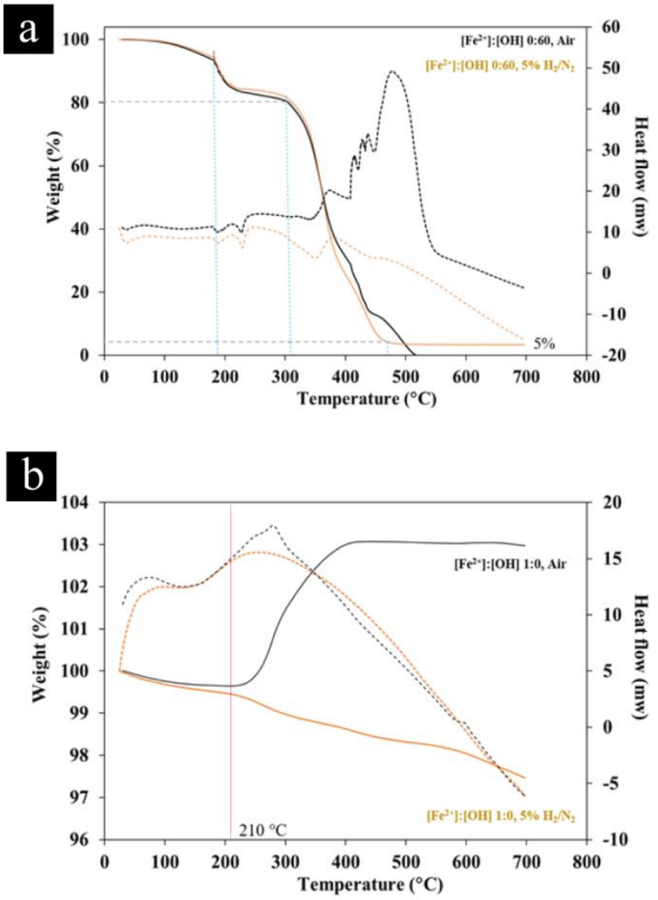

Figure 4.4 TGA analysis of (a) [Fe^{2+}]:[OH] 1:0 (LFP only) and (b) PVA only.

Table 4.1 Data from TGA and DTA curves for LFP and PVA only in 95% N_2/5% H_2

Temperature (°C)	Comments	
	PVA	LFP
120	Loss of water and water from chain-stripping elimination reactions	Loss of water
200-310	Loss of -OH groups	Continue weight loss
480	Chemical degradation of the polymer	Continue weight loss
700		Phase transformation from LFP to Fe_2P

4.3.2. Annealed LFP/C composite

Zhu et al. reported that LFP was transformed to the Fe_2P phase when it was annealed at 700 °C for 3 h. Their results demonstrated significant LFP crystal growth once annealed above 500 °C for 3 h [51]. Chang et al. determined that an LFP/C composite electrode with 7% carbon provided a high initial discharge capacity of 190.5 $mAhg^{-1}$. [40] Therefore, we chose samples with PVA concentrations of $[Fe^{2+}$:[OH 1:60 and annealed them to temperatures of 400 °C and 600 °C under 95% N_2/5% H_2 to thermally degrade carbon and induce porosity. After annealing for 1 hour, XRD confirms that the resulting material is pure LFP, as shown in Figure S1, Supporting information. We calculate the crystallite sizes of annealed LFP at 400, 500, and 600 °C using the Scherrer equation to be 36±4, 36±5, and 37±3 nm, respectively.

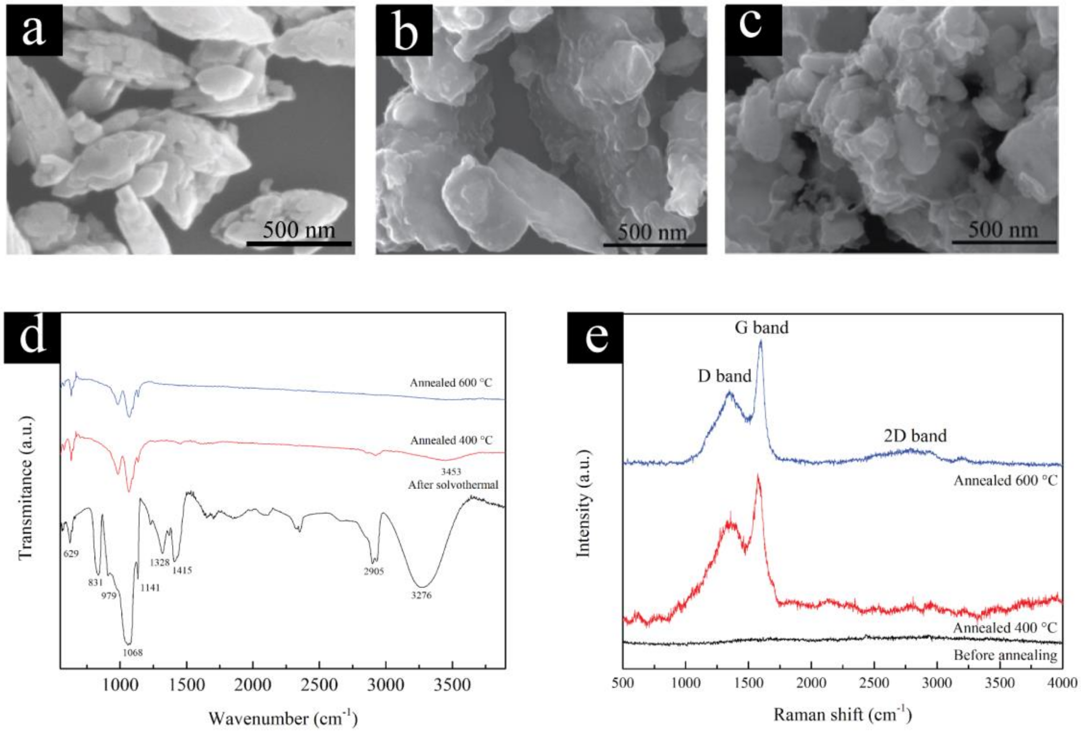

Figure 4.5 SEM micrographs of LFP/C composites after annealing at (a) 400, (b) 500, and (c) 600°C in 95%N_2/5%H_2 for 1 h. (d) FTIR and (e) Raman spectra of the LFP/C composites after solvothermal then annealed at 400 and 600°C in 95% N_2/5% H_2 for 1 h.

SEM and FTIR of the annealed LFP/C composites show that the polymer matrix surrounding the LFP particles degrades upon annealing (Figure 4.5(a-d)). The significant decrease in the OH peak confirms the partial decomposition of PVA in the samples when it is heated at 400°C for 1 h. When it is annealed to 600°C for 1 h, there is no peak observed for free OH bonds indicating the removal of all alcohol functional groups at those temperatures. The peaks located at 979, 1068, and 1141 cm^{-1} are attributed to the stretching modes of the trihedral PO_4^{3-}. These spectra demonstrate that heating improves the crystallinity of LFP/C composites as we observe the split peaks of PO_4^{3-} and remove excess polymer from the composites to form a porous structure. [143] Raman analysis of resulting LFP/C composite after annealing to 600°C in 95%N_2/5%H_2 for 1 h (Figure 4.5(e)) reveals the D (disordered) and G (graphitic) bands from graphite at 1345 and 1596 cm^{-1}, respectively. These D and G peaks represent the structural defects and the first order scattering of the E_{2g} vibrational mode in the graphene sheets, respectively[200-202]. The intensity ratio of D to G peak of annealed samples at 400 °C and 600 °C (I_D/I_G) are 0.76 and 0.55, respectively. These I_D/I_G ratios are better than the previous reports. [203] For example; LFP/C nanoparticles were synthesized using microwave assisted solvent treatment (I_D/I_G is 1.34).[203] Pratheeksha et al., reported their carbon coated LFP nanoparticles synthesized from flame spray pyrolysis followed by carbon coating showed sharp D and G bands with I_D/I_G ratio of 0.802. [204]

To confirm the presence of carbon and observe the grain structure. TEM of particles annealed at 600°C in 95% N_2/5% H_2 for 1 h reveals attached particles where the grain size does not change significantly from as-synthesized particles as confirmed by bright field TEM micrograph, SAED, and dark field micrograph (Figure 4.6 (a-c)). The high magnification micrograph in Figure 6(d) depicts that polycrystalline LFP particle is highly crystalline as the (301) lattice fringes can be observed. The carbon is seen to form a layer (average thickness 2.9 ± 1 nm) surrounding the LFP/C particle, forming a core-shell structure. Therefore, we expect an increase of electronic conductivity of LFP/C composite and a reduction of LFP dissolution into the electrolyte.[204] High-resolution STEM micrographs and EDS mapping images of Fe and C indicate that the surfaces of LFP were surrounded by evenly distributed carbon layer. This LFP/C particles can be able to improve the electronic conductivity, leading to a high specific capacity.[205]

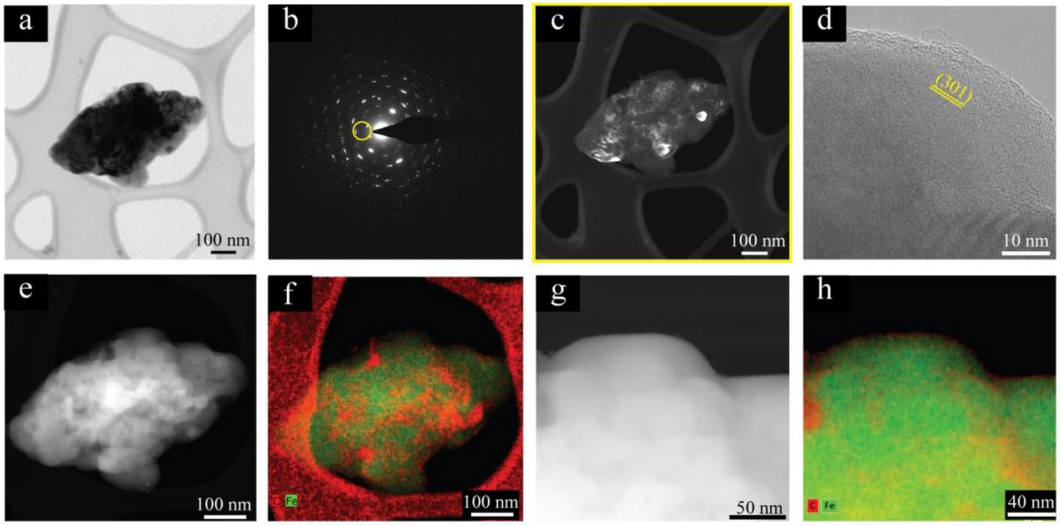

Figure 4.6 Bright field TEM micrographs, (b) the corresponding SAED, (c) dark field micrograph from circled yellow area, and (d) high-resolution TEM micrograph, (e-h) high-resolution STEM micrographs and the corresponding EDS elemental mapping images of the LFP/C composites after annealing at 600 °C in 95% N_2/5% H_2 for 1 h.

4.4. Conclusions

We successfully synthesized a 3D porous LFP/C cathode material in the presence of PVA as a carbon source using a solvothermal method. In the absence of PVA, plate-like LFP crystals were formed. The addition of PVA during synthesis resulted in the aggregation of primary particles, forming secondary particles. The secondary particles, under high PVA concentrations, were still smaller in dimension than the plate-like LFP crystals formed without PVA. Thus, polycrystalline LFP particles were formed within the PVA matrix due to the diffusion-limited growth of LFP in a viscous solution under the solvothermal process.

We suggest that a polymer coating on the surface of the LFP particles forms through electrostatic adsorption of the polymer onto the LFP particles. A thin layer of graphitic carbon coating the LFP particle surfaces was observed after annealing in 95% N_2/5% H_2 to 600 °C. We hypothesize that this may potentially lead to an enhancement of electrochemical performance for batteries.

Supporting Information

LFP/C composite

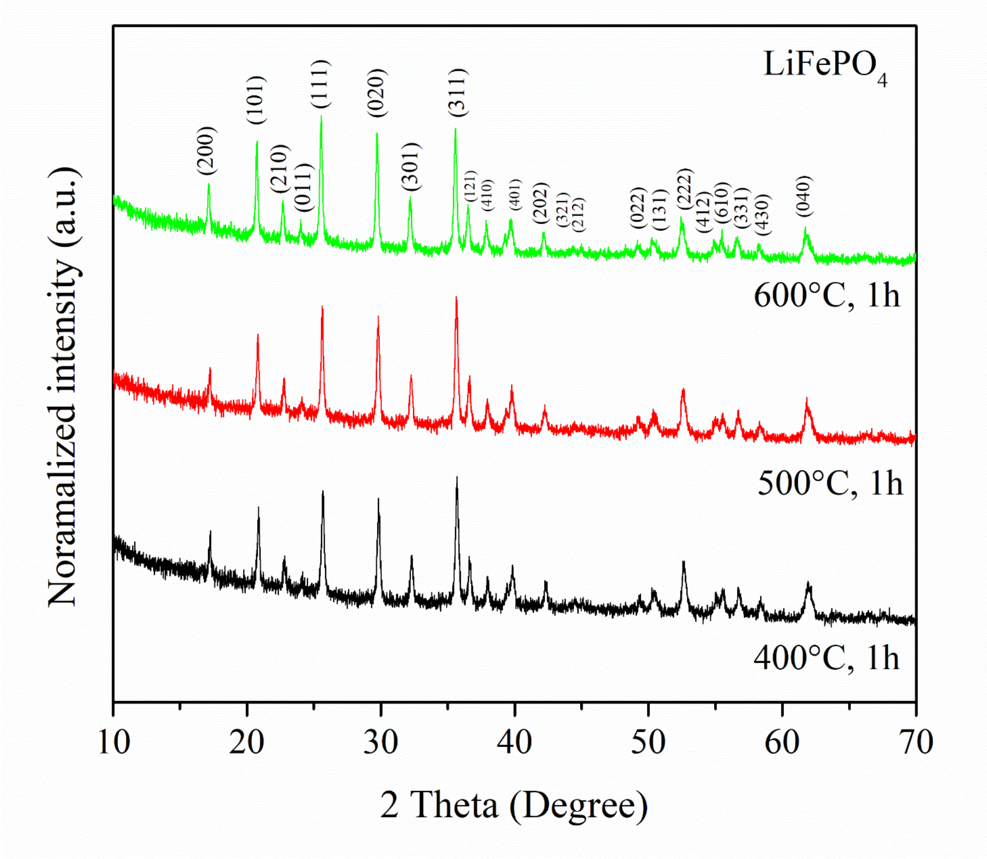

Figure S1 X-ray diffraction patterns of LFP/C composites after annealing to 400, 500 and 600°C in 95%N_2/5%H_2 for 1 hour.

References

1. Xu, B.; Qian, D.; Wang, Z.; Meng, Y. S., Recent progress in cathode materials research for advanced lithium ion batteries. *Materials Science and Engineering: R: Reports* **2012,** *73* (5-6), 51-65.

2. Park, O. K.; Cho, Y.; Lee, S.; Yoo, H.-C.; Song, H.-K.; Cho, J., Who will drive electric vehicles, olivine or spinel? *Energy & Environmental Science* **2011,** *4* (5), 1621.

3. Manthiram, A., Phospho-Olivine Cathodes for Lithium-Ion Batteries. *The Electrochemical Society Interface* **Spring 2009,** *V O L . 1 8 ,* (N O . 1).

4. Meligrana, G.; Gerbaldi, C.; Tuel, A.; Bodoardo, S.; Penazzi, N., Hydrothermal synthesis of high surface LiFePO4 powders as cathode for Li-ion cells. *Journal of Power Sources* **2006,** *160* (1), 516-522.

5. *High Energy Density Lithium Batteries*. Wiley-VCH: 2010.

6. Bini, M.; Capsoni, D.; Ferrari, S.; Quartarone, E.; Mustarelli, P., 1 - Rechargeable lithium batteries: key scientific and technological challenges. In *Rechargeable Lithium Batteries*, Franco, A. A., Ed. Woodhead Publishing: 2015; pp 1-17.

7. Pampal, E. S.; Stojanovska, E.; Simon, B.; Kilic, A., A review of nanofibrous structures in lithium ion batteries. *Journal of Power Sources* **2015,** *300*, 199-215.

8. Lee, H.; Yanilmaz, M.; Toprakci, O.; Fu, K.; Zhang, X., A review of recent developments in membrane separators for rechargeable lithium-ion batteries. *Energy & Environmental Science* **2014,** *7* (12), 3857-3886.

9. Tarascon, J. M.; Armand, M., Issues and challenges facing rechargeable lithium batteries. *Nature* **2001,** *414* (6861), 359-367.

10. Meng, Y. S.; Arroyo-de Dompablo, M. E., Recent Advances in First Principles Computational Research of Cathode Materials for Lithium-Ion Batteries. *Accounts of Chemical Research* **2013,** *46* (5), 1171-1180.

11. Ma C, L. Y., Li H, Fundamental scientific aspects of lithium batteries (VII)—positive electrode materials. *Energy Storage Sci Tech* **2014,** (3), 53–65.

12. Mizushima, K.; Jones, P. C.; Wiseman, P. J.; Goodenough, J. B., LixCoO2 (0<x<-1): A new cathode material for batteries of high energy density. *Materials Research Bulletin* **1980,** *15* (6), 783-789.

13. Thackeray, M., Lithium-ion batteries: An unexpected conductor. *Nat Mater* **2002,** *1* (2), 81-82.

14. Thackeray, M. M.; Kang, S.-H.; Johnson, C. S.; Vaughey, J. T.; Benedek, R.; Hackney, S. A., Li2MnO3-stabilized LiMO2 (M = Mn, Ni, Co) electrodes for lithium-ion batteries. *Journal of Materials Chemistry* **2007,** *17* (30), 3112-3125.

15. Amatucci, G. G.; Tarascon, J. M.; Klein, L. C., Cobalt dissolution in LiCoO2-based non-aqueous rechargeable batteries. *Solid State Ionics* **1996,** *83* (1), 167-173.

16. Maleki, H.; Deng, G.; Anani, A.; Howard, J., Thermal Stability Studies of Li-Ion Cells and Components. *Journal of The Electrochemical Society* **1999,** *146* (9), 3224-3229.

17. Reimers, J. N.; Dahn, J. R., Electrochemical and In Situ X-Ray Diffraction Studies of Lithium Intercalation in Li x CoO2. *Journal of The Electrochemical Society* **1992,** *139* (8), 2091-2097.

18. Fergus, J. W., Recent developments in cathode materials for lithium ion batteries. *Journal of Power Sources* **2010,** *195* (4), 939-954.

19. Rougier, A.; Gravereau, P.; Delmas, C., Optimization of the Composition of the Li1− z Ni1+ z O 2 Electrode Materials: Structural, Magnetic, and Electrochemical Studies. *Journal of The Electrochemical Society* **1996,** *143* (4), 1168-1175.

20. Huang, Z.-F.; Du, F.; Wang, C.-Z.; Wang, D.-P.; Chen, G., Low-spin Mn 3+ ion in rhombohedral LiMnO 2 predicted by first-principles calculations. *Physical Review B* **2007,** *75* (5), 054411.

21. Shao-Horn, Y.; Croguennec, L.; Delmas, C.; Nelson, E. C.; O'Keefe, M. A., Atomic resolution of lithium ions in LiCoO2. *Nat Mater* **2003,** *2* (7), 464-467.

22. Manthiram, A.; Vadivel Murugan, A.; Sarkar, A.; Muraliganth, T., Nanostructured electrode materials for electrochemical energy storage and conversion. *Energy & Environmental Science* **2008,** *1* (6), 621-638.

23. Liu, Q.; Mao, D.; Chang, C.; Huang, F., Phase conversion and morphology evolution during hydrothermal preparation of orthorhombic LiMnO 2 nanorods for lithium ion battery application. *Journal of Power Sources* **2007,** *173* (1), 538-544.

24. Tang, D.; Ben, L.; Sun, Y.; Chen, B.; Yang, Z.; Gu, L.; Huang, X., Electrochemical behavior and surface structural change of LiMn2O4 charged to 5.1 V. *Journal of Materials Chemistry A* **2014,** *2* (35), 14519-14527.

25. Zhang, T.; Li, D.; Tao, Z.; Chen, J., Understanding electrode materials of rechargeable lithium batteries via DFT calculations. *Progress in Natural Science: Materials International* **2013,** *23* (3), 256-272.

26. Padhi, A. K.; Nanjundaswamy, K. S.; Masquelier, C.; Okada, S.; Goodenough, J. B., Effect of Structure on the Fe3 + / Fe2 + Redox Couple in Iron Phosphates. *Journal of The Electrochemical Society* **1997,** *144* (5), 1609-1613.

27. Padhi, A. K.; Nanjundaswamy, K. S.; Goodenough, J. B., Phospho-olivines as Positive-Electrode Materials for Rechargeable Lithium Batteries. *Journal of The Electrochemical Society* **1997,** *144* (4), 1188-1194.

28. Yuan, L.-X.; Wang, Z.-H.; Zhang, W.-X.; Hu, X.-L.; Chen, J.-T.; Huang, Y.-H.; Goodenough, J. B., Development and challenges of LiFePO4 cathode material for lithium-ion batteries. *Energy & Environmental Science* **2011,** *4* (2), 269-284.

29. Ellis, B. L.; Lee, K. T.; Nazar, L. F., Positive Electrode Materials for Li-Ion and Li-Batteries. *Chemistry of Materials* **2010,** *22* (3), 691-714.

30. Streltsov, V. A.; Belokoneva, E. L.; Tsirelson, V. G.; Hansen, N. K., Multipole analysis of the electron density in triphylite, LiFePO4, using X-ray diffraction data. *Acta Crystallographica Section B* **1993,** *49* (2), 147-153.

31. Zhang, W.-J., Structure and performance of LiFePO4 cathode materials: A review. *Journal of Power Sources* **2011,** *196* (6), 2962-2970.

32. Chen, G.; Song, X.; Richardson, T. J., Electron Microscopy Study of the LiFePO4 to FePO4 Phase Transition. *Electrochemical and Solid-State Letters* **2006,** *9* (6), A295-A298.

33. Islam, M. S.; Driscoll, D. J.; Fisher, C. A. J.; Slater, P. R., Atomic-Scale Investigation of Defects, Dopants, and Lithium Transport in the LiFePO4 Olivine-Type Battery Material. *Chemistry of Materials* **2005,** *17* (20), 5085-5092.

34. Wang, L.; Zhou, F.; Meng, Y. S.; Ceder, G., First-principles study of surface properties of $\mathrm{Li}\mathrm{Fe}\mathrm{P}{\mathrm{O}}_{4}$: Surface energy, structure, Wulff shape, and surface redox potential. *Physical Review B* **2007,** *76* (16), 165435.

35. Nishimura, S.-i.; Kobayashi, G.; Ohoyama, K.; Kanno, R.; Yashima, M.; Yamada, A., Experimental visualization of lithium diffusion in LixFePO4. *Nat Mater* **2008,** *7* (9), 707-711.

36. Zhang, W.-J., Comparison of the Rate Capacities of LiFePO4 Cathode Materials. *Journal of The Electrochemical Society* **2010,** *157* (10), A1040-A1046.

37. Franger, S.; Le Cras, F.; Bourbon, C.; Rouault, H., Comparison between different LiFePO4 synthesis routes and their influence on its physico-chemical properties. *Journal of Power Sources* **2003,** *119*, 252-257.

38. Dong, Y. Z.; Zhao, Y. M.; Chen, Y. H.; He, Z. F.; Kuang, Q., Optimized carbon-coated LiFePO4 cathode material for lithium-ion batteries. *Materials Chemistry and Physics* **2009,** *115* (1), 245-250.

39. Wu, Y., *Lithium-ion batteries: Fundamentals and Applications*. CRC Press: 2015; Vol. 4.

40. Chang, Z.-R.; Lv, H.-J.; Tang, H.-W.; Li, H.-J.; Yuan, X.-Z.; Wang, H., Synthesis and characterization of high-density LiFePO4/C composites as cathode materials for lithium-ion batteries. *Electrochimica Acta* **2009,** *54* (20), 4595-4599.

41. Yang, S. T.; Zhao, N. H.; Dong, H. Y.; Yang, J. X.; Yue, H. Y., Synthesis and characterization of LiFePO4 cathode material dispersed with nano-structured carbon. *Electrochimica Acta* **2005,** *51* (1), 166-171.

42. Husain, I., *Electric and hybrid vehicles: design fundamentals*. CRC press: 2011.

43. Amine, K.; Liu, J.; Belharouak, I., High-temperature storage and cycling of C-LiFePO4/graphite Li-ion cells. *Electrochemistry Communications* **2005,** *7* (7), 669-673.

44. Arico, A. S.; Bruce, P.; Scrosati, B.; Tarascon, J.-M.; van Schalkwijk, W., Nanostructured materials for advanced energy conversion and storage devices. *Nat Mater* **2005,** *4* (5), 366-377.

45. Wang, K.; Cai, R.; Yuan, T.; Yu, X.; Ran, R.; Shao, Z., Process investigation, electrochemical characterization and optimization of LiFePO4/C composite from mechanical activation using sucrose as carbon source. *Electrochimica Acta* **2009,** *54* (10), 2861-2868.

46. Liang, G.; Wang, L.; Ou, X.; Zhao, X.; Xu, S., Lithium iron phosphate with high-rate capability synthesized through hydrothermal reaction in glucose solution. *Journal of Power Sources* **2008,** *184* (2), 538-542.

47. Doeff, M. M.; Hu, Y.; McLarnon, F.; Kostecki, R., Effect of Surface Carbon Structure on the Electrochemical Performance of LiFePO4. *Electrochemical and Solid-State Letters* **2003,** *6* (10), A207-A209.

48. Nien, Y.-H.; Carey, J. R.; Chen, J.-S., Physical and electrochemical properties of LiFePO4/C composite cathode prepared from various polymer-containing precursors. *Journal of Power Sources* **2009,** *193* (2), 822-827.

49. Wang, J.; Sun, X., Understanding and recent development of carbon coating on LiFePO 4 cathode materials for lithium-ion batteries. *Energy & Environmental Science* **2012,** *5* (1), 5163-5185.

50. Dominko, R.; Bele, M.; Gaberscek, M.; Remskar, M.; Hanzel, D.; Pejovnik, S.; Jamnik, J., Impact of the Carbon Coating Thickness on the Electrochemical Performance of LiFePO4 / C Composites. *Journal of The Electrochemical Society* **2005,** *152* (3), A607-A610.

51. Zhu, J.; Yoo, K.; El-halees, I.; Kisailus, D., Solution Deposition of Thin Carbon Coatings on LiFePO4. *ACS Applied Materials & Interfaces* **2014,** *6* (23), 21550-21557.

52. Wang, J.; Sun, X., Understanding and recent development of carbon coating on LiFePO4 cathode materials for lithium-ion batteries. *Energy & Environmental Science* **2012,** *5* (1), 5163-5185.

53. Croce, F.; D' Epifanio, A.; Hassoun, J.; Deptula, A.; Olczac, T.; Scrosati, B., A Novel Concept for the Synthesis of an Improved LiFePO4 Lithium Battery Cathode. *Electrochemical and Solid-State Letters* **2002,** *5* (3), A47-A50.

54. Chung, S. Y.; Bloking, J. T.; Chiang, Y. M., Electronically conductive phospho-olivines as lithium storage electrodes. *Nat. Mater.* **2002,** *1* (2), 123-128.

55. Hong, J.; Wang, C. S.; Chen, X.; Upreti, S.; Whittingham, M. S., Vanadium Modified LiFePO4 Cathode for Li-Ion Batteries. *Electrochemical and Solid-State Letters* **2009,** *12* (2), A33-A38.

56. Gabrisch, H.; Wilcox, J. D.; Doeff, M. M., Carbon Surface Layers on a High-Rate LiFePO[sub 4]. *Electrochemical and Solid-State Letters* **2006,** *9* (7), A360.

57. Simkiss, K. a. K. M. W., *Biomineralization : cell biology and mineral deposition* San Diego : Academic Press: 1989.

58. Lowenstam, H. A.; Weiner, S., *On Biomineralization*. Oxford University Press (US): Cary, US, 1989.

59. Addadi, L.; Gal, A.; Faivre, D.; Scheffel, A.; Weiner, S., Control of Biogenic Nanocrystal Formation in Biomineralization. *Israel Journal of Chemistry* **2015**, n/a-n/a.

60. Zaremba, C. M.; Belcher, A. M.; Fritz, M.; Li, Y.; Mann, S.; Hansma, P. K.; Morse, D. E.; Speck, J. S.; Stucky, G. D., Critical Transitions in the Biofabrication of Abalone Shells and Flat Pearls. *Chemistry of Materials* **1996,** *8* (3), 679-690.

61. Song, F.; Soh, A. K.; Bai, Y. L., Structural and mechanical properties of the organic matrix layers of nacre. *Biomaterials* **2003,** *24* (20), 3623-3631.

62. Nudelman, F., Nacre biomineralisation: A review on the mechanisms of crystal nucleation. *Seminars in Cell & Developmental Biology* **2015,** *46*, 2-10.

63. Wegst, U. G. K.; Bai, H.; Saiz, E.; Tomsia, A. P.; Ritchie, R. O., Bioinspired structural materials. *Nat Mater* **2015,** *14* (1), 23-36.

64. Sun, J.; Bhushan, B., Hierarchical structure and mechanical properties of nacre: a review. *RSC Advances* **2012,** *2* (20), 7617.

65. Hing, K. A., Bone repair in the twenty-first century: biology, chemistry or engineering? *Philosophical transactions. Series A, Mathematical, physical, and engineering sciences* **2004,** *362* (1825), 2821-50.

66. Navarrete, M. V.-R. a. D. A., CHAPTER 1 Biological Apatites in Bone and Teeth. In *Nanoceramics in Clinical Use: From Materials to Applications (2)*, The Royal Society of Chemistry: 2016; pp 1-29.

67. Beniash, E.; Aizenberg, J.; Addadi, L.; Weiner, S., Amorphous calcium carbonate transforms into calcite during sea urchin larval spicule growth. *Proceedings of the Royal Society of London. Series B: Biological Sciences* **1997,** *264* (1380), 461-465.

68. Politi, Y.; Arad, T.; Klein, E.; Weiner, S.; Addadi, L., Sea Urchin Spine Calcite Forms via a Transient Amorphous Calcium Carbonate Phase. *Science* **2004,** *306* (5699), 1161-1164.

69. Raz, S.; Hamilton, P. C.; Wilt, F. H.; Weiner, S.; Addadi, L., The Transient Phase of Amorphous Calcium Carbonate in Sea Urchin Larval Spicules: The Involvement of Proteins and Magnesium Ions in Its Formation and Stabilization. *Advanced Functional Materials* **2003,** *13* (6), 480-486.

70. Gong, Y. U. T.; Killian, C. E.; Olson, I. C.; Appathurai, N. P.; Amasino, A. L.; Martin, M. C.; Holt, L. J.; Wilt, F. H.; Gilbert, P. U. P. A., Phase transitions in biogenic amorphous calcium carbonate. *Proceedings of the National Academy of Sciences* **2012,** *109* (16), 6088-6093.

71. Seto, J.; Ma, Y.; Davis, S. A.; Meldrum, F.; Gourrier, A.; Kim, Y.-Y.; Schilde, U.; Sztucki, M.; Burghammer, M.; Maltsev, S.; Jäger, C.; Cölfen, H., Structure-property

relationships of a biological mesocrystal in the adult sea urchin spine. *Proceedings of the National Academy of Sciences* **2012,** *109* (10), 3699-3704.

72. Chen, Z.-y.; Zhu, H.-l.; Ji, S.; Fakir, R.; Linkov, V., Influence of carbon sources on electrochemical performances of LiFePO 4/C composites. *Solid State Ionics* **2008,** *179* (27), 1810-1815.

73. Smirnov, K. S.; Zhorin, V. A.; Smirnov, S. E., Study of properties of cathode materials based on lithium-iron phosphate. *Inorganic Materials: Applied Research* **2014,** *5* (5), 467-470.

74. Maccario, M.; Croguennec, L.; Wattiaux, A.; Suard, E.; Le Cras, F.; Delmas, C., C-containing LiFePO4 materials — Part I: Mechano-chemical synthesis and structural characterization. *Solid State Ionics* **2008,** *179* (35), 2020-2026.

75. Maccario, M.; Croguennec, L.; Le Cras, F.; Delmas, C., Electrochemical performances in temperature for a C-containing LiFePO4 composite synthesized at high temperature. *Journal of Power Sources* **2008,** *183* (1), 411-417.

76. M. Talebi-Esfandarani, S. R., M. Gauthier, P. Sauriol, G. Liang, M. Dollé, LiFePO4 synthesized via melt synthesis using low-cost iron precursors. *Journal of Solid State Electrochemistry* **2016,** *20* (7), 1821-1829.

77. Gauthier, M.; Michot, C.; Ravet, N.; Duchesneau, M.; Dufour, J.; Liang, G.; Wontcheu, J.; Gauthier, L.; MacNeil, D. D., Melt Casting LiFePO4 : I. Synthesis and Characterization. *Journal of The Electrochemical Society* **2010,** *157* (4), A453-A462.

78. Talebi-Esfandarani, M.; Rousselot, S.; Gauthier, M.; Sauriol, P.; Duttine, M.; Wattiaux, A.; Liu, Y.; Sun, A.; Liang, G.; Dollé, M., Control of the LiFePO4 electrochemical properties using low-cost iron precursor in a melt process. *Journal of Solid State Electrochemistry* **2016,** *20* (12), 3481-3490.

79. Zhao, R. R.; Zhu, L. C.; Huang, Z. Z.; Liang, J. Z.; Chen, H. Y., An investigation on the performance of LiFePO4/C derived from various FePO4. *Ionics* **2013,** *19* (4), 581-588.

80. Satyavani, T. V. S. L.; Srinivas Kumar, A.; Subba Rao, P. S. V., Methods of synthesis and performance improvement of lithium iron phosphate for high rate Li-ion batteries: A review. *Engineering Science and Technology, an International Journal* **2016,** *19* (1), 178-188.

81. Benedek, P.; Wenzler, N.; Yarema, M.; Wood, V. C., Low temperature hydrothermal synthesis of battery grade lithium iron phosphate. *RSC Advances* **2017,** *7* (29), 17763-17767.

82. Wang, F.; Chen, J.; Tan, Z.; Wu, M.; Yi, B.; Su, W.; Wei, Z.; Liu, S., Low-temperature electrochemical performances of LiFePO4 cathode materials for lithium ion batteries. *Journal of the Taiwan Institute of Chemical Engineers* **2014,** *45* (4), 1321-1330.

83. Zhu, J.; Fiore, J.; Li, D.; Kinsinger, N. M.; Wang, Q.; DiMasi, E.; Guo, J.; Kisailus, D., Solvothermal Synthesis, Development, and Performance of LiFePO4 Nanostructures. *Crystal Growth & Design* **2013,** *13* (11), 4659-4666.

84. Gao, Y.; Li, L.; Peng, H.; Wei, Z., Surfactant-Assisted Sol–Gel Synthesis of Nanostructured Ruthenium-Doped Lithium Iron Phosphate as a Cathode for Lithium-Ion Batteries. *ChemElectroChem* **2014,** *1* (12), 2146-2152.

85. Wang, G.; Bewlay, S.; Yao, J.; Ahn, J.-H.; Dou, S.; Liu, H.-K., Characterization of LiM x Fe1− x PO 4 (M= Mg, Zr, Ti) Cathode Materials Prepared by the Sol-Gel Method. *Electrochemical and Solid-State Letters* **2004,** *7* (12), A503-A506.

86. Kim, J.-K.; Choi, J.-W.; Chauhan, G. S.; Ahn, J.-H.; Hwang, G.-C.; Choi, J.-B.; Ahn, H.-J., Enhancement of electrochemical performance of lithium iron phosphate by controlled sol–gel synthesis. *Electrochimica Acta* **2008,** *53* (28), 8258-8264.

87. W.D. Kingery, H. K. B., and D.R. Uhlman, *Introduction to Ceramics*. John Wiley & Sons, Inc: United States of America, 1975.

88. Blackford, J. R.; Skouvaklis, G.; Purser, M.; Koutsos, V., Friction on ice: stick and slip. *Faraday Discussions* **2012,** *156* (0), 243-254.

89. Jane, R. B., Sintering and microstructure of ice: a review. *Journal of Physics D: Applied Physics* **2007,** *40* (21), R355.

90. Lifshitz, I. M.; Slyozov, V. V., The kinetics of precipitation from supersaturated solid solutions. *Journal of Physics and Chemistry of Solids* **1961,** *19* (1), 35-50.

91. Huang, F.; Zhang, H.; Banfield, J. F., Two-Stage Crystal-Growth Kinetics Observed during Hydrothermal Coarsening of Nanocrystalline ZnS. *Nano Lett* **2003,** *3* (3), 373-378.

92. Kisailus, D.; Choi, J. H.; Lange, F. F., GaN nanocrystals from oxygen and nitrogen-based precursors. *Journal of Crystal Growth* **2003,** *249* (1), 106-120.

93. Usta, M.; Glicksman, M. E.; Wright, R. N., The effect of heat treatment on Mg2Si coarsening in aluminum 6105 alloy. *Metallurgical and Materials Transactions A* **2004,** *35* (2), 435-438.

94. Dong, J.; Hu, M. Z.; Payzant, E. A.; Armstrong, T. R.; Becher, P. F., Grain growth in nanocrystalline yttrium-stabilized zirconia thin films synthesized by spin coating of polymeric precursors. *Journal of nanoscience and nanotechnology* **2002,** *2* (2), 161-169.

95. Chan, T.-Y.; Liu, S.-J.; Lin, S.-T., Effects of high concentrations of liquid phase and magnesia on the grain growth of alumina. *Ceramics international* **1998,** *24* (8), 617-625.

96. Vandermeer, R. A.; Hu, H., On the grain growth exponent of pure iron. *Acta Metallurgica et Materialia* **1994,** *42* (9), 3071-3075.

97. Zhu, K.; Ruan, Q.; Godfrey, A. In *The kinetics of grain growth in near-micrometre grain size copper produced by spark plasma sintering*, IOP Conference Series: Materials Science and Engineering, IOP Publishing: 2015; p 012060.

98. Kim, B.-N.; Hiraga, K.; Morita, K., Kinetics of normal grain growth depending on the size distribution of small grains. *Materials Transactions* **2003,** *44* (11), 2239-2244.

99. Usta, M.; Glicksman, M.; Wright, R., The effect of heat treatment on Mg 2 Si coarsening in aluminum 6105 alloy. *Metallurgical and Materials Transactions A* **2004,** *35* (2), 435-438.

100. Zhu, J.; Vo, T.; Li, D.; Lu, R.; Kinsinger, N. M.; Xiong, L.; Yan, Y.; Kisailus, D., Crystal Growth of Li[Ni1/3Co1/3Mn1/3]O2 as a Cathode Material for High-Performance Lithium Ion Batteries. *Crystal Growth & Design* **2012,** *12* (3), 1118-1123.

101. Yoshida, H.; Hashimoto, S.; Yamamoto, T., Dopant effect on grain boundary diffusivity in polycrystalline alumina. *Acta Materialia* **2005,** *53* (2), 433-440.

102. Laidler, K. J., The development of the Arrhenius equation. *J. Chem. Educ* **1984,** *61* (6), 494.

103. Belharouak, I.; Johnson, C.; Amine, K., Synthesis and electrochemical analysis of vapor-deposited carbon-coated LiFePO4. *Electrochemistry Communications* **2005,** *7* (10), 983-988.

104. Yamada, A.; Hosoya, M.; Chung, S.-C.; Kudo, Y.; Hinokuma, K.; Liu, K.-Y.; Nishi, Y., Olivine-type cathodes. *Journal of Power Sources* **2003,** *119-121*, 232-238.

105. Arnold, G.; Garche, J.; Hemmer, R.; Ströbele, S.; Vogler, C.; Wohlfahrt-Mehrens, M., Fine-particle lithium iron phosphate LiFePO4 synthesized by a new low-cost aqueous precipitation technique. *Journal of Power Sources* **2003,** *119-121*, 247-251.

106. Hsu, K.-F.; Tsay, S.-Y.; Hwang, B.-J., Synthesis and characterization of nano-sized LiFePO4cathode materials prepared by a citric acid-based sol–gel route. *J. Mater. Chem.* **2004,** *14* (17), 2690-2695.

107. Franger, S.; Le Cras, F.; Bourbon, C.; Rouault, H., LiFePO[sub 4] Synthesis Routes for Enhanced Electrochemical Performance. *Electrochemical and Solid-State Letters* **2002,** *5* (10), A231.

108. Świder, J.; Świętosławski, M.; Molenda, M.; Dziembaj, R., A Novel Concept for the Synthesis of Nanometric LiFePO4 by Co-precipitation Method in an Anhydrous Environment. *Procedia Engineering* **2014,** *98*, 36-41.

109. Audebrand, N.; Auffrédic, J.-P.; Louër, D., X-ray Diffraction Study of the Early Stages of the Growth of Nanoscale Zinc Oxide Crystallites Obtained from Thermal Decomposition of Four Precursors. General Concepts on Precursor-Dependent Microstructural Properties. *Chemistry of Materials* **1998,** *10* (9), 2450-2461.

110. Nudelman, F., Nacre biomineralisation: A review on the mechanisms of crystal nucleation. *Semin Cell Dev Biol* **2015,** *46*, 2-10.

111. Wegst, U. G.; Bai, H.; Saiz, E.; Tomsia, A. P.; Ritchie, R. O., Bioinspired structural materials. *Nat Mater* **2015,** *14* (1), 23-36.

112. Levi-Kalisman, Y.; Falini, G.; Addadi, L.; Weiner, S., Structure of the nacreous organic matrix of a bivalve mollusk shell examined in the hydrated state using cryo-TEM. *J Struct Biol* **2001,** *135* (1), 8-17.

113. Ashit Rao , H. C., *Mineralization Schemes in the Living World: Mesocrystals*. 22 December 2016.

114. Cölfen, H. a. M. A., *Mesocrystals and nonclassical crystallization*. Chichester, England ; Hoboken, NJ : Wiley: 2008.

115. De Yoreo, J. J.; Gilbert, P. U. P. A.; Sommerdijk, N. A. J. M.; Penn, R. L.; Whitelam, S.; Joester, D.; Zhang, H.; Rimer, J. D.; Navrotsky, A.; Banfield, J. F.; Wallace, A. F.; Michel, F. M.; Meldrum, F. C.; Cölfen, H.; Dove, P. M., Crystallization by particle attachment in synthetic, biogenic, and geologic environments. *Science* **2015,** *349* (6247).

116. Cölfen, H.; Antonietti, M., Crystal Design of Calcium Carbonate Microparticles Using Double-Hydrophilic Block Copolymers. *Langmuir* **1998,** *14* (3), 582-589.

117. Cölfen, H.; Mann, S., Higher-order organization by mesoscale self-assembly and transformation of hybrid nanostructures. *Angewandte Chemie International Edition* **2003,** *42* (21), 2350-2365.

118. Van Santen, R. A., The Ostwald step rule. *The Journal of Physical Chemistry* **1984,** *88* (24), 5768-5769.

119. Gower, L. B., Biomimetic Model Systems for Investigating the Amorphous Precursor Pathway and Its Role in Biomineralization. *Chemical Reviews* **2008,** *108* (11), 4551-4627.

120. Niederberger, M.; Colfen, H., Oriented attachment and mesocrystals: Non-classical crystallization mechanisms based on nanoparticle assembly. *Physical Chemistry Chemical Physics* **2006,** *8* (28), 3271-3287.

121. Pouget, E. M.; Bomans, P. H. H.; Dey, A.; Frederik, P. M.; de With, G.; Sommerdijk, N. A. J. M., The Development of Morphology and Structure in Hexagonal Vaterite. *Journal of the American Chemical Society* **2010,** *132* (33), 11560-11565.

122. Politi, Y.; Metzler, R. A.; Abrecht, M.; Gilbert, B.; Wilt, F. H.; Sagi, I.; Addadi, L.; Weiner, S.; Gilbert, P. U. P. A., Transformation mechanism of amorphous calcium carbonate into calcite in the sea urchin larval spicule. *Proceedings of the National Academy of Sciences* **2008,** *105* (45), 17362-17366.

123. Gal, A.; Habraken, W.; Gur, D.; Fratzl, P.; Weiner, S.; Addadi, L., Calcite Crystal Growth by a Solid-State Transformation of Stabilized Amorphous Calcium Carbonate Nanospheres in a Hydrogel. *Angewandte Chemie International Edition* **2013,** *52* (18), 4867-4870.

124. Sun, S.; Gebauer, D.; Colfen, H., A solvothermal method for synthesizing monolayer protected amorphous calcium carbonate clusters. *Chemical Communications* **2016,** *52* (43), 7036-7038.

125. Gower, L. A.; Tirrell, D. A., Calcium carbonate films and helices grown in solutions of poly(aspartate). *Journal of Crystal Growth* **1998,** *191* (1), 153-160.

126. Gower, L. B.; Odom, D. J., Deposition of calcium carbonate films by a polymer-induced liquid-precursor (PILP) process. *Journal of Crystal Growth* **2000,** *210* (4), 719-734.

127. Faatz, M.; Gröhn, F.; Wegner, G., Amorphous Calcium Carbonate: Synthesis and Potential Intermediate in Biomineralization. *Advanced Materials* **2004,** *16* (12), 996-1000.

128. Zhang, H.; Chen, B.; Ren, Y.; Waychunas, G. A.; Banfield, J. F., Response of nanoparticle structure to different types of surface environments: Wide-angle x-ray scattering and molecular dynamics simulations. *Physical Review B* **2010,** *81* (12), 125444.

129. Yang, H. G.; Zeng, H. C., Self-Construction of Hollow SnO2 Octahedra Based on Two-Dimensional Aggregation of Nanocrystallites. *Angewandte Chemie International Edition* **2004,** *43* (44), 5930-5933.

130. Penn, R. L.; Banfield, J. F., Morphology development and crystal growth in nanocrystalline aggregates under hydrothermal conditions: insights from titania. *Geochimica et cosmochimica acta* **1999,** *63* (10), 1549-1557.

131. Kulak, A. N.; Iddon, P.; Li, Y.; Armes, S. P.; Cölfen, H.; Paris, O.; Wilson, R. M.; Meldrum, F. C., Continuous Structural Evolution of Calcium Carbonate Particles: A Unifying Model of Copolymer-Mediated Crystallization. *Journal of the American Chemical Society* **2007,** *129* (12), 3729-3736.

132. Xu, A.-W.; Antonietti, M.; Yu, S.-H.; Cölfen, H., Polymer-Mediated Mineralization and Self-Similar Mesoscale-Organized Calcium Carbonate with Unusual Superstructures. *Advanced Materials* **2008,** *20* (7), 1333-1338.

133. Pipich, V.; Balz, M.; Wolf, S. E.; Tremel, W.; Schwahn, D., Nucleation and Growth of CaCO3 Mediated by the Egg-White Protein Ovalbumin: A Time-Resolved in situ Study Using Small-Angle Neutron Scattering. *Journal of the American Chemical Society* **2008,** *130* (21), 6879-6892.

134. Oaki, Y.; Imai, H., Morphological Evolution of Inorganic Crystal into Zigzag and Helical Architectures with an Exquisite Association of Polymer: A Novel Approach for Morphological Complexity. *Langmuir* **2005,** *21* (3), 863-869.

135. Oaki, Y.; Imai, H., Hierarchically Organized Superstructure Emerging from the Exquisite Association of Inorganic Crystals, Organic Polymers, and Dyes: A Model Approach Towards Suprabiomineral Materials. *Advanced Functional Materials* **2005,** *15* (9), 1407-1414.

136. Zhu, J.; Fiore, J.; Li, D.; Kinsinger, N. M.; Wang, Q.; DiMasi, E.; Guo, J.; Kisailus, D., Solvothermal Synthesis, Development, and Performance of LiFePO4Nanostructures. *Crystal Growth & Design* **2013,** *13* (11), 4659-4666.

137. Soltani, N.; Saion, E.; Erfani, M.; Rezaee, K.; Bahmanrokh, G.; Drummen, G. P.; Bahrami, A.; Hussein, M. Z., Influence of the polyvinyl pyrrolidone concentration on particle size and dispersion of ZnS nanoparticles synthesized by microwave irradiation. *International journal of molecular sciences* **2012,** *13* (10), 12412-12427.

138. Ait Salah, A.; Jozwiak, P.; Zaghib, K.; Garbarczyk, J.; Gendron, F.; Mauger, A.; Julien, C. M., FTIR features of lithium-iron phosphates as electrode materials for rechargeable lithium batteries. *Spectrochimica Acta Part A: Molecular and Biomolecular Spectroscopy* **2006,** *65* (5), 1007-1013.

139. Alexander, M. R.; Payan, S.; Duc, T. M., Interfacial interactions of plasma-polymerized acrylic acid and an oxidized aluminium surface investigated using XPS, FTIR and poly(acrylic acid) as a model compound. *Surface and Interface Analysis* **1998,** *26* (13), 961-973.

140. Dong, J.; Ozaki, Y.; Nakashima, K., Infrared, Raman, and Near-Infrared Spectroscopic Evidence for the Coexistence of Various Hydrogen-Bond Forms in Poly(acrylic acid). *Macromolecules* **1997,** *30* (4), 1111-1117.

141. Gadaleta, S.; Paschalis, E.; Betts, F.; Mendelsohn, R.; Boskey, A., Fourier transform infrared spectroscopy of the solution-mediated conversion of amorphous calcium phosphate to hydroxyapatite: new correlations between X-ray diffraction and infrared data. *Calcified tissue international* **1996,** *58* (1), 9-16.

142. Peak, D.; Luther, G. W.; Sparks, D. L., ATR-FTIR spectroscopic studies of boric acid adsorption on hydrous ferric oxide. *Geochimica et Cosmochimica Acta* **2003,** *67* (14), 2551-2560.

143. Termine, J. D.; Eanes, E. D., Comparative chemistry of amorphous and apatitic calcium phosphate preparations. *Calcified Tissue Research* **1972,** *10* (1), 171-197.

144. Granasy, L.; Pusztai, T.; Borzsonyi, T.; Warren, J. A.; Douglas, J. F., A general mechanism of polycrystalline growth. *Nat Mater* **2004,** *3* (9), 645-650.

145. Gránásy, L.; Pusztai, T.; Tegze, G.; Warren, J. A.; Douglas, J. F., Growth and form of spherulites. *Physical Review E* **2005,** *72* (1), 011605.

146. Andreassen, J.-P.; Flaten, E. M.; Beck, R.; Lewis, A. E., Investigations of spherulitic growth in industrial crystallization. *Chemical Engineering Research and Design 88* (9), 1163-1168.

147. Beck, R.; Andreassen, J.-P., Spherulitic growth of calcium carbonate. *Crystal Growth & Design* **2010,** *10* (7), 2934-2947.

148. Yu, S.-H.; Cölfen, H.; Antonietti, M., Polymer-Controlled Morphosynthesis and Mineralization of Metal Carbonate Superstructures. *The Journal of Physical Chemistry B* **2003,** *107* (30), 7396-7405.

149. Meldrum, F. C.; Cölfen, H., Controlling Mineral Morphologies and Structures in Biological and Synthetic Systems. *Chemical Reviews* **2008,** *108* (11), 4332-4432.

150. Fu, Y. S.; Song, Y. F.; Kulinich, S. A.; Sun, J.; Liu, J.; Du, X. W., Single-crystal ZnO flocky sphere formed by three-dimensional oriented attachment of nanoparticles. *Journal of Physics and Chemistry of Solids* **2008,** *69* (4), 880-883.

151. Zhu, J., Synthesis, Characterization and Performance of Cathodes for Lithium Ion Batteries. 2014.

152. Imai, H.; Oaki, Y.; Kotachi, A., A Biomimetic Approach for Hierarchically Structured Inorganic Crystals through Self-Organization. *Bulletin of the Chemical Society of Japan* **2006,** *79* (12), 1834-1851.

153. Li, J.; Armstrong, B. L.; Kiggans, J.; Daniel, C.; Wood III, D. L., Optimization of LiFePO4 nanoparticle suspensions with polyethyleneimine for aqueous processing. *Langmuir* **2012,** *28* (8), 3783-3790.

154. HE, L.-h.; ZHAO, Z.-w.; LIU, X.-h.; CHEN, A.-l.; SI, X.-f., Thermodynamics analysis of LiFePO 4 pecipitation from Li–Fe (II)–P–H 2 O system at 298 K. *Transactions of Nonferrous Metals Society of China* **2012,** *22* (7), 1766-1770.

155. Choi, J.; Rubner, M. F., Influence of the Degree of Ionization on Weak Polyelectrolyte Multilayer Assembly. *Macromolecules* **2005,** *38* (1), 116-124.

156. Jaffar, S.; Nam, K. T.; Khademhosseini, A.; Xing, J.; Langer, R. S.; Belcher, A. M., Layer-by-layer surface modification and patterned electrostatic deposition of quantum dots. *Nano Lett* **2004,** *4* (8), 1421-1425.

157. Jongen, N.; Hofmann, H.; Bowen, P.; Lemaitre, J., Calcination and morphological evolution of cubic copper oxalate particles. *Journal of materials science letters* **2000,** *19* (12), 1073-1075.

158. Beck, R.; Andreassen, J.-P., The onset of spherulitic growth in crystallization of calcium carbonate. *Journal of Crystal Growth* **2010,** *312* (15), 2226-2238.

159. Ivanov, V. K.; Fedorov, P. P.; Baranchikov, A. Y.; Osiko, V. V., Oriented attachment of particles: 100 years of investigations of non-classical crystal growth. *Russian Chemical Reviews* **2014,** *83* (12), 1204.

160. Gehrke, N.; Cölfen, H.; Pinna, N.; Antonietti, M.; Nassif, N., Superstructures of Calcium Carbonate Crystals by Oriented Attachment. *Crystal Growth & Design* **2005,** *5* (4), 1317-1319.

161. Burleson, D. J.; Penn, R. L., Two-Step Growth of Goethite from Ferrihydrite. *Langmuir* **2006,** *22* (1), 402-409.

162. Penn, R. L.; Banfield, J. F., Imperfect Oriented Attachment: Dislocation Generation in Defect-Free Nanocrystals. *Science* **1998,** *281* (5379), 969-971.

163. Wang, G.; Li, L.; Lan, J.; Chen, L.; You, J., Biomimetic crystallization of calcium carbonate spherules controlled by hyperbranched polyglycerols. *Journal of Materials Chemistry* **2008,** *18* (24), 2789-2797.

164. Prosini, P. P.; Carewska, M.; Scaccia, S.; Wisniewski, P.; Pasquali, M., Long-term cyclability of nanostructured LiFePO4. *Electrochimica Acta* **2003,** *48* (28), 4205-4211.

165. Lu, C.-Z.; Fey, G. T.-K.; Kao, H.-M., Study of LiFePO4 cathode materials coated with high surface area carbon. *Journal of Power Sources* **2009,** *189* (1), 155-162.

166. Smith, J. E.; Brodsky, M. H.; Crowder, B. L.; Nathan, M. I.; Pinczuk, A., Raman Spectra of Amorphous Si and Related Tetrahedrally Bonded Semiconductors. *Physical Review Letters* **1971,** *26* (11), 642-646.

167. Padhi, A. K.; Nanjundaswamy, K.; Goodenough, J. B., Phospho-olivines as positive-electrode materials for rechargeable lithium batteries. *Journal of the electrochemical society* **1997,** *144* (4), 1188-1194.

168. Paolella, A.; Bertoni, G.; Marras, S.; Dilena, E.; Colombo, M.; Prato, M.; Riedinger, A.; Povia, M.; Ansaldo, A.; Zaghib, K.; Manna, L.; George, C., Etched colloidal LiFePO4 nanoplatelets toward high-rate capable Li-ion battery electrodes. *Nano Lett* **2014,** *14* (12), 6828-6835.

169. Park, O. K.; Cho, Y.; Lee, S.; Yoo, H.-C.; Song, H.-K.; Cho, J., Who will drive electric vehicles, olivine or spinel? *Energy & Environmental Science* **2011,** *4* (5), 1621-1633.

170. Shahid, R.; Murugavel, S., Particle size dependent confinement and lattice strain effects in LiFePO 4. *Physical Chemistry Chemical Physics* **2013,** *15* (43), 18809-18814.
171. Satyavani, T.; Kiran, B. R.; Kumar, V. R.; Kumar, A. S.; Naidu, S., Effect of particle size on dc conductivity, activation energy and diffusion coefficient of lithium iron phosphate in Li-ion cells. *Engineering Science and Technology, an International Journal* **2016,** *19* (1), 40-44.

172. Fedorková, A.; Oriňáková, R.; Oriňák, A.; Wiemhöfer, H.-D.; Kaniansky, D.; Winter, M., Surface treatment of LiFePO4 cathode material with PPy/PEG conductive layer. *Journal of Solid State Electrochemistry* **2010,** *14* (12), 2173-2178.

173. Kim, H.; Cho, B.; Cho, W., Electronically conductive phospho-olivines as lithium storage electrodes. *Journal of Power Sources* **2004,** *132* (1-2), 235-239.

174. Yang, M.-R.; Ke, W.-h.; Wu, S.-h., Improving electrochemical properties of lithium iron phosphate by addition of vanadium. *Journal of Power Sources* **2007,** *165* (2), 646-650.

175. Channagiri, S. A.; Nagpure, S. C.; Babu, S. S.; Noble, G. J.; Hart, R. T., Porosity and phase fraction evolution with aging in lithium iron phosphate battery cathodes. *Journal of Power Sources* **2013,** *243*, 750-757.

176. Doherty, C. M.; Caruso, R. A.; Smarsly, B. M.; Adelhelm, P.; Drummond, C. J., Hierarchically porous monolithic LiFePO4/carbon composite electrode materials for high power lithium ion batteries. *Chemistry of Materials* **2009,** *21* (21), 5300-5306.

177. Yu, F.; Zhang, J.; Yang, Y.; Song, G., Porous micro-spherical aggregates of LiFePO4/C nanocomposites: A novel and simple template-free concept and synthesis via sol–gel-spray drying method. *Journal of Power Sources* **2010,** *195* (19), 6873-6878.

178. Yu, F.; Zhang, L.; Lai, L.; Zhu, M.; Guo, Y.; Xia, L.; Qi, P.; Wang, G.; Dai, B., High Electrochemical Performance of LiFePO4 Cathode Material via In-Situ Microwave Exfoliated Graphene Oxide. *Electrochimica Acta* **2015,** *151*, 240-248.

179. Yang, X.; Xu, Y.; Zhang, H.; Huang, Y. a.; Jiang, Q.; Zhao, C., Enhanced high rate and low-temperature performances of mesoporous LiFePO4/Ketjen Black nanocomposite cathode material. *Electrochimica Acta* **2013,** *114*, 259-264.

180. Yu, F.; Lim, S. H.; Zhen, Y.; An, Y.; Lin, J., Optimized electrochemical performance of three-dimensional porous LiFePO4/C microspheres via microwave irradiation assisted synthesis. *Journal of Power Sources* **2014,** *271*, 223-230.

181. Chen, Z.; Dahn, J. R., Reducing Carbon in LiFePO4 / C Composite Electrodes to Maximize Specific Energy, Volumetric Energy, and Tap Density. *Journal of The Electrochemical Society* **2002,** *149* (9), A1184-A1189.

182. Li, C.-C.; Chang, S.-J.; Chen, C.-A., Effects of sp2- and sp3-carbon coatings on dissolution and electrochemistry of water-based LiFePO4 cathodes. *Journal of Applied Electrochemistry* **2017**.

183. Swain, P.; Viji, M.; Mocherla, P. S. V.; Sudakar, C., Carbon coating on the current collector and LiFePO4 nanoparticles – Influence of sp2 and sp3-like disordered carbon on the electrochemical properties. *Journal of Power Sources* **2015,** *293*, 613-625.

184. Wegst, U. G.; Bai, H.; Saiz, E.; Tomsia, A. P.; Ritchie, R. O., Bioinspired structural materials. *Nature materials* **2015,** *14* (1), 23-36.

185. Chen, S. F.; Zhu, J. H.; Jiang, J.; Cai, G. B.; Yu, S. H., Polymer-Controlled Crystallization of Unique Mineral Superstructures. *Advanced Materials* **2010,** *22* (4), 540-545.

186. Wang, G.; Sæterli, R.; Rørvik, P. M.; van Helvoort, A. T.; Holmestad, R.; Grande, T.; Einarsrud, M.-A., Self-assembled growth of PbTiO3 nanoparticles into microspheres and bur-like structures. *Chemistry of materials* **2007,** *19* (9), 2213-2221.

187. Levi, Y.; Albeck, S.; Brack, A.; Weiner, S.; Addadi, L., Control Over Aragonite Crystal Nucleation and Growth: An In Vitro Study of Biomineralization. *Chemistry - A European Journal* **1998,** *4* (3), 389-396.

188. Falini, G.; Albeck, S.; Weiner, S.; Addadi, L., Control of Aragonite or Calcite Polymorphism by Mollusk Shell Macromolecules. *Science* **1996,** *271* (5245), 67-69.

189. Kinsinger, N. M.; Wong, A.; Li, D.; Villalobos, F.; Kisailus, D., Nucleation and Crystal Growth of Nanocrystalline Anatase and Rutile Phase TiO2 from a Water-Soluble Precursor. *Crystal Growth & Design* **2010,** *10* (12), 5254-5261.

190. Hennink, W.; Van Nostrum, C. F., Novel crosslinking methods to design hydrogels. *Advanced drug delivery reviews* **2012,** *64*, 223-236.

191. Kinsinger, N.; Tantuccio, A.; Sun, M.; Yan, Y.; Kisailus, D., Photocatalytic titanium dioxide composite. *Journal of nanoscience and nanotechnology* **2011,** *11* (8), 7015-7021.

192. Gohil, J.; Bhattacharya, A.; Ray, P., Studies on the crosslinking of poly (vinyl alcohol). *Journal of polymer research* **2006,** *13* (2), 161-169.

193. Shehap, A., Thermal and spectroscopic studies of polyvinyl alcohol/sodium carboxy methyl cellulose blends. *Egypt. J. Solids* **2008,** *31* (1), 75-91.

194. Kim, G.-M., Fabrication of Bio-Nanocomposite Nanofibers Mimicking the Mineralized Hard Tissues via Electrospinning Process. In *Nanofibers*, Kumar, A., Ed. InTech: Rijeka, 2010; p Ch. 04.

195. Kayal, S.; Ramanujan, R., Doxorubicin loaded PVA coated iron oxide nanoparticles for targeted drug delivery. *Materials Science and Engineering: C* **2010,** *30* (3), 484-490.

196. Santhiya, D.; Subramanian, S.; Natarajan, K.; Malghan, S., Surface chemical studies on the competitive adsorption of poly (acrylic acid) and poly (vinyl alcohol) onto alumina. *Journal of colloid and interface science* **1999,** *216* (1), 143-153.

197. Peng, Z.; Kong, L. X., A thermal degradation mechanism of polyvinyl alcohol/silica nanocomposites. *Polymer Degradation and Stability* **2007,** *92* (6), 1061-1071.

198. Gilman, J. W.; VanderHart, D. L.; Kashiwagi, T., Thermal Decomposition Chemistry of Poly (vinyl alcohol) Char Characterization and Reactions with Bismaleimides. ACS Publications: 1995.

199. Yang, S.; Song, Y.; Zavalij, P. Y.; Stanley Whittingham, M., Reactivity, stability and electrochemical behavior of lithium iron phosphates. *Electrochemistry Communications* **2002,** *4* (3), 239-244.

200. Song, J.; Wang, L.; Ma, Z.; Du, Z.; Shao, G.; Kong, L.; Gao, W., Biotemplated fabrication of a novel hierarchical porous C/LiFePO 4/C composite for Li-ion batteries. *RSC advances* **2015,** *5* (3), 1983-1988.

201. Ha, J.; Park, S.-K.; Yu, S.-H.; Jin, A.; Jang, B.; Bong, S.; Kim, I.; Sung, Y.-E.; Piao, Y., A chemically activated graphene-encapsulated LiFePO 4 composite for high-performance lithium ion batteries. *Nanoscale* **2013,** *5* (18), 8647-8655.

202. Yang, J.; Wang, J.; Tang, Y.; Wang, D.; Li, X.; Hu, Y.; Li, R.; Liang, G.; Sham, T.-K.; Sun, X., LiFePO 4–graphene as a superior cathode material for rechargeable lithium batteries: impact of stacked graphene and unfolded graphene. *Energy & Environmental Science* **2013,** *6* (5), 1521-1528.

203. Liu, M.; Zhao, Y.; Gao, S.; Wang, Y.; Duan, Y.; Han, X.; Dong, Q., Mild solution synthesis of graphene loaded with LiFePO 4–C nanoplatelets for high performance lithium ion batteries. *New Journal of Chemistry* **2015,** *39* (2), 1094-1100.

204. Pratheeksha, P. M.; Mohan, E. H.; Sarada, B. V.; Ramakrishna, M.; Hembram, K.; Srinivas, P. V. V.; Daniel, P. J.; Rao, T. N.; Anandan, S., Development of a novel carbon-coating strategy for producing core–shell structured carbon coated LiFePO 4 for an improved Li-ion battery performance. *Physical Chemistry Chemical Physics* **2017,** *19* (1), 175-188.

205. Su, F.-Y.; You, C.; He, Y.-B.; Lv, W.; Cui, W.; Jin, F.; Li, B.; Yang, Q.-H.; Kang, F., Flexible and planar graphene conductive additives for lithium-ion batteries. *Journal of Materials Chemistry* **2010,** *20* (43), 9644-9650.